DEFECT FORMATION MECHANISMS IN POWDER-BED METAL ADDITIVE MANUFACTURING

Submitted in partial fulfillment of the requirements for

the degree of

Doctor of Philosophy

in

Materials Science and Engineering

Ross W. Cunningham

B.S., Materials Science and Engineering, Lehigh University
B.S., Integrated Business and Engineering, Lehigh University
M.S., Materials Science and Engineering, Carnegie Mellon University

Carnegie Mellon University
Pittsburgh, PA

May, 2018

Dedicated to my family,

Peter, Cynthia, and Joshua

Abstract

Metal Additive Manufacturing (AM) provides the means to fabricate complex metallic parts with reduced time to market and material waste and improved design freedom. Industries with strict materials qualifications such as aerospace, biomedical, and automotive are increasingly looking to AM to meet their production needs. However, significant materials-related challenges impede the widespread adoption of these technologies for critical components. In particular, fatigue resistance in as-built parts has proven to be inferior and unpredictable due to the large and variable presence of porosity. This presents a challenge for the qualification of any load bearing part without extensive post-processing, such as Hot Isostatic Pressing, and thorough inspection. Improved understanding of the underlying mechanisms behind defect formation will assist in designing process improvements to minimize or eliminate defects without relying entirely on post-processing. In this work, the effects of powder, processing parameters, and post-processing on porosity formation in powder-bed metal AM processes are investigated using X-ray microtomography and a newly developed in-situ high speed radiography technique, Dynamic X-ray Radiography. High resolution X-ray computed tomography is used to characterize defect morphology, size, and spatial distribution as a function of process and material inputs. Dynamic X-ray Radiography, which enables the in-situ observation of the laser-metal interactions at frame rates on the order of 100 kHz (and faster), is utilized to understand the dynamic behavior and transitions that occur in the vapor depression across process space. Experimental validation of previously held assumptions regarding defect formation as well as new insights into the influence of the vapor cavity on defect formation are presented.

Acknowledgements

Like most good things in life, this was a team effort. I could not have accomplished a fraction of what I have without the help and support, academically or otherwise, of a number of people I now wish to thank. First and foremost, I would like to acknowledge my advisor, Tony Rollett, for guiding me along a path I never could have imaged when I started the Ph.D. process four years ago. I don't think either of us could have anticipated the last few years, but it has certainly been an interesting and fulfilling journey. His passion for science and unyielding support for his students personal and professional development (even when we forget to send in our weekly reports) has been a true inspiration.

Next, I would like to thank my committee members Dr. Chris Pistorius, Dr. Jack Beuth, and Dr. John Elmer for their feedback and assistance over the course of this research, particularly on the final stretch. Also, while she is not on my committee I consider Dr. Sandra DeVincent Wolf to be an equally esteemed mentor and I would like to thank her for all the time spent on my professional development. Next, I acknowledge our collaborators Drs. Tao Sun and Cang Zhao from the Advanced Photon Source and thank them for inviting us along on this DXR adventure with them. Similarly, I especially would like to acknowledge Dr. Xianghui Xiao for his help and especially his patience during my many late nights collecting CT data at the APS.

It has been a pleasure and privilege to spend my graduate years as a member of the Carnegie Mellon research community, particularly the Rollett group. I owe a great deal to both the old guard of Drs. Tugce Ozturk, Brian Lin, Clay Stein, Samikshya Subedi, Sudipto Mandal and Shivram Kashyap for welcoming me into the group and mentoring me, as well as the new members Rachel Lim, Chris Kantzos, and Joe Pauza for letting me pay it forward and for reminding me of the excitement that comes with being an eager new researcher. I also acknowledge the past and present

iii

Beuth Group at Carnegie Mellon University, particularly Dr. Sneha Narra, without whom much of this work would not have been possible.

Last but certainly not least I thank my friends Saransh, Chetali, Steve and Steph for for all of their support and encouragement as we took this journey together. Finally, I owe everything to my family, who have always been there for each other even through the most difficult of times. As a parting note, I would like to give one last thank you to my father, Peter Cunningham, for inspiring me to get into science from an early age and always making sure I had the support I needed to achieve my goals.

Ross Cunningham

Pittsburgh, PA

May 2018

List of Publications

Directly resulted from this thesis work:

1. Cunningham, R., Nicolas, A., Madsen, J., Fodran, E., Anagnostou, E., Sangid, M. D., & Rollett, A. D. (2017). Analyzing the effects of powder and post-processing on porosity and properties of electron beam melted Ti-6Al-4V. *Materials Research Letters*, 1-10.
2. Cunningham, R., Narra, S. P., Montgomery, C., Beuth, J., & Rollett, A. D. (2017). Synchrotron-based X-ray microtomography characterization of the effect of processing variables on porosity formation in laser power-bed additive manufacturing of Ti-6Al-4V. *JOM*, *69*(3), 479-484.
3. Cunningham, R., Narra, S. P., Ozturk, T., Beuth, J., & Rollett, A. D. (2016). Evaluating the effect of processing parameters on porosity in electron beam melted Ti-6Al-4V via synchrotron X-ray microtomography. *JOM*, *68*(3), 765-771.

Supported by this thesis work:

1. Kantzos, C., Cunningham, R., Tari, V., & Rollett, A. D. (2017). Characterization of Metal Additive Manufacturing Surfaces using Synchrotron X-ray CT and Micromechanical Modeling. *Computational Mechanics*.
2. Zhao, C., Fezzaa, K., Cunningham, R., Wen, H., De Carlo, F., Chen, L., ... & Sun, T. (2017). Real-time monitoring of laser powder bed fusion process using high-speed X-ray imaging and diffraction. *Scientific Reports*, *7*.
3. Narra, S. P., Cunningham, R., Beuth, J., & Rollett, A. D. (2017). Location Specific Solidification Microstructure Control in Electron Beam Melting of Ti-6Al-4V. *Additive Manufacturing*.
4. Rao, S., Cunningham, R., Ozturk, T., & Rollett, A. D. (2016). Measurement and Analysis of Porosity in Al-10Si-Mg Components Additively Manufactured by Selective Laser Melting. *Materials Performance and Characterization*, *5*(5), 701-716.

Table of Contents

List of Figures

List of Tables

List of Symbols and Abbreviations

AM	additive manufacturing
LMBF	laser powder bed fusion
EBM	Electron Beam Melting
LOF	Lack of Fusion
HIP	Hot isostatic press
3D	three dimensional
CT	computed tomography
XCT	x-ray computed tomography
T	temperature
T_o	initial temperature
Q	adsorbed power
V	beam velocity
r	radial distance
k	thermal conductivity
D	thermal diffusivity
ρ	density
η	viscocity
P	Power
I	Current
μXCT	x-ray microtomography
A	absorptivity coefficient
I_L	laser intensity
w_o	laser spot radius
t	time
t_{KH}	keyhole transition temperature
t_d	dwell time
$\Delta H/h_s$	normalized enthalpy
T_b	boiling point
T_m	melting point

h_s	enthalpy of melting
CCD	charge-coupled device
LuAG	Lutetium Aluminum Garnet
I_{norm}	normalized image
I_{raw}	raw image
I_{dark}	dark-field image
I_{flat}	bright-field image
FFT	fast Fourier transform
d_O	overlap depth
t_l	layer thickness
l_c	collimator focal length
l_o	objective lens focal length
PREP	plasma rotating electrode process
e	ellipticity
S	surface area
$F(S,\gamma)$	surface tension force
F_r	recoil pressure force
α	depression angle
HT	heat treatment
KH	Keyhole
P_a	atmospheric pressure
P_{sat}	saturation pressure
γ	surface tension coefficient
T_c	critical temperature
V_d	drill velocity

Chapter 1: Introduction

1.1 Motivation

Additive Manufacturing (AM) is a rapidly developing field of technologies with the goal of manufacturing functional, near-net-shape metallic parts from a three dimensional computer model by the layer-wise addition of material [1]. These technologies have generated considerable interest for their potential benefits of enabling advanced part geometries, and cost savings through reduced material waste and time-to market. Powder bed processes are one such class of technology, which operate by sequentially spreading powder layers of controlled thickness across a build area, where the appropriate cross section is selectively melted via an electron beam (EBM) or laser beam (LPBF). These processes are popular because of their high resolution and dimensional tolerance, and the availability of automated commercial machines capable of producing functional parts with reduced operator involvement. However, the replacement of a structural component using AM is significantly more complex than simply having the 3-D geometry of the component; variability in performance as a function of materials and AM processes also poses a major challenge. Even if the required form and fit tolerances are met, minor variations in the AM process can produce undesirable mechanical properties that are unsuitable for safety critical components. Defects deriving from the starting materials, process control, and non-ideal post-processing can significantly impact structural integrity and durability and may result in a component that appears satisfactory, but in fact does not meet the rigorous requirement for safety critical applications [2]–[6]. This presents a barrier for the use of AM to fabricate parts destined for fatigue-sensitive applications, such as aerospace or biomedical components, as these defects have been shown to be a source of fatigue crack initiation, Fig. 1.1.
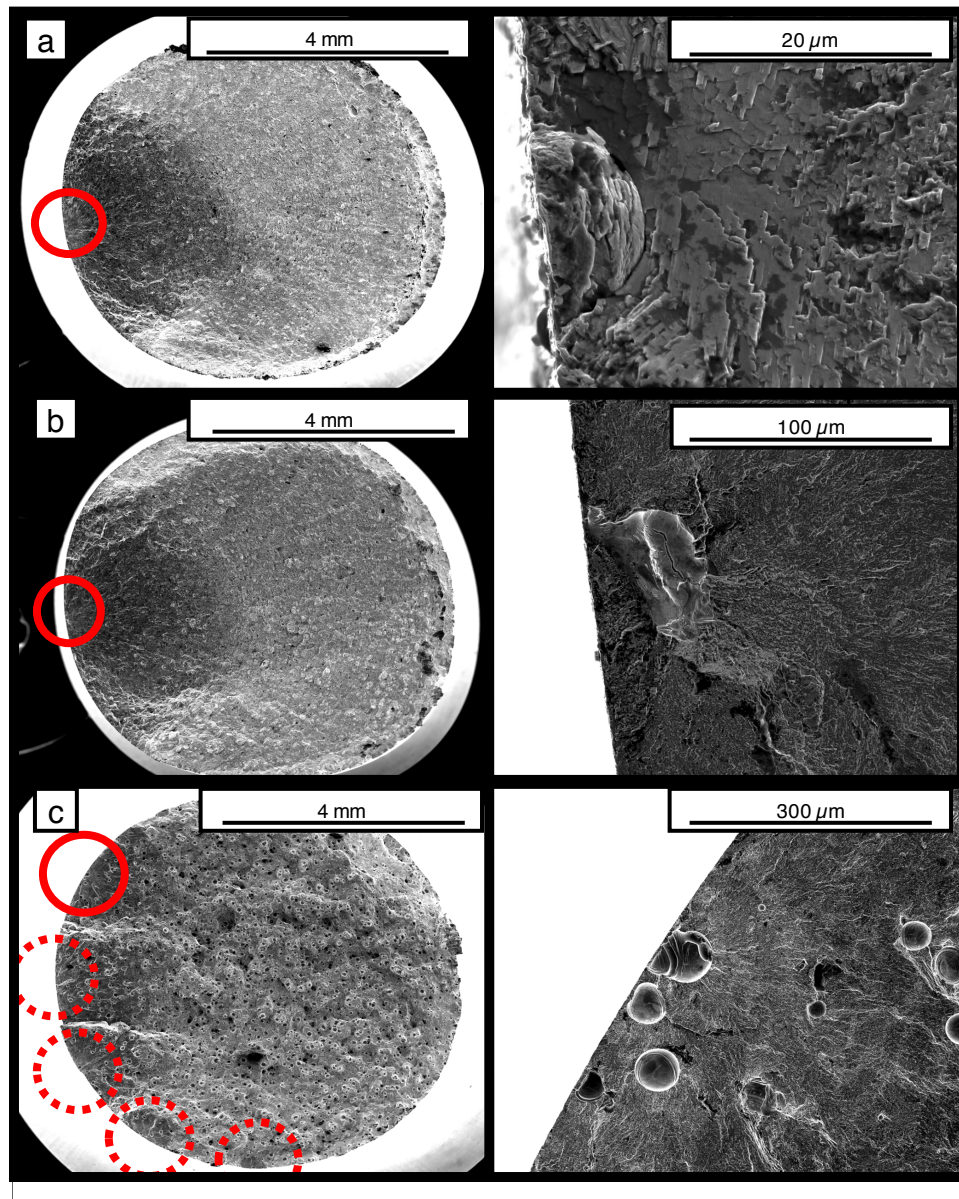
Figure 1.1: Various types of defects found in LPBF AM Inconel 718 acting as fatigue crack initiation sites. Represented in this study are a) gas porosity, b) lack of fusion, and c) keyholing [7]

More troublesome is quantifying the uncertainty associated with these properties and accurately calculating the resulting risks. A better fundamental understanding of the possible defect formation mechanisms, particularly with regard to the effects of powder properties, processing parameters, and post-processing on defect population will help define post-processing and inspection requirements that will help in managing these risks.

1.2 Objective

The objective of this research is to investigate possible defect formation mechanisms active in powder bed additive manufacturing processes. While experimentally derived methods for determining appropriate process parameters, such a process mapping [8], have shown success in determining areas of process space that produce nearly fully dense parts, their applications are limited to specific machine manufacturers, and often specific versions of machines. With the wide variety of machines available [1], and the excitement for AM driving the frequent addition of new machines to market, a more fundamental understanding of defect formation mechanisms presents the opportunity to have a more wide-ranging impact. Furthermore, mapping techniques often ignore defects that may arise from the raw materials [3], or develop during post-processing [9], many of which have been discussed but lack conclusive experimental proof. Therefore, this study will investigate a number of defect formation mechanisms mentioned in literature, beginning with the raw material powder, defects that form during processing, and finally those that may form as a result of post-processing. Additionally, newly developed in-situ characterization techniques will be used to gain new insight into the dynamic behavior that these complex processes exhibit on the melt pool scale.

1.3 Methods and Approach

By contrast with previous studies that have largely relied on bulk-density techniques or cross sections to evaluate porosity in AM materials, this work heavily utilizes 3D X-ray computed tomography to evaluate and differentiate different types of defects, as well as newly developed high-speed in-situ x-ray imaging technique to visualize defect formation mechanisms in real time. High resolution synchrotron-based X-ray microtomography was used to characterize porosity in sections of bulk AM parts fabricated with different powders, process variables, and post-

processing to evaluate trends and likely defect sources. This information was then used to design specific experiments to identify the dynamic behavior that results in defect formation using the in-situ imaging technique.

1.4 Hypotheses

As the title of this thesis suggests, the focus of this research is on understanding defect formation mechanisms in metal powder bed additive manufacturing processes. This study focuses on the following hypotheses:

1. Inert gas trapped in the powder can be transferred to printed parts. While this is generally accepted as reasonable assumption [10], definitive experimental proof of this occurrence as well as the mechanism(s) that allow the transfer for full melting processes have not been conclusively demonstrated.

2. Process parameters resulting in sufficiently high power density (high power, low velocity) lead to keyhole pore formation because of instability-driven collapse of the vapor cavity. The transition between this region and the acceptable "process window", generally considered to be the conduction to keyhole transition, is assumed to be sharp.

3. Inert gas containing pores in HIPed AM parts can regrow following post-HIP heat treatment. This includes trapped gas porosity from the powder, and lack of fusion defects built in inert-gas environments. This is based on previous work from powder metallurgy (thermal induced porosity) [11] and the titanium foam industry [12] where the expansion of pressurized inert gas pores at high temperature through creep has been extensively documented. The assumption is that these defects can contain sufficient internal inert gas that expansion occurs at typical heat treatment temperatures.

Chapter 2: Background

2.1 Powder Bed Additive Manufacturing

Powder bed systems represent one of the main families of technologies within metal additive manufacturing, along with powder feed and wire feed [1]. These differ from the other methods by their layering technique, which involves the spreading/raking of powder to a specified layer thickness, followed by the selective melting of the desired area on each layer, which acts to weld it to the underlying material. Some of the benefits of these systems include high dimensional tolerance, ability to create internal passages, and a high level of automation compared to other systems [1]. Machines within this category are further distinguished by their heat source, which is either an electron beam for Electron Beam Melting (EBM) systems, or a laser for Laser Powder Bed Fusion (LPBF). Two of the popular machine manufacturers are Arcam AB for the EBM, and EOS for the LPBF process. Samples fabricated from these two machines are the focus of this study. A schematic powder bed system is shown in Fig. 2.1, based on an EOS M290 LPBF system. EBM systems operate with similar principles, but utilize gravity assisted powder hoppers rather than a vertically mobile powder-feed platform.
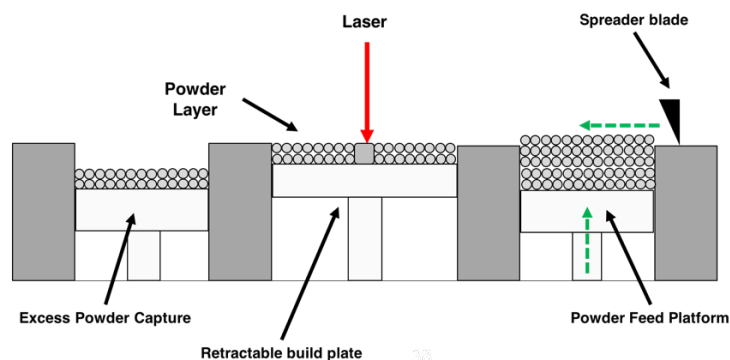
Figure 2.1: Schematic LPBF AM system.

2.1.1 Laser Powder Bed Fusion

The LPBF machine used in this study is an EOS M290. These machines use a 400 W Yb-fiber laser with a D86 spot size of approximately 100 μm (at focal) as the heat source [13], [14]. A controlled atmosphere of either nitrogen or argon is used in the chamber depending on the reactivity of the material. A blade is used to spread powder across a 250 x 250 mm build plate. EOS supplies a variety of metallic powder, generally smaller than 60 μm, for use in these systems. An example of EOS-supplied *Titanium Ti64* powder, made from gas atomized Ti-6Al-4V alloy, is shown in Fig. 2.2.
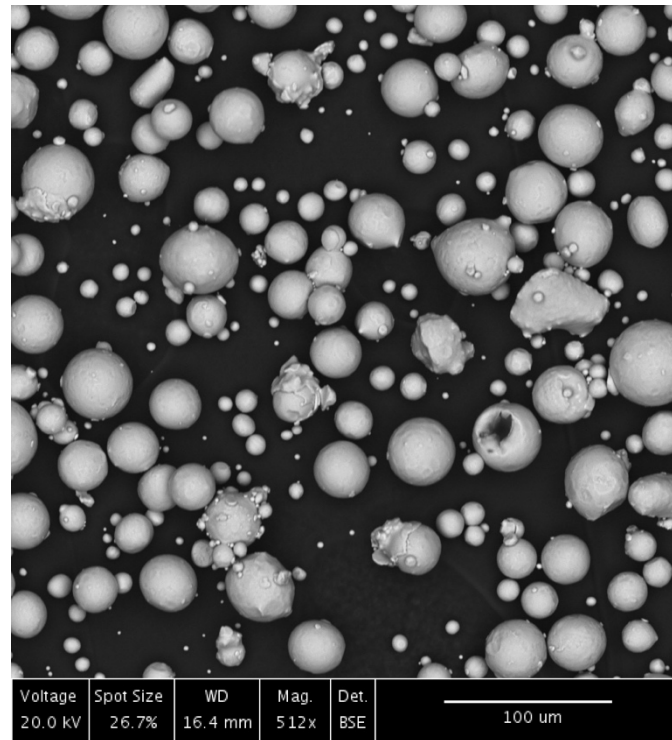
Figure 2.2: Backscatter mode SEM micrograph of EOS Ti-6Al-4V *(Ti64)* powder used in this study.

The processing parameters users can control are laser power, velocity, hatch spacing, layer thickness, and baseplate temperature. Beam power and velocity are two of the primary variables, as they directly determine the size of the melt pool. The effect of these can be approximated by

the Rosenthal equation, which assumes pure heat conduction from a point heat source traveling at

constant speed in a straight line [15]:

$$T = T_{0+} \frac{Q}{2\pi kr} \exp\left(-\frac{V(\xi+r)}{2D}\right) \tag{2.1}$$

where T is the local temperature, T_0 is the initial temperature, Q is the adsorbed power from the

heat source, V is beam velocity, r is the radial distance from the beam, ξ is the distance from the

beam position along the travel direction, k is thermal conductivity, and D is thermal diffusivity.

When T is used as the melting temperature for a given set of beam and material parameters, a

semicircular profile approximating the melt pool size is attained. Hatch spacing is the programmed

center-to-center distance between two adjacent laser passes. Layer thickness is the distance the

build plate moves down between each new layer of deposited powder. Finally, the baseplate

temperature determines the preheat of the baseplate, with a maximum of 200 ˚C.

2.1.2 Electron Beam Melting

At the time of writing, Arcam AB supplies the only commercially available powder bed EBM

system. The machines utilized in this study, the S12 and A2X, use an electron beam generated

from a thermionic tungsten source accelerated to 60 kV as the heat source. The build chamber is

pumped to a vacuum of 5×10^{-6} mbar, before being backfilled to 2×10^{-3} mbar with high purity He

[16]. Powder is spread from hoppers on either end of the build plate using a rake. A high speed

preheat pass of the beam over the build plate acts to preheat the powder bed to a desired

temperature (~700 ˚C), and partially sinter the powder to prevent "smoking", or the expulsion of

powder away from the beam during the melting pass. To further reduce "smoking", these machines

use larger powder than the EOS laser based machines, with a diameter range of approximate 45-

100 μm. A backscatter SEM micrograph of the Arcam-supplied plasma atomized Ti6Al4V powder

is shown in Fig. 2.3.
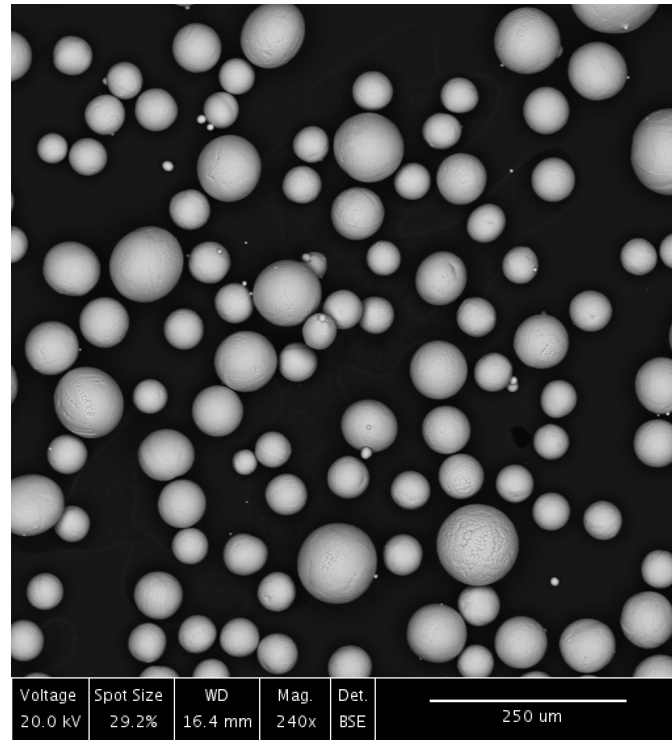
Figure 2.3: Backscatter-mode SEM micrographs of Arcam supplied Ti6Al4V powder fabricated by plasma atomization.

User controlled processing parameters are summarized in Table 2.1. Unlike the EOS system which give control of individual processing parameters, these systems use a proprietary control software that limits user input. Instead of power and velocity, a *speed function* variable is used to control velocity and current, so as to keep melt pool size constant. The current controls the applied power along with the fixed accelerating voltage by:

$$P = I * V \tag{2.2}$$

where P is the beam power, I is the current, and V is the accelerating voltage (60 kV).

2.2 Defects in Powder Bed Additive Manufacturing

This section describes the different defect formation mechanisms for metal powder bed additive manufacturing currently described in the literature. In addition to AM, defects in the related fields of welding and powder metallurgy are also considered.

Table 2.1: Process parameters for Arcam EBM system

Processing Parameter	Definition
Speed Function	Proprietary unit-less variable used to control beam velocity.
Focus Offset	Shift in baseplate vertical position used to control spot size.
Line Offset	Distance between adjacent melt pool passes, equivalent to hatch spacing.
Layer Thickness	Distance build plate moves down between subsequent powder layers.
Preheat Temperature	Target baseplate temperature.

2.2.1 Raw Materials Defects

Most commercial powder-bed machines are sold to end-users with a set of experimentally derived process parameters that work for the specific powder supplied by the machine manufacturer. Because of this limited choice in raw materials, the influence of different powders on porosity in the resulting parts is often overlooked. Because of the preference of spherical powders for AM, these powders are usually fabricated with some form of inert gas atomization [17]. The presence of trapped inert gas in atomized metal powder is a well-established source of defects in powder metallurgy (Fig. 2.4) [17], [18]. These gas pores are the result of the inert atomization gas used to prevent oxidation during powder fabrication getting trapped as bubbles inside the solidifying particles. These pores are transferred to the powder metallurgy components during the solid-state consolidation processes employed by this type of manufacturing.
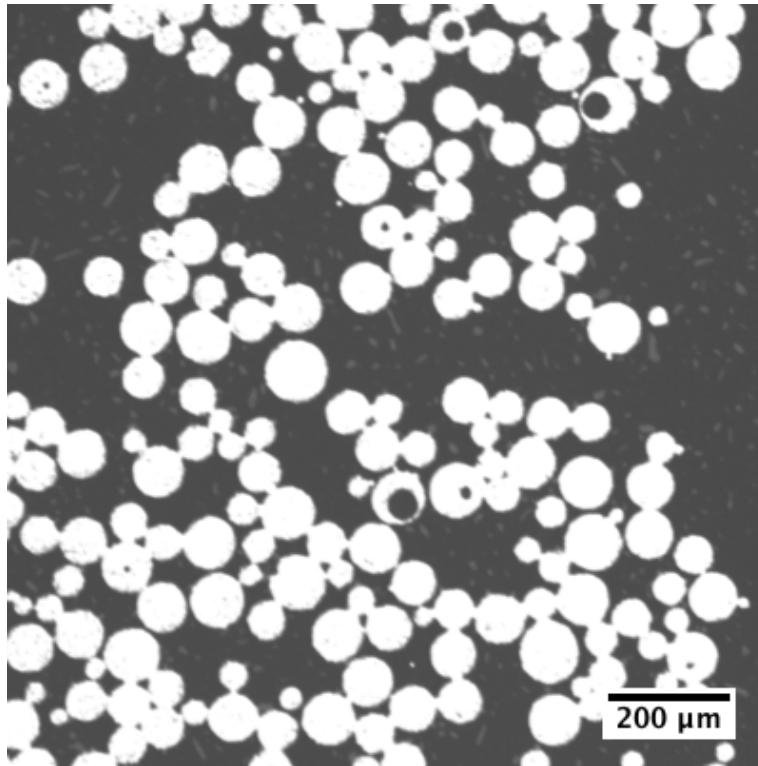
Figure 2.4: Optical micrograph of cross section of plasma atomized Ti-6Al-4V powder showing internal porosity.

This same powder porosity is frequently cited as a source of defects in AM metals [3], [10], [19], [20]. However, because these powder-bed AM processes are full melting processes, the mechanism of pore transfers from the powder to the as-built part is less straightforward and infrequently discussed. In-depth characterization of this porosity was performed by Tammas-Williams *et al.*, where they identified spherical pores in both the powder and as-built Arcam EBM Ti-6Al-4V using X-ray microtomography (μXCT) [3]. Because of the vacuum atmosphere in the EBM process, and the high solubility of contaminant gases such as oxygen in titanium, the pores in the as-built condition were attributed to the initial powder porosity. The mechanism put forth was that because the Marangoni-induced convection in the melt pool is acting to drive the pores to the bottom of the melt pool is greater than the buoyancy forces acting to help the pores escape

to the surface, pores would tend to remain at the bottom of the melt pool and have a better chance

of being trapped during solidification [19]. Marangoni flow (3) is surface tension driven liquid

flow that arises from the large temperature gradient because of the hot material directly under the

heat source given by:

$$v_{Mar} = \frac{2}{3}\left(\frac{r}{2\eta_{Melt}+3\,\eta_{Gas}}\right)\left(\frac{d\gamma}{dY}\right)\left(\frac{dY}{dT}\right) \tag{2.3}$$

where Y is distance, η_{Melt} is the viscosity of the melt, η_{Gas} is the viscosity of the gas, γ is the surface

tension of the melt, and T is temperature [21]. Under these conditions and the negative coefficient

of surface energy with temperature expected for pure materials, the material under the beam is

heated and has a lower surface tension than the surrounding liquid in the melt pool, so it flows out

towards the melt pool periphery and down, whereas the material at the bottom of the melt pool

rises. It should be noted that in materials that contain surface active elements, notably sulfur in

steel, this coefficient reverses sign over some range of temperature, and the flow direction similarly

reverses [22]. In the other direction, buoyancy is governed by the Stokes equation (4), and is driven

by the density difference between the entrapped gas and the melt [23]:

$$v_{Buoy} = \frac{2g}{9}\left(\frac{\rho_{Melt}-\rho_{Gas}}{\eta_{Melt}}\right)r \tag{2.4}$$

where g is the acceleration because of gravity, ρ is the density, and η is the viscosity. It was also

reported that pores in the as-built part were larger than those observed in the powder, possibly

through coalescence at the bottom of the melt pool, or expansion because of the low pressure

environment [3].

While it is usually dismissed in AM literature, studies on electron beam welding have cited

absorbed carbon, oxygen and hydrogen on plate surfaces as a source of porosity for titanium alloys

[24]–[26]. This contamination is believed to be concentrated at the abutting plate surfaces, as

surface preparation has been shown to affect the resulting porosity [24]. Residual gas analysis

highlighted hydrogen as the main gas contained in the pores [26]. The increased surface area provided by the powder in AM has the potential to provide a source of contamination. However, beam velocity was observed to strongly affect the presence of porosity, with peak porosity at speeds far below those used for AM, so it is unclear whether this type of porosity is a significant contributing factor.

2.2.2 Processing Defects

Processing defects refer to defects formed during the additive manufacturing process that are generally attributed to incorrect processing parameters. This is commonly simplified into two extremes, Fig. 2.6; a too low energy input results in insufficient melting or "lack of fusion" (LOF) porosity, whereas a too high energy input causes "keyholing" [2], [27], [28].

Lack of Fusion (LOF)

LOF porosity is the most frequently discussed defect, because its large size and irregular morphology makes it particularly deleterious to mechanical properties [27], [29]–[33]. However, the mechanism behind its formation is well understood and documented [34]–[36], so it will not be a focus of this study. The general concept to avoid lack of fusion can be summarized by considering a simple geometric model consisting of two transverse cross sections through parallel melt tracks, Fig 2.5. Under conduction-mode melting conditions [37] this can be considered to be two semicircular cross sections with a center to center distance equal to the hatch spacing, h. In order to sufficiently melt all of the material the hatch spacing needs to be small enough for a given melt pool size so that the overlap depth, d_O, is greater than the layer thickness of the powder.
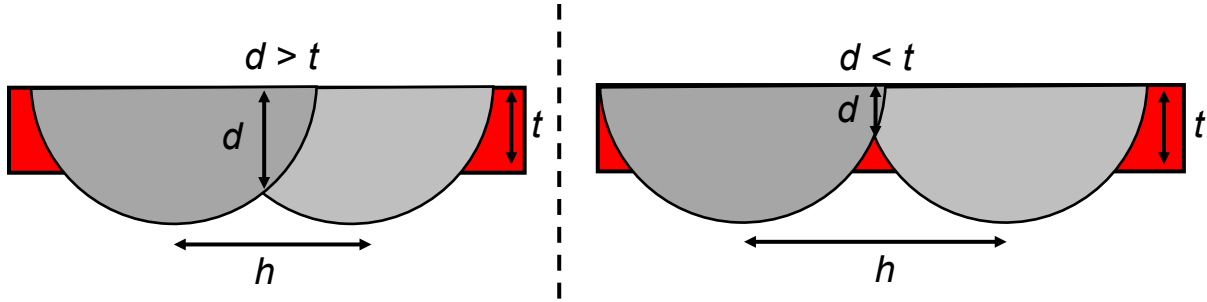
Figure 2.5: Schematic of factors that determine lack of fusion between adjacent weld tracks. *d* is overlap depth, *t* is the layer thickness, and *h* is the hatch spacing. Lack of fusion is avoided provided *d > t* [36].
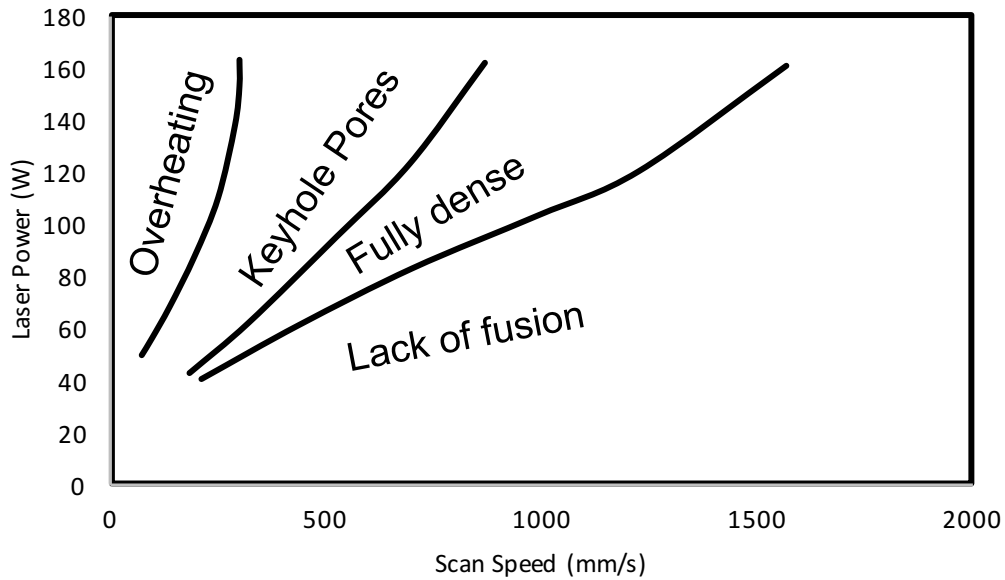
Figure 2.6: Experimentally derived process map for Ti-6Al-4V on an EOS M270 laser powder bed machine showing regions of defect formation for a layer thickness of 30 μm. Adapted from Gong *et al.* [2].

Conduction to Keyhole Transition

As discussed in the previous section, the energy delivered by the beam needs to be sufficient to form a sufficiently large melt pool to fully overlap the underlying material and adjacent melt pools. This effectively puts a lower-bound on melt pool size for a given hatch spacing/layer thickness and suggests the use of larger melt pools in order to have a sufficient factor of safety to account for variability and fluctuations in the melt pool dimension. However, at high enough energy

densities, on the order of 10^5 W/cm^2 [38], [39], a transition occurs where the melt pool changes from shallow and semicircular to deep and narrow. In welding, these two regimes are referred to as conduction-mode and keyhole-mode melting, respectively[37]. The latter regime is believed to be initiated by the strong vaporization of the liquid metal, which causes a deep, narrow vapor cavity ("keyhole") to form within the melt pool under the laser [28], [38]. While it is easy to distinguish the two modes of melting at sufficiently low or high energy density conditions, the transition between the two is still contested. Although keyhole modes can be effectively utilized to make deep penetration laser welds, for AM it is avoided as it has the propensity to generate porosity, which will be discussed in a later section. Therefore, this transition, as well as the post-transition behavior of the vapor depression in process conditions relevant to AM are the focus of this study.

Keyhole Transition in Spot Welding

Experiments conducted for laser drilling or "spot welding" present simplified conditions for analyzing this transition, as the beam is stationary. Previous investigations into the keyhole transition in spot welds generally agree that the mechanism behind this transition involves the competing forces of surface tension acting to keep the liquid melt pool surface flat, and recoil pressure generated by the localized vaporization of the liquid metal under the laser. When the recoil pressure exceeds the surface tension, the liquid is pushed away and a depression is formed in the surface [40]–[43]. In previous experiments, this transition has been identified by evidence of liquid expulsion [40], deposition of metal vapor and droplets above the melt pool surface [41], or high speed visible light imaging [42].

Many authors associate the initiation of a vapor depression/keyhole with the point at which the liquid under the beam reaches a temperature at or above its boiling point, but the details are

contested [42], [43]. As described by King et al. and Trapp et al. [28], [44], for a stationary

Gaussian beam, the time-dependent temperature under the beam center can be calculated by [45]

$$T = \frac{AI_L 2w_O}{k\sqrt{\pi}} tan^{-1} \frac{\sqrt{4Dt}}{2w_o} \tag{2.5}$$

where A is the absorptivity, I_L is laser intensity, w_o is laser spot radius, κ is thermal conductivity,

D is thermal diffusivity, and t is time. For a Gaussian beam, laser intensity is given by

$$I_L = \frac{2P}{\pi(2w_o)^2} \tag{2.6}.$$

Solving for time for $T=T_b$ (T_b = boiling point) gives a critical time to initiate the keyhole transition

for a given laser intensity

$$t_{KH} = \frac{(2w_0)^2}{4D} tan^2 \frac{\sqrt{\pi}\kappa T_b}{AI\sigma} \tag{2.7}.$$

This critical time serves as the basis for estimating the transition for a moving beam with a velocity

v through the estimated dwell time of the laser, t_d, where

$$t_d \sim \frac{2w_o}{v} \tag{2.8}.$$

Keyhole Transition with a Moving Beam

As with spot welds, the often cited mechanism for the transition is when the recoil pressure

overcomes the surface tension forces when the material reaches the boiling point [28], [44]. King

et al. [28] also described a normalized enthalpy criteria based on Hann et al. [46] where the

conduction-to-keyhole transition should occur based on a critical velocity u when

$$\frac{\Delta H}{h_s} > \frac{\pi T_b}{T_m} \tag{2.9}$$

where T_b and T_m are the boiling and melting points, and $\Delta H/h_s$ is the normalized enthalpy equal to

$$\frac{\Delta H}{h_s} = \frac{AP}{h_s\sqrt{\pi Du(2w_o)^3}}$$

(2.10)

where A is absorptivity, P is power, h_s is the enthalpy of melting, D is thermal diffusivity, u is the critical velocity, and w_o is the laser spot radius. However, their results indicated that the observed threshold was approximately five times the estimated threshold, which is a substantial difference.

The challenge with experimentally describing the keyhole transition with a moving beam lies in defining a threshold. In most welding and AM literature, an arbitrary depth-to-width ratio of the melt pool transverse cross section is chosen, corresponding to an obviously non-semicircular shape [28], [44], [47], which represents an indirect measurement. Where high-speed visible light imaging is used, the formation of a vapor depression in the top surface of the melt pool has also been used to categorize the threshold [44]. Occasionally, a transition region is described between the two regimes, where a depression is formed but the melt pool remains semicircular [47]. The variety of definitions for this transition makes it clear that sufficiently high fidelity characterization techniques have not been available or applied to investigate the dynamic behavior of this transition.

Post-Transition Behavior and Defects

Keyhole-mode melting has been exhaustively investigated by the welding community [38], [48]–[52]. Once the keyhole regime is active, the absorptivity and resulting melt pool depth for a given energy density is observed to increase dramatically [44]. It has been suggested that this is the result of an increasing aspect ratio (of the vapor depression) absorbing more of the laser light via multiple reflections [53]. Fabbro *et al.* discussed the potential consequences on keyhole morphology as a function of process parameters such as beam velocity [52]. However, while there are many parallels between laser welding and LPBF, the latter operates at considerably higher beam velocities (~ 1000 m/s vs. 20 mm/s) and smaller spot sizes (~100 μm vs 1 mm). The consequences

of operating in this region of process space have not been thoroughly investigated. For example, Trapp et al. observed that the increase in absorptivity once in the keyhole regime behaved differently at high velocities, which was further complicated by the addition of powder [44].

For the purpose of this study, the main concern of operating in keyhole mode is the potential formation of porosity, which is believed to form when fluctuations in the vapor cavity lead to a collapse and the entrainment of vapor in the melt pool [54], [55]. In-situ x-ray radiography has proven useful in investigating the keyhole morphology and behavior of laser welds, but previous efforts focused on the process space relevant to welding and had a limited penetrating power and frame rate because of reliance on lab-scale X-ray sources [50], [51], [56]. Atmosphere has also been shown to play a significant role in the formation of porosity, with a vacuum significantly lowering the presence of keyhole pores in Ti-6Al-4V in laser welds [55], [57].

Comparatively little work has been done for LPBF, and almost none for EBM. King *et al.* observed the transition from conduction to keyhole mode in laser powder-bed AM, with the associated porosity, for single track experiments in 304 stainless steel [28]. Recently, advanced multi-phase simulations on laser powder bed AM have supported the cavity collapse mechanism of pore formation, while also suggesting additional vapor depression related pore formation mechanisms including vortex liquid flows following the vapor depression that may enable bubbles to form, as well as end-of-track pores because of the sudden shutdown of the beam and subsequent collapse of the vapor cavity[58]. The issue of end-of-track pores was further investigated by Groeber et al. and has been identified as a potential major source of defects even if the main pass is free of pores that form while the beam is moving [59]

2.2.3 Post-Processing Defects

Because of the propensity for defects in AM parts, a hot-isostatic press (HIP) treatment is frequently applied to reduce the number and severity of internal defects. HIPing involves the application of high pressure and temperature in an inert environment, which acts to shrink the size of internal defects through the reduction of surface energy and unbalanced internal and external pressure [60]. The process needs to occur at a sufficiently high temperature and pressure to allow the material to deform via creep and collapse the pores, and if the gas is soluble, allow it to diffuse out of the pores. Studies have shown the effectiveness of HIPing to reduce porosity in AM components [5] and the subsequent improvement on elongation and fatigue life [33]. However, the extended time at high temperature can cause considerable microstructural coarsening, resulting in reduced strength and unfavorable microstructures. Post-HIP heat treatments such as a β-solution heat treatment for Ti-6Al-4V, or solutionizing and aging treatment for IN 718, may be employed to reach a final desired microstructure.

The problem arises when pores containing inert gas such as argon are HIPed and then subsequently exposed to high temperature. Argon pores have been observed to regrow following high temperature heat treatments after HIPing in a process known as thermal induced porosity, and be significant enough to often cause a degradation in mechanical properties [11], [61], [62]. This process is the result of heating the now pressurized pore from the HIP process to temperatures that allow the surrounding material to deform via creep. Such processes are well studied, and are used to make titanium foams [12], [63], [64]. The question is not whether or not this will occur with AM metals, but whether or not AM defects contain sufficient inert gas to regrow to appreciable sizes at temperatures relevant to heat treatments. Tammas-Williams *et al*. observed this behavior with porosity in EBM Ti-6Al-4V attributed to the starting powder, and that the extent of regrowth

was largely controlled by temperature rather than time [9]. To date this has not been investigated

for processing flaws in AM such as keyholes or lack of fusion, but in the case of LPBF, both could

feasibly contain inert gas from the atmosphere, as shielding gas was detected in keyhole pores

laser welding [50], and lack of fusion porosity is open to the atmosphere before being closed off

by subsequent layers.

Chapter 3: Experimental Methods

This section describes the two main experimental characterization methods utilized in this study. This includes synchrotron-based x-ray microtomography (μSXCT) and Dynamic X-ray Radiography (DXR). All experiments were conducted at Argonne National Lab's Advanced Photon Source synchrotron.

3.1 Synchrotron Based X-ray Microtomography (μSXCT)

X-ray micro-tomography (μXCT) has been used effectively in characterizing defects in welds [54], [57], and it is increasingly become the tool of choice for investigating defects in AM materials [3], [65]–[69]. This is largely because the quantitative characterization of the different types of defects found in AM components (e.g., lack of fusion, gas porosity, key-holing) requires significant information on spatial distribution and morphology that is difficult to achieve through traditional means of cross section analysis or bulk density (Archimedean density, ultrasonic inspection) [2][70]. In contrast to these methods, μXCT is a non-destructive (at least to the small sample) technique that provides 3D information on internal defects by the reconstruction of a series of radiographs taken as the sample rotates over 180˚ or 360˚ [71]. Recently, synchrotron-based micro-tomography (μSXCT) has been applied to AM for its increased level of detail [28], [35], as the high energy x-rays provide large penetration, a high signal to noise ratio, rapid data acquisition, as well as sub-micron voxel resolution [72].

The μSXCT experiments in this work were performed at the 2-BM beamline at Argonne National Lab's Advanced Photon Source. A schematic of the setup in shown in Fig. 3.1. A sample with a through-thickness less than 2 mm is placed on a 4-axis stage in line with the x-ray beam and detector at a specified detector-distance, with the axis of rotation parallel to the scintillator

screen and camera. A white x-ray beam (60 keV peak energy) with 10x optics was used for these experiments, achieving a voxel size of 0.65 μm. A CCD camera and 20 μm Lutetium Aluminum Garnet (LuAG) scintillator were used to collect 1500 radiographs of the sample as it is rotated 180˚, each with an exposure time of approximately 100 ms. Additionally, images are collected with the sample removed from the field of view (flat images), and with the beam off (dark images) for use in background subtraction. This process is able to capture a ~1.5 mm^3 scan volume in ~ 4 minutes.
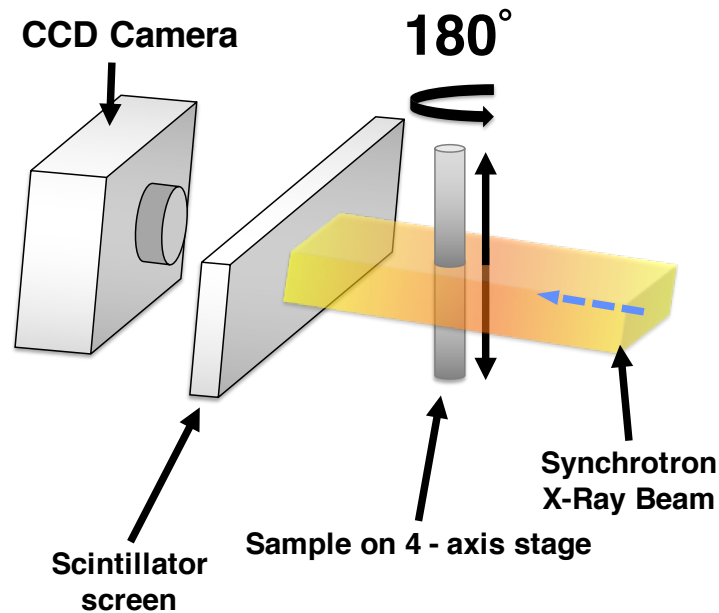
Figure 3.1: Schematic diagram of μSXCT setup at 2-BM beamline at Argonne National Lab's Advanced Photon Source

The radiographs are filtered and reconstructed using TomoPy, a software package supplied by APS [73]. TomoPy is a python based package that provides preprocessing in the form of artifact removal, as well as image reconstruction through the Fourier-based GridRec method [74]. Before reconstruction, a number of filters are applied to remove noise caused by damage to the camera or scintillator. First, a median filter is applied to each radiograph to remove abnormal pixels (zingers) caused by bad pixels or background x-rays. An image division step using the flat and dark images

(4) is then applied to the radiographs that serves as both a background subtraction for further artifact removal and normalizes the image intensities from 0 to 1.

$$I_{Norm} = \frac{I_{Raw} - I_{Dark}}{I_{Flat} - I_{Dark}} \tag{3.1}$$

Any remaining artifacts from the detector or scintillator screen will appear in the reconstruction as crescent shapes, or "ring artifacts", as the affected pixels do not change as a function of rotation angle. These are readily detectable, as they form a vertical line on the sinogram (pixel intensity vs. rotation angle). A combined wavelet-FFT filter is applied to remove the lines from the sinogram, returning the final corrected radiographs for reconstruction [75]. The effect of these filters on reconstruction quality is illustrated in Fig. 3.2.
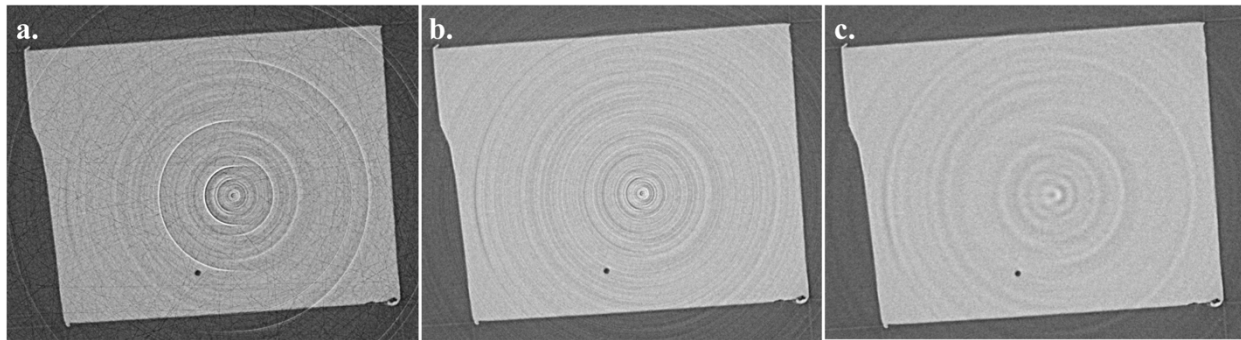
Figure 3.2: Reconstructed slice of AM Ti-6Al-4V showing effect of filters. a. without zinger removal or stripe removal, b. with zinger removal, and c. with zinger and stripe removal.

Tomographic reconstruction is performed using the Fourier-based GridRec method [74], resulting in stacks of images like those seen in Fig. 3.2. Post-reconstruction analysis including segmentation and porosity analysis are completed using Avizo 9 software.

3.2 Dynamic X-ray Radiography (DXR)

Note: This section is adapted from: Parab et al., J Synchrotron Rad.(2018, submitted) [76]

Early efforts to perform in-situ investigations on defect formation mechanisms in laser welding using lab-scale transmission x-ray radiography and a high speed camera were performed by Katayama *et al*. [56], [77]. A new experimental setup has been developed at Argonne National Lab's Advanced Photon Source to perform similar experiments utilizing the significantly greater flux and time resolution of synchrotron X-rays to investigate the dynamic processes occurring during LPBF. A schematic of the setup is shown in Fig. 3.3. These experiments were performed at the 32-ID beamline at Argonne National Lab's Advanced Photon Source synchrotron.
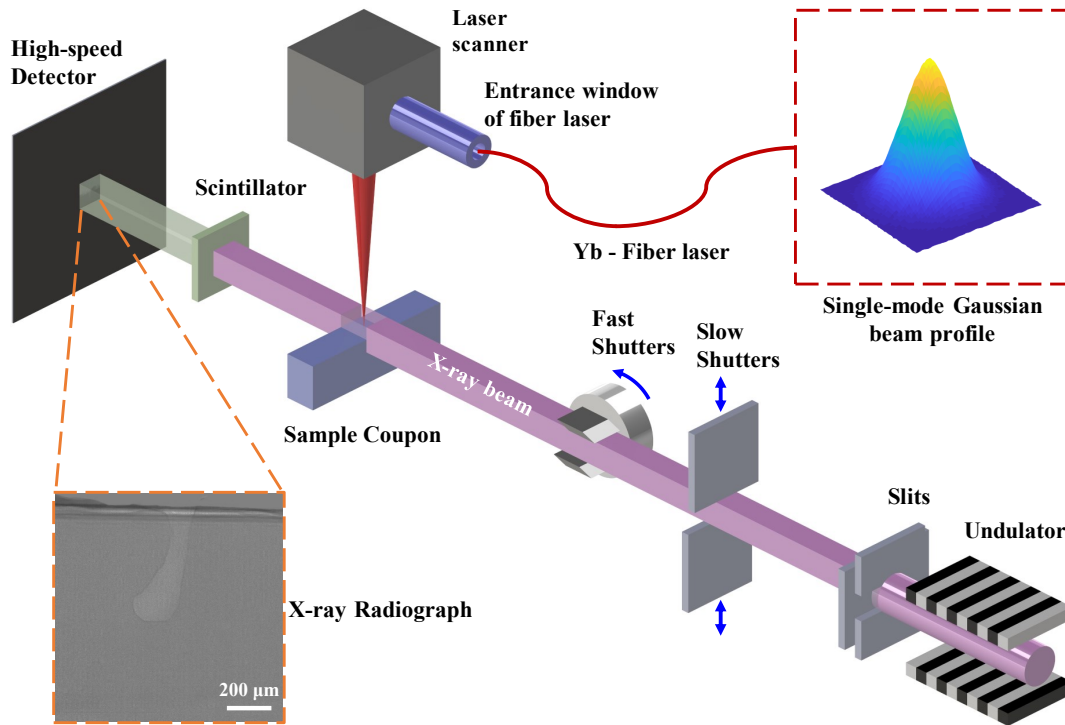
Figure 3.3: Schematic of experimental setup for Dynamic X-ray Radiography experiments at the 32-ID beamline.

3.2.1 Laser setup

The laser system consisted of a ytterbium fiber laser source (IPG YLR-500-AC, IPG Photonics, Oxford, MA USA) combined with a laser scanner (Intelli*SCAN*$_{de}$ 30, SCANLAB Gmbh., Puchheim, Germany). The fiber laser provided pure Gaussian beam profiles and was operated in single-mode. The wavelength and maximum power of the laser were 1070 nm and 520 W respectively. All experiments in this study were performed in the CW mode. The scanner manipulates the laser beam using a system of rotating mirrors driven by galvanometers. The specified maximum scan speed was 0.7 m/s, although higher scan speeds up to 1.2 m/s were achieved and verified through direct measurement via DXR (high speed radiography).

Beam parameters were controlled using a proprietary software (laserDESK, SCANLAB Gmbh., Puccheim, Germany). The laser was either operated in "line scan" mode where the laser was translated in one or multiple straight lines along the top of the sample, or in "spot beam" mode where the laser was stationary and exposing the surface for a set time at a single location.

At the focus, the spot size (diameter) can be calculated from the laser optics by

$$2w_o = \frac{f * l_o}{l_c} \tag{3.2}$$

where w is the beam radius, f is the fiber diameter = 14 μm, l_c is the collimator focal length = 85 mm, and l_o is the objective lens focal length = 340 mm, resulting in a focal spot size of 56 μm. In order to more accurately represent the conditions of the LPBF systems, which operate with a beam diameter of ~100 μm, the experiments were experiments were performed off-focus, with the surface of the sample located below the focal plane. A beam profiler was not available prior to the experiments included in this work, so approximate off-focus beam sizes were measured via direct

observation of the keyhole opening width in spot beam experiments, and compared to the theoretical beam diameter based on the equation

$$w(z) = w_0 \left(1 + \left(\frac{\lambda z}{\pi w_0^2} \right) \right)$$
(3.3)

where w is the beam radius at distance z from the focal point, w_0 is the beam radius at focus (28 μm), and λ is the wavelength of the laser (1070 nm). The experiments in this work used spot sizes of approximately 95 μm, 115 μm, and 140 μm +/- 10 μm, corresponding to distances below the focal plane of 2.5, 3.5, and 4.5 mm. The measurement of the beam spot sizes is discussed in Appendix B.

3.2.2 Specimen chamber

The specimen chamber consisted of a stainless-steel vacuum chamber. A fused silica window was located on the top of the chamber for the laser beam to pass through. The laser scanner was located on the top of the window, which was separated from the top of the chamber by a vacuum flange with a length of 350 mm. This length was selected such that the distance between the scanner and the sample was approximately equal to the working distance of the scanner f-theta lens. Two additional viewports were incorporated in line with X-ray propagation direction and were sealed using 127 μm thick Kapton film. The chamber was connected to a mechanical vacuum pump and a fill line from an argon cylinder for pumping and purging the chamber. A pressure transducer was attached to the same connector to gauge the pressure inside the chamber. The vacuum pump was capable of pumping the chamber to a low vacuum pressure of ~100 mtorr. After pumping out, the chamber was back-filled with argon to atmospheric pressure.

The translational stage assembly was composed of three single-axis translational stages equipped with stepper motors. A vertical post was fixed on the stage assembly and fed through the

bellows into the chamber. The horizontal translational stage assembly was used to align the specimens with the laser spot. The vertical stage was used to control the distance between the scanner and the specimen, which controlled the laser spot size. The chamber and the translation stages were placed on top of heavy-duty vertical and horizontal stages, which were used to align the laser with the X-ray beam.

3.2.2 Sample setup

Experiments were either performed directly on the plate or on simulated powder beds. The plate samples, or equivalently the substrates in the case of the powder beds, were machined from larger plates into coupons that were were 2.9 mm high, 50 mm long, and either 400 μm or 800 μm thick. The specimens were stood up in the vertical position. For the simulated powder bed experiments, the substrate was sandwiched between two glassy carbon plates, as seen in Fig. 3.4. A uniform layer of powder ~ 100 μm thick was spread manually on top of the metal base. Both plate and powder bed samples were maintained at room temperature prior to the experiment.
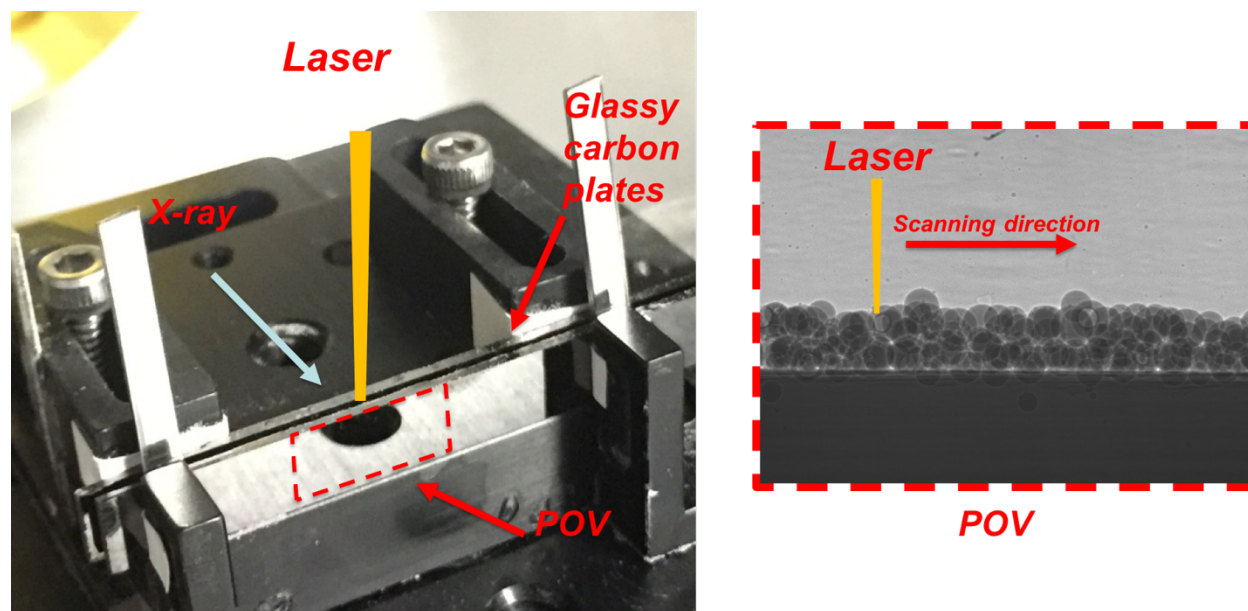
Figure 3.4: Sample setup for simulated powder bed sample for dynamic x-ray radiography. Beam-on-plate experiments were run on the same setup but omitted the glassy carbon plates.

3.2.3 High-speed X-ray imaging

The high-speed synchrotron X-ray imaging experiments were performed at beamline 32-ID-B at the Advanced Photon Source located at Argonne National Laboratory. The schematic of the beamline setup in shown in Fig. 3.3. A short-period (18 mm) undulator with the gaps set at 14 mm was used for the experiments, which provides a polychromatic X-ray beam with a 1st harmonic (~96 % of the flux) energy of ~24.4 keV. A set of horizontal and vertical white beam slits were used to collimate the X-ray beam as well as control its size. For the current experiments, the slit dimensions were typically set to 1.5 mm × 1.5 mm.

The recorded X-ray images contain both absorption and phase contrast. Absorption contrast stems from the difference in transmitted X-ray intensity as they are attenuated by materials of different densities as they pass through the sample [78]. X-ray phase contrast results from changes in the phase pass through materials with different refractive indices. Compared to absorption contrast, this can provide improved edge contrast, particularly for lighter materials and

interfaces [79], [80]. A single crystal $Lu_3Al_5O_{12}$: Ce scintillator was used to convert the transmitted X-rays to visible light. These are subsequently relayed to the high-speed camera (Photron FastCam SA-Z, Photron Inc., Tokyo Japan) through a 45° mirror, a 10X microscope objective, and a tube lens. Video recordings were taken at either 400 kHz, 200 kHz, or 50 kHz. Operating at higher frame rates required a reduction in the area of the field of view of the camera due to limited memory and readout speed. Corresponding field of view dimensions for the 400 kHz, 200 kHz, or 50 kHz frame rates are approximately 240 μm x 256 μm, 464 μm x 512 μm, and 2048 μm x 512 μm respectively.

3.3.4 Image Analysis

Because of the large number of images produced in each experiment and the rapid acquisition time, automated image analysis process was developed to extract necessary information from the images. Some preprocessing of image stacks was done using ImageJ prior to automated processing. For the purposes of these experiments, the automated analysis only needed to capture the maximum depth of an interface (e.g., solid/liquid for melt pool, or gas/liquid for vapor depression). In order to simplify the approach, the movies were compressed into a two dimensional array of maximum depth and time. If one imagines each movie as a three dimensional array with time as the z-axis, the projection is done such that the resulting projected image is the maximum depth for a given time step determined by the frame rate. An example of a compressed image in shown in Fig. 3.5. Following this, a simple analysis was performed to find the point along each column of pixels met the user-defined threshold (Appendix A).
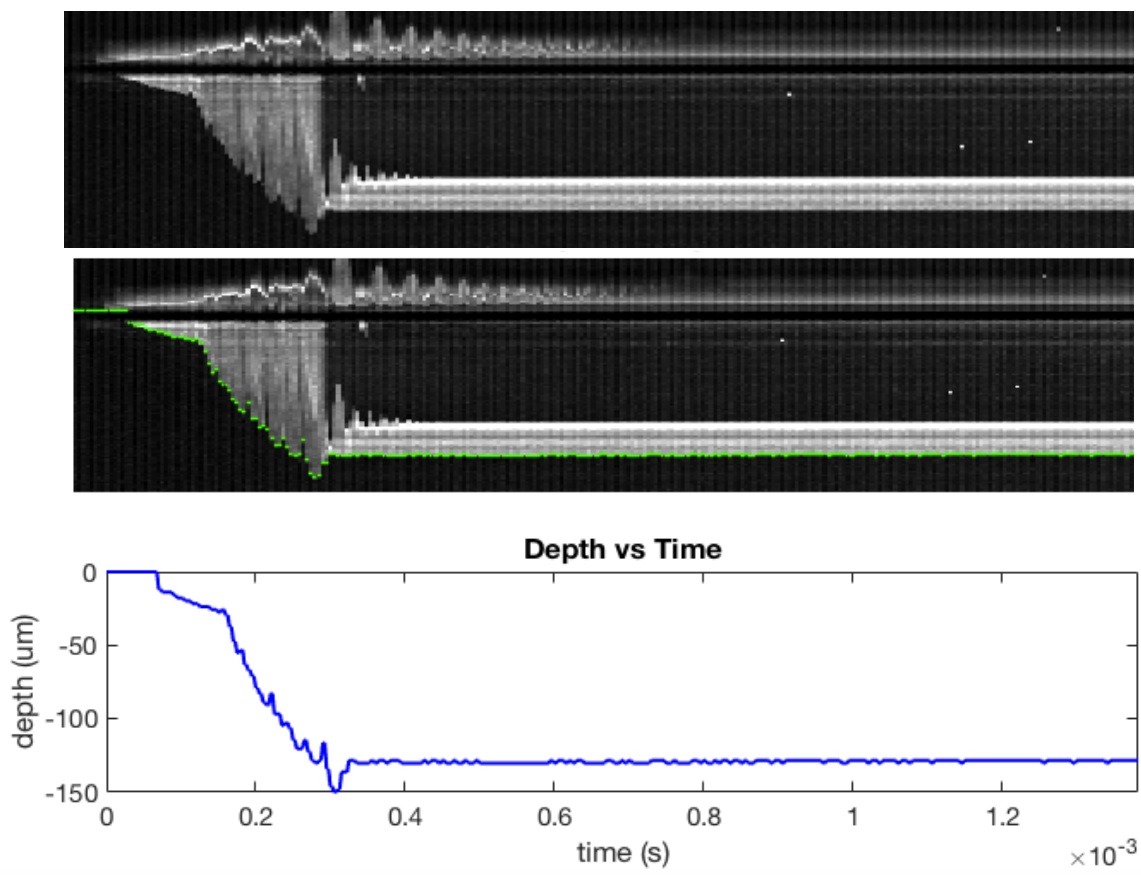
Figure 3.5: Image analysis for determining maximum vapor depression depth as a function of time.

Chapter 4: Transfer of Porosity Contained Within the Powder

This chapter investigates the potential contribution of inert gas contained within the powder to the as-built part, and the circumstances under which this transfer occurs. The majority of experiments were conducted using the Arcam EBM process, as the vacuum atmosphere minimizes potential other sources of gas compared to the inert environment of the LPBF process. A preliminary investigation using the μCT compares the pore populations in two starting powders to the porosity in as-built parts build from their respective powder. Additionally, the effect of processing parameters, specifically *speed function* in the Arcam process, on the propensity to transfer pores is investigated. Finally, the in-situ experiments seeking to observe and understand the pore transfer process were performed. These collective results demonstrate that pores from the starting powder can be a significant contributor to the defect population in as-built parts, but that there are methods to reduce their population and size through process parameter control. A specific circumstance that enables the transfer of pores from the powder particle to the melt pool is also proposed.

4.1 Effect of Internal "Trapped Gas" Porosity in EBM Ti-6Al-4V

Note: This section is largely reproduced from: Cunningham, et al. MRL.(2017) [81].

To examine the contribution of internal powder porosity on the as-built defect population in metal powder-bed AM, the porosity in as-built samples of EBM Ti-6Al-4V built from two different powders with widely different internal porosity was compared using μSXCT. EBM Ti-6Al-4V was used because the EBM process is carried out in vacuum, thus limiting the sources of gas in the experiment. Test blocks were fabricated by Northrup Grumman using plasma atomized Arcam Ti6Al4V ELI powder from AP&C, and Plasma Rotating Electrode Process (PREP) powder from TIMET on an ARCAM A2X. PREP powder is generally accepted as having lower internal porosity

compared to other powder manufacturing methods, as it does not employ an atomization gas, but it is fabricated in an inert gas environment [17]. Compositions provided in the powder quality certifications are given in Table 4.1. Often different processing parameters are required when changing powders to accommodate necessary changes in layer thickness, but this has been shown to affect both the gas and lack of fusion porosity present in the sample [3], [4]. To limit this effect, the powders used in this study had approximately the same size range, albeit with different size distributions. Particle size distributions measured via SEM images taken on a Joel 5900 and Genesis Particle analysis software are given in Fig. 4.1. Additionally, the same processing parameters and version of machine were used for both; in this case, the manufacturer recommended parameters for Ti-6Al-4V in an ARCAM A2X (see Table 4.2) were used. Synchrotron imaging samples were sectioned via EDM from the bulk specimens with 1 mm x 1 mm x 30 mm dimensions, with the long axis parallel to the build direction. Samples of the powders were sealed at tap density inside 1.5 mm Kapton tubing for μSXCT.

Table 4.1: Compositions of virgin Arcam Ti6Al4V ELI and TIMET PREP powder

Powder	Element (Wt. %)														
	Ti	Al	V	Fe	Y	C	O	N	H	Cu	Mn	Mo	Sn	Zr	Other
AP&C	Bal.	6.41	3.89	0.18	<0.001	0.01	0.08	0.02	0.001	-	-	-	-	-	<0.4
Timet	Bal.	6.09	3.98	0.17	-	0.02	0.18	<0.01	0.002	<0.01	<0.01	0.01	<0.01	<0.01	<0.05

Synchrotron x-ray microtomography was performed at the 2-BM beamline at the Advanced Photon Source at Argonne National Lab operating in white beam mode. A total of 1,500 projections were taken over 180° with a 100 ms exposure time resulting in approximately a 4 min scan time. A 0.65 μm voxel size (edge length) was obtained. The radiographs were reconstructed and filtered using TomoPy 0.0.3 [73]. Avizo version 9 was used for segmentation and analysis. A minimum of 8 face-connected voxels was used as the minimum feature size, establishing a minimum feature resolution of approximately 1.5 μm.
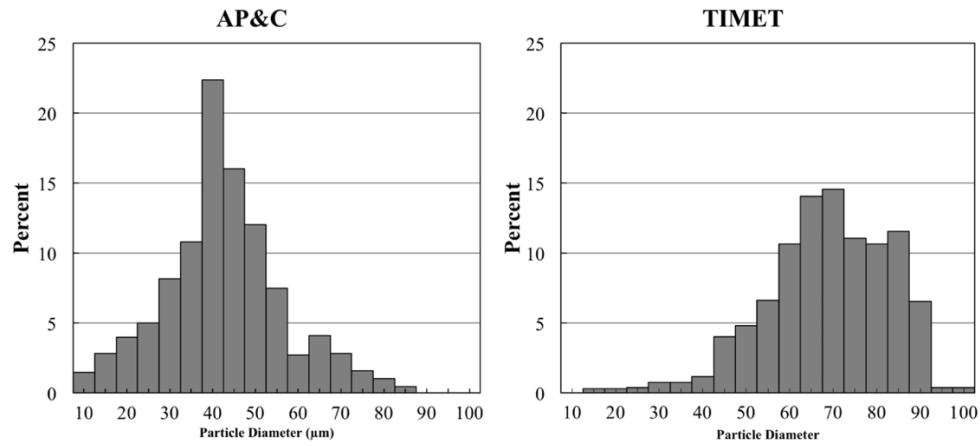
Figure 4.1: Number-weighted size distributions of powders used in this study measured via SEM image analysis and Genesis Particles software. [81]
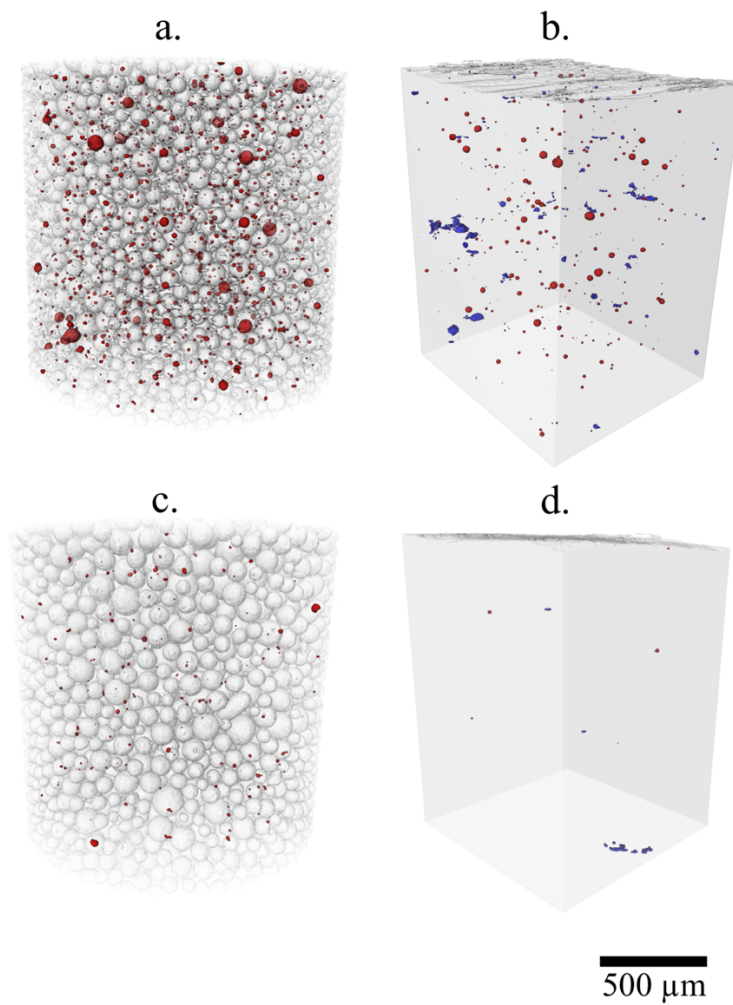
Figure 4.2: μSXCT results showing porosity in powder and samples built from AP&C (a,b), and TIMET (c,d) powders in an electron beam powder bed printer [82]**.**

Table 4.2: Standard processing parameters for Ti-6Al-4V on Arcam A2X

PreHeat			Focus Offset	125 +/- 75 mA
			Heating Focus Offset	250 +/- 150 mA
			Offset to Part	5 mm
		PreHeat 1	Max Beam Current	30 +/- 10 mA
			Beam Speed	11,000 +/- 3,000 mm/s
			Max No. Repetition	39 +/- 4
			Ave Current	14.8 +/- 4 mA
		PreHeat 2	Max Beam Current	38 mA max
			Beam Speed	11,000 +/- 3,000 mm/s
			Max No. Repetition	21 +/- 4
			Ave Current	16.8 +/- 4 mA
			Max Heat Time	28 +/- 7 sec
Melt	Contours = 3	Outer Contour	# Spots	50
			Spot Time	0.8 ms
			Multispot Overlap	0.5 mm
			Current	5 mA
			Focus Offset	Nominal Post Calibration +/- 10 mA
			Speed Function	6
		Inner Contour	Current	12 mA
			Focus Offset	0
			Speed Function	30
	Hatch		Current	17 mA
			Focus Offset	Nominal Post Calibration +/- 10 mA
			Speed Function	36
			Line Order	1
			Line Spacing	0.2 mm
	Heating		Max Heat Time	25 sec

The combined µSXCT results of are shown in Fig. 4.2. Relevant statistics are summarized in Table 4.3. The plasma atomized powder (Fig. 4.2a) has a significantly larger population and maximum size of porosity than the PREP powder (Fig. 4.2c), and is comparable to previously reported µXCT results from plasma atomized powder [3]. In the PREP powder, numerous pores were observed that had an irregular morphology inconsistent with the highly spherical gas porosity

frequently observed in the as-built condition. While more investigation is required to determine the nature of this porosity, the irregular shape suggests it may be shrinkage porosity, and therefore would not contribute to gas porosity in the as-built parts. For these reasons, only porosity within the powder with sufficiently spherical morphology to be realistically considered gas porosity (anisotropy < 0.5) was compared to the spherical porosity observed in the fabricated samples. However, highly spherical gas pores were still detected in the PREP powder, in contrast to the widely held belief that PREP powder is free of gas porosity. It should be noted that, in contrast to the trapped argon, the gas pores in the PREP build would likely contain helium, which is the gas used in most PREP powder manufacturing processes [17].

Table 4.3: Porosity statistics from of EBM Ti-6Al-4V samples built from AP&C & TIMET Powder

	Lack of Fusion				Gas Porosity				
	Volume Fraction $(x10^4)$	# Pores per mm^3	Ave. Eq. Diam.	Max Eq. Diameter	Volume Fraction $(x10^4)$	# Pores per mm^3	Ave. Eq. Diam.	Max Eq. Diameter	Margin of Error (%)
AP&C Powder	n/a	n/a	n/a	n/a	$9.59x10^{-2}$	892	11	72	3.3
AP&C As-Built	2.97	187	7.81	49	3.78	263	10	42	6.1
TIMET Powder	n/a	n/a	n/a	n/a	$6.82x10^{-3}$	68	10	33	12.1
TIMET As-Built	0.17	12	9	28	$2.27x10^{-2}$	7	7	13	37.8

μSXCT results of the as-built parts are shown in Figs. 4.2b and d. Multiple μSXCT scans were taken throughout the height of the samples, with no significant variation in porosity observed along the build direction, so the scans from the top ~1.5 mm were used to compare the samples. As with the powder porosity, pores were segregated by morphology, with low sphericity pores attributed to lack of fusion defects. Results show a similar trend in porosity to that of the powder, with the AP&C part having considerably more porosity. A comparison of the size distributions of pores in the powders and as-built samples is shown in Fig. 4.3.
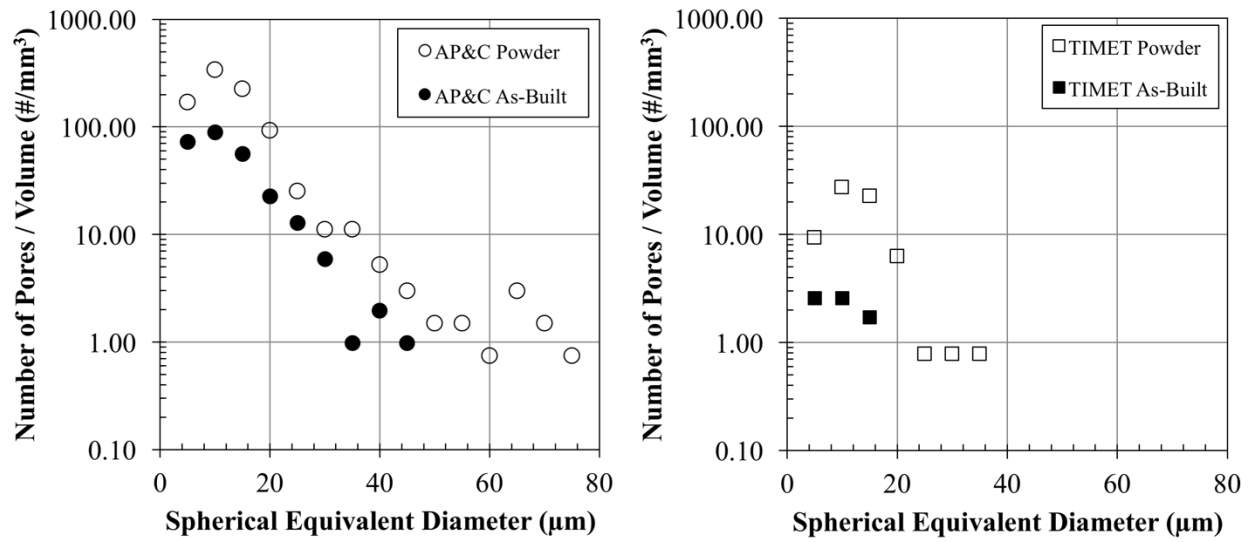
Figure 4.3: Size distributions of gas pores detected by μSXCT in Arcam EBM Ti-6Al-4V samples compared to porosity in AP&C and TIMET powder, expressed as number densities. [81]

4.2 Effect of Processing Parameters on Porosity in Arcam EBM Ti-6Al-4V

Note: This section is largely reproduced from: Cunningham et al. JOM (2016) [4].

The purpose of this study was to observe how porosity changed as a function of processing parameters, specifically the *speed function,* in EBM Ti-6Al-4V. Test blocks were fabricated on an Arcam A2 machine at North Carolina State University using Arcam Ti-6Al-4V powder. Because *speed function* is a unitless parameter, processing parameters variations were designed to vary the melt pool cross sectional area (normal to the direction of beam movement) in a systematic manner. Processing parameters were designed by Sneha Narra and Dr. Jack Beuth of Carnegie Mellon University. As shown in Table 4.4, melt pool cross sectional areas of 1, 2, 4, ½, and ¼ times the 'nominal value' were prescribed through changes in the Arcam *speed function,* where the 'nominal value' was the area using the parameters suggested by the machine manufacturer for Ti-6Al-4V.

The process mapping approach developed by Beuth *et al.* has demonstrated that process outputs such as melt pool geometry can be related to primary process variables including beam power and travel velocity for direct metal additive manufacturing [8]. Fig. 4.4 provides an experimentally derived plot of the variation of melt pool cross sectional area with speed function one which these parameters were based [83]. Accordingly, this relationship between speed function and melt pool cross-sectional area was used to vary the speed function for the test blocks given in Table 4.4.
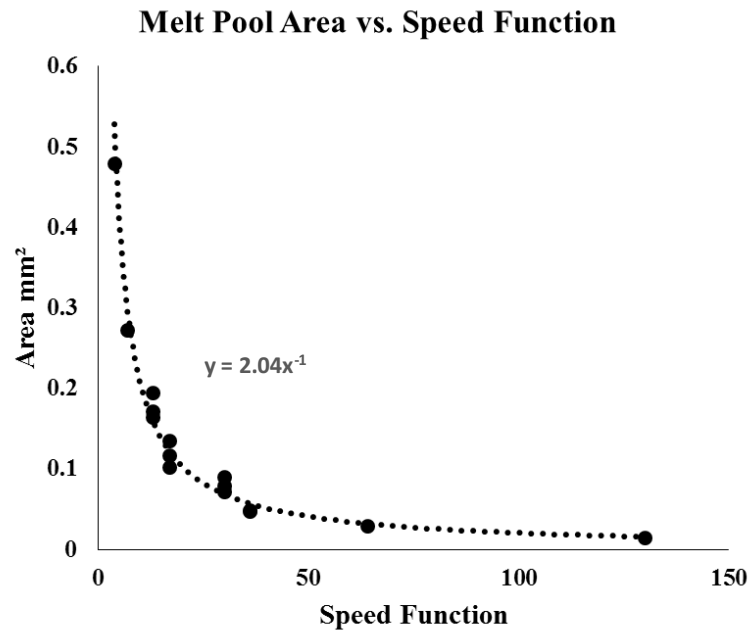
Figure 4.4: Experimentally derived plot demonstrating the relationship between melt pool cross-sectional area and speed function [83]**.**

Ti-6Al-4V test blocks (cylinders) with dimensions of 3 cm (diameter) x 1.5 cm (height) were fabricated from standard Arcam-supplied Ti-6Al-4V powder. Layer thickness, hatch spacing and start plate temperature were kept at the nominal values of 70 μm, 200 μm and 750°C respectively. The hatching direction was rotated by 90° after each layer was deposited. The nominal beam spot size available on the machine was used for all specimens, (which depends somewhat on the particular machine used and on the initial machine calibration). Tomography

specimens were then machined from the centers of each sample with dimensions of 1 mm x 1 mm x 15 mm with the long axis parallel to the build direction.

Table 4.4: Speed Function and resulting change in approximate melt pool cross-sectional area.

Approx. Relative Melt Pool Area*(Area/Nominal Area)	Speed Function (Raster)
1X	36
2X	20
4X	10
1/2X	72
1/4X	152
* Cross sectional area of melt pool perpendicular to travel direction	

Synchrotron X-ray microtomography was performed at the Advanced Photon Source at Argonne National Lab. The 2-BM beamline operating in 60 kV white beam mode was used in order to get sufficient contrast and penetration through the samples. 1500 projections were taken over 180° with a 100 ms exposure time resulting in approximately a 4 minute scan time. A 0.65 μm voxel size (edge length) was obtained.

The radiographs were reconstructed and filtered using TomoPy, a software package supplied by APS. Avizo 9 software was used for segmentation and generating the 3D reconstructions from the reconstructed images. Analysis was performed in order to determine pore shape, volume, and spatial distribution. Two scans were analyzed per sample, encompassing the regions from 0-1.5 mm and 6.5-8 mm from the final deposited layer surface. Morphology was determined using the 'anisotropy' function in Avizo 9 with a value of 0.7 being the cutoff for gas porosity. Any porosity found outside of this range was considered lack of fusion porosity. Because of the high resolution possible with synchrotron XCT, a minimum feature size of ~1.5 μm diameter was achieved. A minimum of 8 face-connected voxels were required in order to be considered a

valid feature. While there may be pores below this limit, they represent a very small volume fraction, and are likely inconsequential to mechanical properties.

Fig. 4.5 shows spherical porosity attributed to trapped gas observed in each region highlighted in blue. These results show a significant difference in porosity between samples of different melt pool area, as well as between heights of individual samples. Statistical data on the observed porosity is given in Table 4.5. Figs. 4.6 & 4.7 show the volume fraction and size distribution of gas pores in each sample. Additionally, the size distribution of pores observed in the Arcam Ti-6Al-4V powder in Section 4.1 is plotted in Fig. 4.7. The results show a considerable decrease in porosity as melt pool size increases. Gas pores above 10 μm are largely eliminated in the 2X and 4X samples, except for the very top of the sample. As melt pool size decreases, the observed size distribution of gas pores more closely resembles the size distribution of pores detected in the powder.

Table 4.5: Summary of gas pore statistics determined from XCT analysis.

Sample	Location*	Volume Scanned (mm³)**	Pore Count	Vol. Norm. Pore Count (#/mm³)	Volume Fraction (%)	Ave. Spherical Equivalent Diameter (μm)	Max Spherical Equivalent Diameter (μm)
1/4X	Top	1.32	342	259	.0314	8.42	42.9
	Middle	1.34	394	294	.0309	8.20	42.9
1/2X	Top	1.09	361	331.2	.0469	8.01	56.2
	Middle	1.21	445	367.8	.0743	8.05	67.0
1X	Top	.723	164	226.8	.0347	6.21	58.6
	Middle	.709	29	351	.0150	4.60	52.1
2X	Top	.947	70	73.9	.00988	7.28	36.7
	Middle	1.00	111	111	.00146	4.45	18.0
4X	Top	.974	48	49.3	.00899	8.70	55.1
	Middle	.982	38	38.7	.00027	3.85	10.4

*Top indicates 0-1.5 mm from surface. Middle indicates 6.5-8 mm from surface.
** Lack of fusion porosity not included in Volume Scanned.
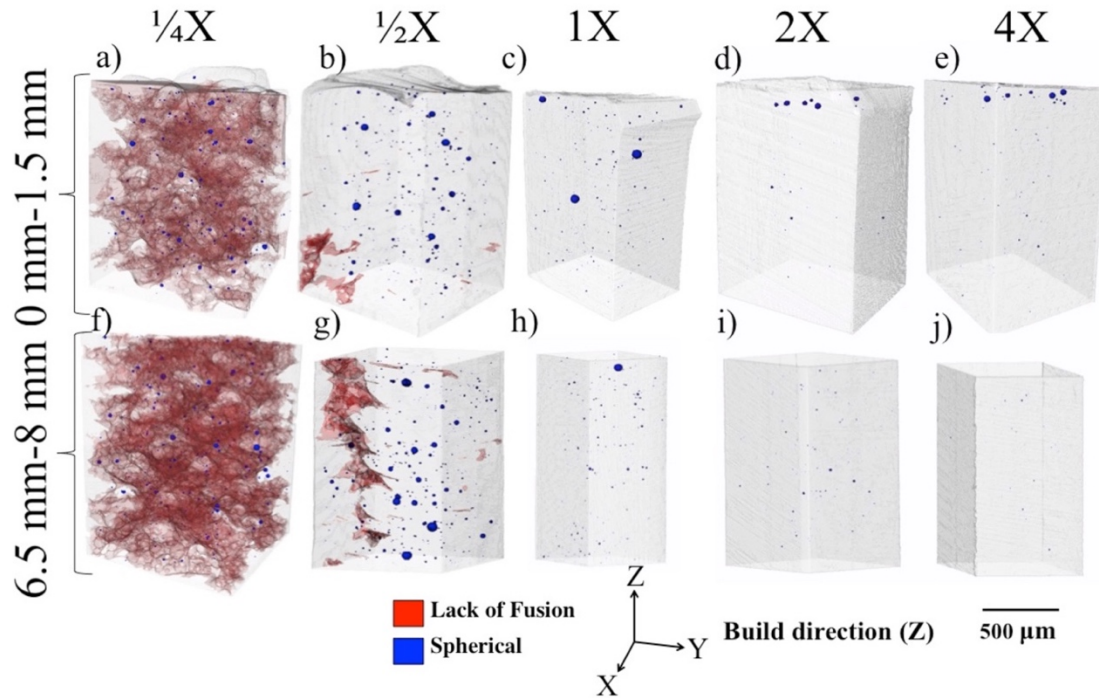
Figure 4.5: Synchrotron XCT results with lack of fusion highlighted in red and spherical porosity in blue. a) through e) represent the top 1.4 mm region, while f) through j) correspond to the 6-8.5 mm region. Significant variation in porosity is observed across the range of parameters. [4].
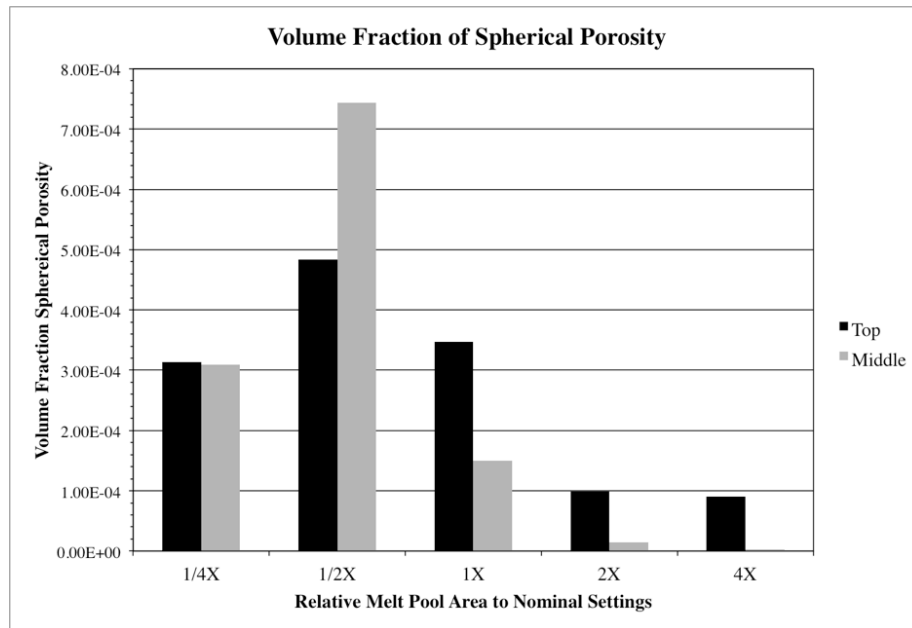
Figure 4.6: Volume fraction of gas porosity measured via μSXCT.
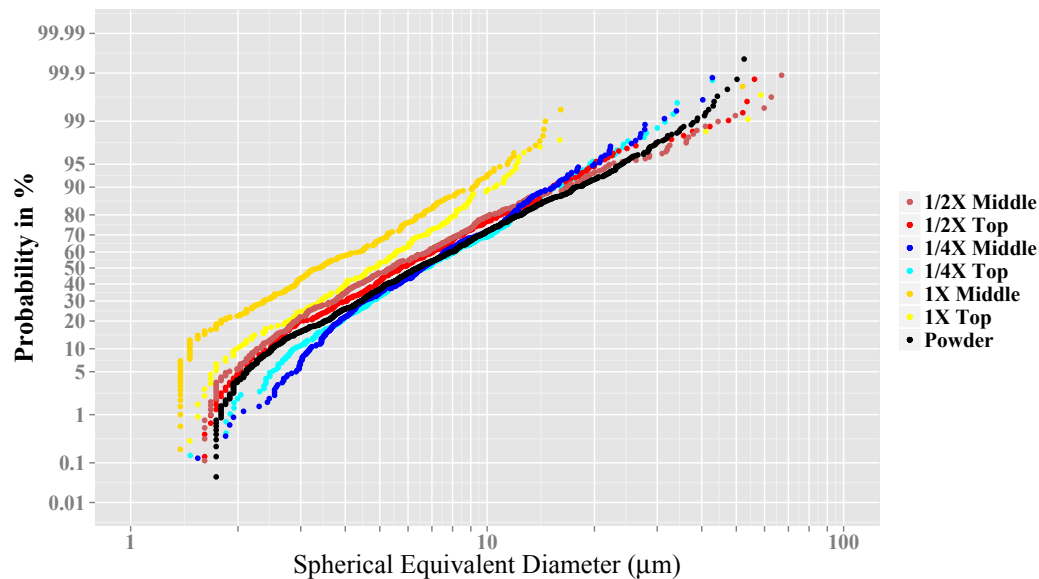
Figure 4.7: Comparison of size distribution of pores in powder and as-built samples. Size distributions of pores in the powder and the samples converge as melt pool size decreases. The substantial straight portions of most of the distributions indicate that the pores are approximately log-normally distributed.

Additionally, at the reduced melt pool size samples, lack of fusion is observed to increase

significantly. While the defects were too large to adequately capture in the scan volume, cross

sections (Fig. 4.6) show pore volume fractions of ~4 and 20% for the 1/2X and 1/4X samples respectively. Particularly for the 1/2X sample, the defects are separated by much more than the 200 μm hatch spacing, indicating they are not likely formed by the simple geometric considerations of the previously described lack of fusion model, but rather something like "channel pores" described in other reports [84], [85].
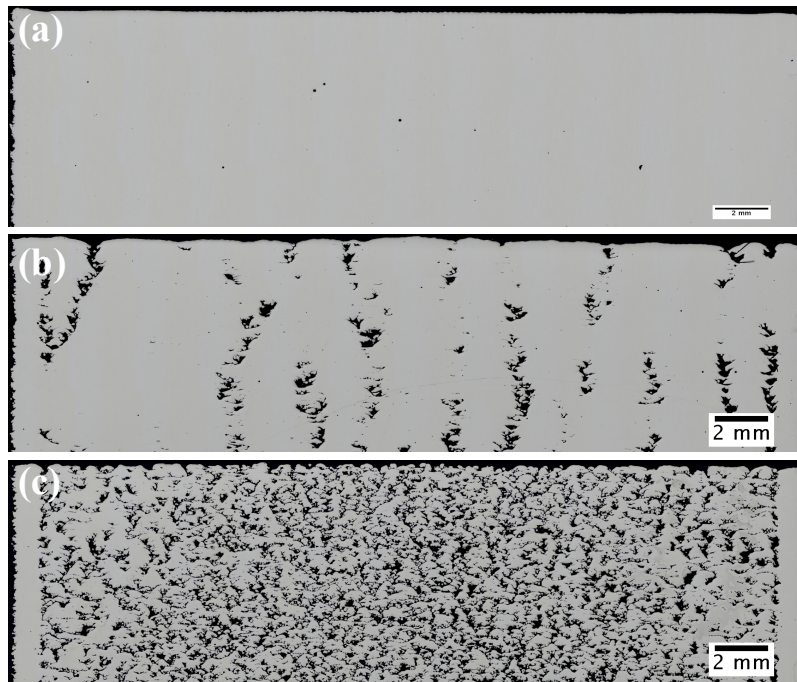
Figure 4.8: Light optical micrographs of polished cross sections of the (a) 1X, (b) 1/2X and (c) 1/4X samples. Large, vertically aligned lack of fusion flaws are present in the 1/2X sample, as was indicated by the CT. The lack of fusion porosity is roughly 4 % by area in (b) and 20 % in (c).

4.3 Discussion of μSXCT Analysis

The correlation between powder and part porosity observed in Figs. 4.2 and 4.3 provides strong evidence to support the theory that the porosity within the powder contributes heavily to the defect population in as-built EBM parts. Comparison of the gas pores in the AP&C powder with the as-built part (Fig. 4.3) shows a similar size distribution but lower number density and volume fraction,

consistent with previous results and the current assumption that some pores are eliminated during processing, either through combination in the melt pool and/or escape [3]. While the limited number of pores detected in the PREP powder and parts make it difficult to conclude that transfer is occurring from the powder to the parts, the size is comparable, and the presence of spherical pores in the as-built PREP samples suggest that some level of gas porosity does exist in the powder, albeit at a significantly reduced size and number density compared to the plasma atomized powder. While this does not conclusively prove trapped inert gas in the powder is the source of the defects in these as-built parts, there is sufficient evidence to largely disqualify the other two likely defect formation mechanisms, namely keyholing and absorbed gas porosity. The dramatic difference in porosity between the two as-built specimens despite their same processing parameters suggests that keyholing is not a factor, as a similar effect would be expected in both. Gong *et al.* speculated that the control software present in Arcam systems, which acts to stabilize the melt pool geometry, make it difficult to achieve the conditions required for keyholing [2]. Similarly, the gas analysis of the powder (Table 4.1) shows that with the exception of nitrogen, the TIMET powder had higher concentrations of absorbed gas, including hydrogen [24]–[26], making it unlikely that absorbed gases were the cause of the increased gas porosity seen in the AP&C sample. As will be discussed in Chapter 8, the fact that these pores are not completely eliminated during the HIP process, and their subsequent regrowth, provides further evidence that pores observed in the as-built state are a result of inert gas transferred from the powder. While keyholing or absorbed gas should not be discounted as possible defect formation mechanisms in the EBM process, in this case the inert gas porosity appears to be the dominant factor.

However, while significant evidence supports the idea that the powder is the source of porosity, the mechanism of its transfer from the powder to the part during processing is still

unclear. Fig. 4.5 shows that this type of porosity is significantly affected by processing conditions. Increasing the size of the melt pool by lowering the *speed function* effectively eliminated any large pores from the bulk of the material, with the exception of the very top of the build. Conversely, decreasing the size of the melt pool by increasing beam velocity resulting in a distribution closer to that of the porosity measured in the powder from Fig. 4.3. While this was not the same batch of powder used to build the samples in Fig. 4.5, they were both Arcam-supplied plasma atomized powder from AP&C, so it can be assumed they have reasonably similar pore distributions. It has been suggested that the elimination of pores with increased melt pool size is because of the increased amount of remelting of previous layers, giving pores more of a chance to escape the surface [3]. The final layers of the part would not have a chance to be remelted, therefore the porosity would remain, as seen in the 2X and 4X sample in Fig. 4.5. However, this seems to be contrary to the theory that the melt pool flow will drive porosity to the bottom of the pool, effectively trapping the porosity in the sample, possibly indicating a different mechanism for pore transfer is responsible.

While outside the scope of this research, another notable result is that the builds made with AP&C powder display a significantly higher number density of lack of fusion pores. This is a counterintuitive result because the expectation is that, given a similar size range for the two powders combined with the identical processing parameters and machine, a similar degree of melting should occur. This then suggests that other powder properties such as variations in the size distribution, associated packing density and spreadability may also significantly affect the frequency of lack of fusion defects. However, single bead experiments to capture melt pool cross sections were not collected for these parameters, and the proprietary control software of the Arcam process make it difficult to accurately extract process parameters for modeling purposes.

4.3 In-situ observation of Powder Pore Transfer

While the μSXCT studies provided considerable circumstantial evidence that the gas pores inside the powder were transferring to the as-built parts, the mechanism of their transfer, and potential removal through remelting, is still not conclusively understood. However, DXR is uniquely suited to observe this type of dynamic process. In this investigation, a sample of the AP&C powder shown in Fig. 4.2 was melted in an attempt to observe pore transfer from the powder to the melt. In Figs. 4.9 and 4.10, the powder was melted under stationary laser illumination with beam parameters P = 312 W, $2w_o$ = 140 μm for an exposure time of 1 ms. In both cases, pores contained in a powder particle adjacent to the beam location are pulled into the melt pool, and the pores are observed to transfer to the melt pool. However, in Fig. 4.9 (video S4.1), the pore is ejected almost instantly, while it remains in the melt pool in Fig. 4.10 (video S4.1). The main difference is the time at which the laser turns off in relation to when the powder is pulled into the melt pool. In Fig. 4.9, the laser is still on when the pore enters the melt pool. The pore expands and makes contact with the liquid/gas interface of the vapor depression, quickly escaping the melt pool. In contrast, the powder particle containing the pore in Fig. 4.10 enters the melt pool as the laser is turned off, and as such shows little disturbance in the melt pool. While it does display some movement, the surface of the melt pool appears to solidify prior to its possibility of escape. This was difficult to capture, as anytime a pore entered the melt pool while the laser was on, it was rapidly ejected.

This behavior suggests pores within powders directly under the heat source would not contribute the final porosity in the as-built parts, which further complicates the question of transfer mechanism. However, simulations by Khairallah *et al.* predicted that powder would be pulled laterally into the melt pool after the beam had passed, forming what they called a "denudation

zone" [58]. This behavior presents the conditions that the results seen in Figs. 4.9 & 4.10 suggest are required for pore transfer.

This theory was tested using a moving beam (P = 260 W, 700 mm/s) with a spot size of approximately 250 μm. Note that we needed to use a larger beam than we had measured in Appendix B in order to melt the large particles, but the spot size is not critical to this observation. Fig. 4.11 (video S4.2) shows a pore-containing powder particle entering the melt pool well after the laser has past that region but being pulled in from the denuded zone. The pore enters the melt pool and displays some forward motion in the same direction as the beam travel speed, but otherwise stays in the melt pool while it solidifies.
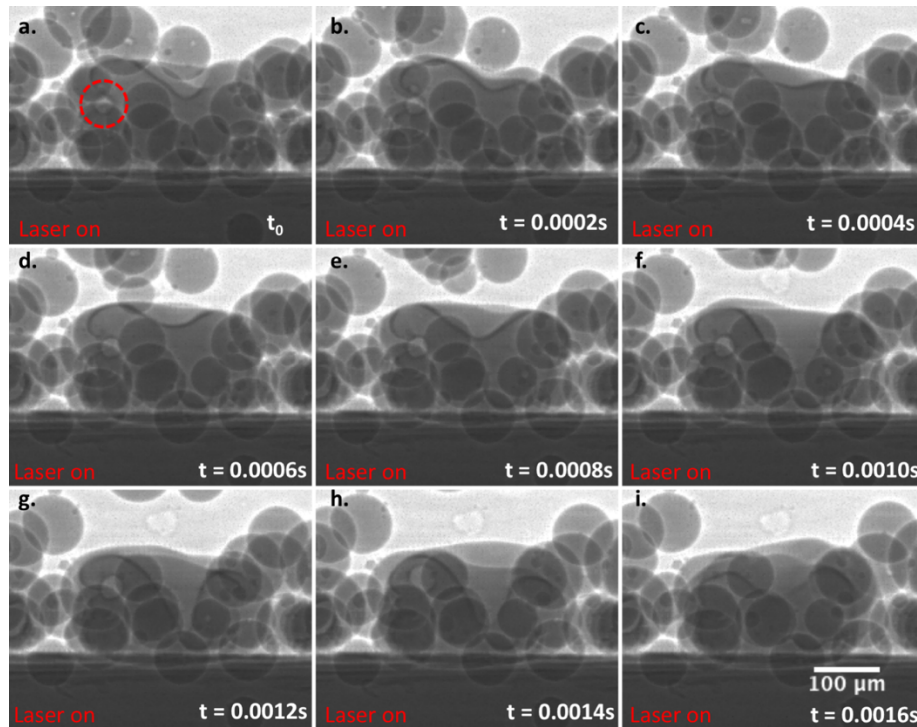
Figure 4.9: DXR time sequence showing transfer of a gas pore from a powder particle to the melt pool, and its subsequent rapid escape from the melt pool. Laser is on during the whole sequence.
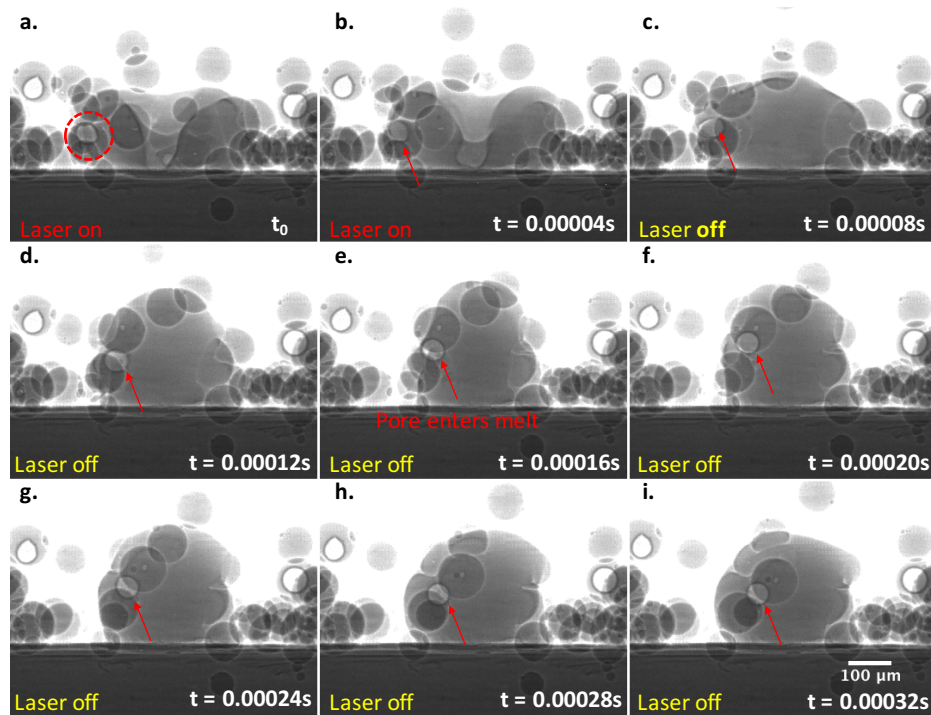
Figure 4.10: Time sequence showing transfer of pore to from a powder particle to the melt pool, and the pore remaining in melt pool. Laser is on turned off right as the powder particle enters the melt pool.
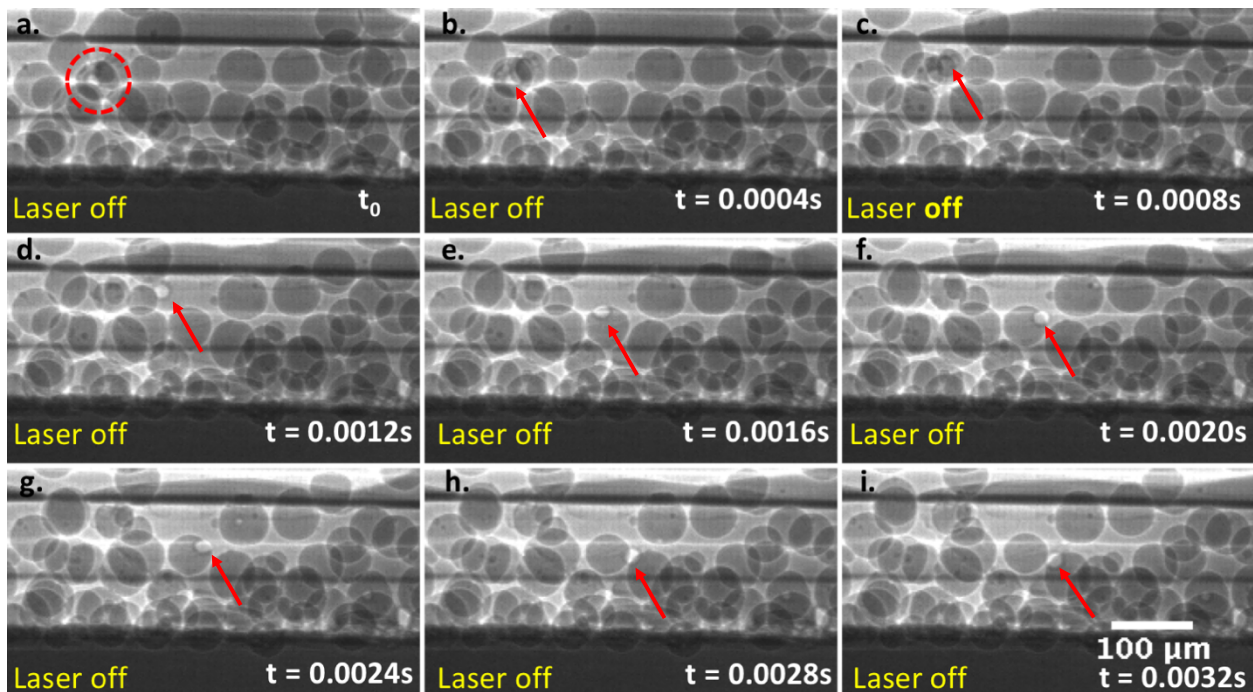
Figure 4.11: Time sequence showing transfer of pore to from a powder particle to the melt pool, and the pore remaining in melt pool. Laser has moved far past the field of view when the particle enters the melt pool.

While this provides a clear demonstration that this mechanism is possible, there are still questions remaining about how this mechanism behaves in vacuum environment and with sintered powder, as is the case with the EBM process discussed in this chapter. We attempted to observe this mechanism in these conditions but were unsuccessful due to the tendency for the powder to violently eject from the incident area of the laser when under vacuum conditions, even at relatively low powers. Furthermore, sintering the sample in suitably inert environment proved impossible with the available equipment. However, despite the lack of direct observation, it still seems feasible that despite the sintering pass, the powder could still be laterally pulled in once it makes contact with the melt pool, as the sintering is very minor and designed to not damage the powder particles for future recycling by forming significant necks or agglomerates [86]. It is also possible that simply melting on the periphery of the melt pool would be enough to entrain the gas, provided it does not come in contact with the vapor depression.

4.4 In-situ observation of Pore Removal Through Remelting

While directly observing the transfer of the pore under sintered and vacuum conditions was unsuccessful, testing the theory of remelting under vacuum conditions was relatively simple. A sample of Arcam Ti-6Al-4V built under nominal processing conditions was machined into the size of a DXR coupon. A moving beam experiment using beam conditions of P= 260 W, V = 0.4 m/s, and laser spot size $2w_o$ = 95 µm was performed under vacuum conditions. Figure 4.12 shows a time series of a keyhole depression formed by the laser moving through a preexisting pore in the material. It is clear that in Fig. 4.12e, the two begin to interact, and once the depression moves past, the pore is completely remove. It is impossible to know from the 2D projection if the pore
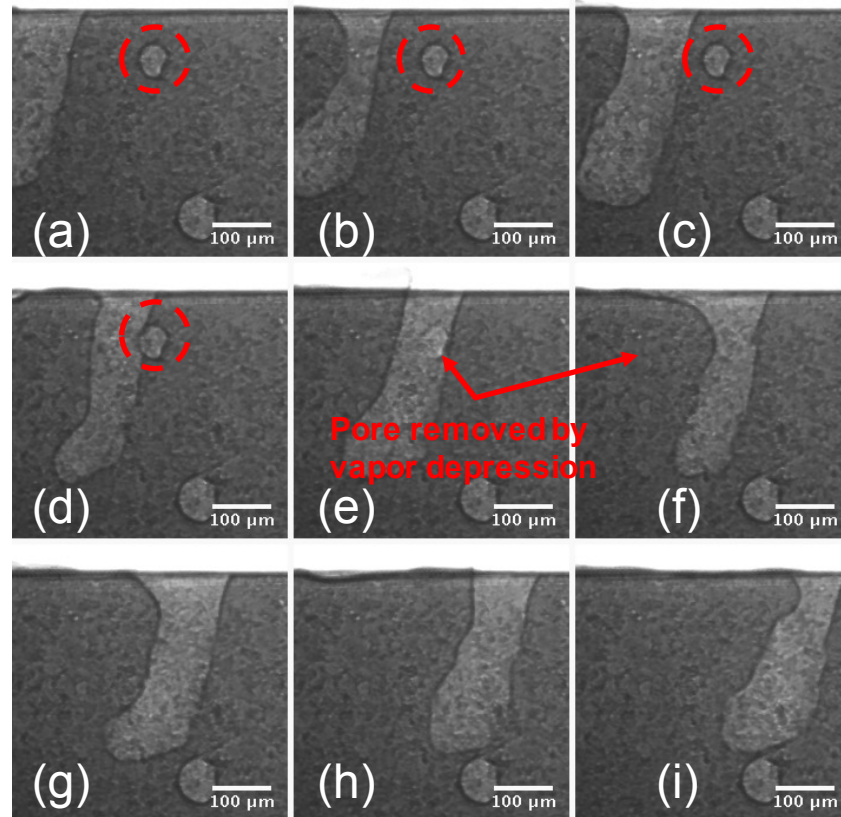
Figure 4.12: DXR recording of vapor cavity removing preexisting gas pore in Arcam EBM fabricated Ti-6Al-4V. As in Fig. 4.9, contact with the vapor depression enables elimination of pore from the melt.

Interacted with the melt pool or vapor depression, but regardless the observation further supports the theory from section 4.2 that the larger melt pools were the source of the reduced porosity evident in the 2X and 4X melt pool area samples, as they effectively cleaned up the underlying areas of defects, and only the non-remelted regions at the top still contained defects. This is not too farfetched, as the same rational is used to describe strategies to reduce porosity formation in electron beam welds of Ti-6Al-4V, where direct alignment of the keyhole on the surface containing the pore forming gas largely reduced porosity [26].

4.5 Conclusions

The findings from the study of the powder pore transfer during the metal powder bed AM process can be summarized as the following:

i. The size distribution of pores within the starting powder was observed to transfer over to the as-built part to a reasonably close approximation, but at a lower volume fraction. The fraction transferred is, however, dependent on processing parameters.

ii. In the Arcam process, process parameters that produced larger melt pool sizes, and therefore remelted more previously deposited material, were observed to contain significantly less porosity than those with smaller melt pools

iii. The direct observation of a pore transferring into the melt pool with a powder particle has been captured both for a static and moving been scenario. While only limited data was collected on this behavior, it suggests that this transfer occurs at regions adjacent to the melt track rather than direct in the beam path due to the tendency of the vapor depression to remove pores.

iv. Remelting is observed to be an effective way to remove porosity in-situ.

Chapter 5: X-Ray Computed Tomography of Porosity Evolution Across Process Space in Laser Powder Bed Fusion Ti-6Al-4V

Note: This chapter is reproduced from: Cunningham, et al. JOM (2017) [87]

This work builds upon a previous study conducted on an Arcam AB® Electron Beam Melting (EBM) machine, discussed in Chapter 4.2, where the effect of processing variables on porosity was measured using synchrotron-based μSXCT [4], as well as previous studies where defects were mapped out across process space using less informative techniques such as bulk density and cross sections [2]. In this study, a large region of process space for an EOS M290 LPBF machine was covered to observe the transition of the dominant porosity formation mechanism from lack of fusion to keyholing, as the primary variables - power, velocity and hatch spacing were varied to control the amount of overlap between adjacent melt pools, while simultaneously observing the effect of changing these variables independently. In general, the expected defect regime transitions occurred in their predicted locations, but gas pores and some small irregular defects persisted in most samples. Additionally, one sample suggested the possibility of keyhole porosity induced by a too-close hatch spacing.

5.1 Design of Parameters

Test cubes with side lengths of 1.5 cm were fabricated on an EOS M290 courtesy of Dr. Colt Montgomery using EOS Titanium Ti64 (Ti-6Al-4V alloy) powder. These tests were designed based on the trends in porosity observed in the previous work with EBM Ti-6Al-4V [4]. The goal of this study was to observe variations in porosity across available process space at varying beam powers, velocities and hatch spacings in a controlled manner utilizing the process mapping

approach [8]. The process parameters were designed in collaboration with Drs. Sneha Narra, and

Jack Beuth of Carnegie Mellon University. Table 5.1 summarizes the process parameters used to

fabricate the test samples, along with the estimated melt pool widths based on measurements from

single-bead-on-plate tests performed by our collaborators, and the "overlap depth" between two

adjacent melt pools for the purpose of predicting lack of fusion porosity. The "overlap depth", d_O,

is defined as the maximum depth of the overlapping region between two semi-circular melt pools

for a given hatch spacing. This geometric model assumes that lack of fusion will be eliminated if

the layer thickness, t_l, is less than the "overlap depth", d_O [88] (i.e. $t_l/d_O < 1$). In this model, a semi-

circular melt pool shape was assumed, and 30 μm layer thickness, t, was used. It should be noted

that melt pools are often observed to be unstable, particularly when they are small [89]. This can

result in variation in melt pool widths and depths that are critical for sufficient overlap between

adjacent tracks and fusion with previous layers. Such melt pool variation was not taken into

account in these tests but was expected to contribute to defect population. In particular, cases with

ratios of hatch spacing to melt pool width (H/W) approaching unity (e.g. sample 12 and the default

case of sample 1) are sensitive to variations in melt pool width that can lead to lack of fusion

porosity, as there is insufficient additional overlap to account for such fluctuations. Additionally,

samples were included to purposefully initiate keyholing or lack of fusion porosity. Finally, in

order to investigate the contribution of porosity from the trapped argon gas in the powder, a sample

of the powder from the machine was also scanned, and the size distribution of the spherical

porosity contained in the powder was compared to pores with similar morphology in the as-built

parts.

To summarize, sample 1 was built with default parameters recommended for Ti-6Al-4V

by the machine manufacturer (EOS). Samples 2 – 5 were built at a default power of 280 W and

varying velocities, with hatch spacing adjusted to attempt to avoid any lack of fusion defects based on the geometric model assumption. Within this group, sample 2 was designed to contain keyhole porosity based on observations of single-bead-on-plate results. Also within this group, samples 4 and 5 were designed with an H/W value near 0.71, which yields the maximum deposition rate under the assumptions of a semi-circular melt pool shape and the ability to freely adjust layer thickness with overlap depth, d. Similarly, at the default velocity of 1200 mm/s, beam power was varied in samples 6 – 8, with hatch spacing again adjusted to prevent lack of fusion porosity. The intent was to be able to compare samples across process space without numerous variables changing between each sample, thus making trends more easily observed, while simultaneously observing the effect of overlap depth. Samples 9 and 10 were designed to purposefully form lack of fusion porosity (note the t_l/d_O values >1). Sample 11 was designed to test the effect of decreasing hatch spacing to double the effective overlap depth compared to default conditions. Finally, sample 12 was included with parameter values aimed at maximizing deposition rate while avoiding keyholing or lack of fusion porosity based on the current assumptions. It should be noted that the final ~100 μm of deposited layers for each sample automatically switched to "top skin" processing parameters, which are listed in Table 5.1.

μSXCT samples with dimensions of 1 mm x 1 mm x 15 mm were sectioned from the center of the test cubes, with the long dimension parallel to the build direction. The samples did not undergo any post processing common to AM processes such as hot isostatic pressing (HIP), and are therefore shown in their as-built state. Synchrotron x-ray microtomography was performed at the 2-BM beamline at the Advanced Photon Source at Argonne National Lab operating in white beam mode. A total of 1,500 projections were taken over 180˚ with a 50 ms exposure time resulting in an approximately 2 minute scan time per 1.5 mm^3 volume. A 0.65 μm voxel size (edge length)

was obtained, resulting in a minimum resolvable feature dimension of approximately 1.5 µm. The

volumes were reconstructed from the radiographs using TomoPy 0.0.3 [73]. Avizo 9 software was

used for segmentation and analysis (Appendix A).

Table 5.1: List of parameters used in fabricating the test samples and associated melt pool dimensions

Sample No.	Power (W)	Velocity (mm/s)	Hatch Spacing, H (µm)	Melt Pool Width, W (µm)	Overlap depth, d_o (µm)	t_l/d_o	H/W	Goal of Test
Sample 1	280	1,200	140	160	39	0.77	0.88	Default
Sample 2	280	400	140	293	128	0.23	0.48	Velocity effect with keyholing
Sample 3	280	800	140	233	93	0.32	0.60	Velocity effect
Sample 4	280	1,000	140	199	70	0.43	0.70	Velocity effect
Sample 5	280	1,500	80	115	41	0.73	0.70	Velocity effect
Sample 6	370	1,200	140	196	69	0.43	0.71	Power effect
Sample 7	325	1,200	140	178	55	0.55	0.79	Power effect
Sample 8	100	1,200	50	89	37	0.81	0.56	Power effect
Sample 9	165	1,200	140	115	0	N/A	1.2	Lack of fusion
Sample 10	280	1,200	160	160	6	5	1	Lack of fusion
Sample 11	280	1,200	40	160	78	0.38	0.25	2x default overlap depth
Sample 12	370	1,000	240	252	38	0.79	0.95	Maximum deposition rate
"top skin"	280	1,200	140	160	39	0.77	0.88	
*in all cases, layer thickness, t = 30 µm								

5.2 Results & Discussion

Projections of the three dimensional (3D) tomographic reconstructions of the top 1.5 mm of each

sample, ordered by melt pool overlap depth (see Table 5.1), are given in Fig. 5.1. It should be

noted that viewing porosity in 3D projections creates an exaggerated appearance of the volume

fraction of pores within the sample. Pores were segmented and colored by morphology, with the

exception of Fig. 5.1-2, which was colored by individual pore due to its significantly larger defect

population. While morphology is not a conclusive metric for determining the defect formation

mechanism, it is reasonable to assume that pores that are highly spherical are likely to be formed

from insoluble gas bubbles trapped during solidification, while largely irregular pores are likely

lack of fusion defects. For this experiment, an anisotropy value of 0.5 was used as the maximum

cutoff for "spherical" pores.

A summary of the pore statistics is given in Table 5.2. It is readily observable from these

results that irregular pores are the dominant defect observed in these samples. However, sample 2

shown in Fig. 5.1-2, which was fabricated to guarantee keyhole porosity, illustrates the challenges

of segmenting by morphology when keyholing can be a factor, as pores range from nearly spherical

to largely irregular. Considering this fact, the samples were analyzed by pore morphology, while

also taking into account results and trends from related samples that only differ by one process

variable (e.g., different power but same velocity and hatch spacing), as well as the general location

in process space.

Looking first at lack of fusion (highly irregular, larger pores), it is apparent from Fig. 1 that

lack of fusion scales roughly with melt pool overlap depth, with some notable exceptions. Figs.

5.1-8 & 5.1-9 show that these two samples are dominated by lack of fusion. Of these two, only

sample 9 was designed to have considerable lack of fusion, with sample 8 theoretically fully melted

based on the assumptions used in the design of the sample parameters. However, sample 8 has the

smallest melt pool width, and it is possible that the semi-circular assumption breaks down at such

low-melting conditions. Figs. 5.1-12 & 5.1-10 show that samples 12 and 10 also have significant

lack of fusion. This is expected, as these samples have a value of H/W near 1, so minor variations

in melt pool width can yield lack of fusion porosity. Samples 4, 6, 7 and 1 (Figs. 5.1-4, 6, 7, 1)

also contain at least some lack of fusion pores despite having been designed to be fully melted,

though significantly less than samples 8, 9, 10 and 12.
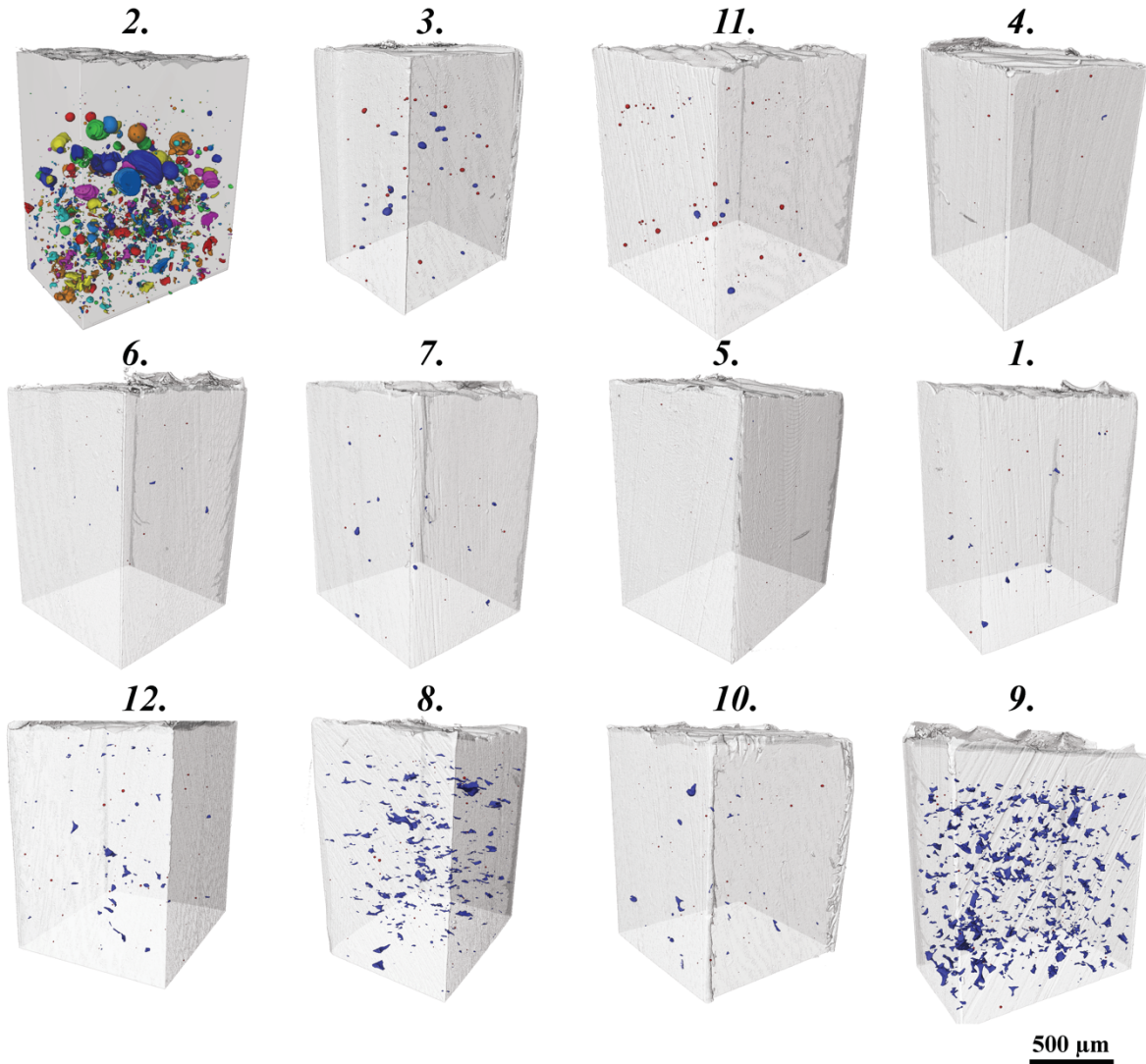
Fig. 5.1: Projections of μSXCT-reconstructions of samples in order of decreasing overlap depth, with associated sample numbers from Table 5.1. The sudden shift in porosity observed over the top ~100 μm is due to an automatic shift in parameters to "top skin" that are different from those used in the bulk. Pores meeting the "spherical" morphology are colored red, with the remainder colored blue, except in *2,* where pores were given unique colors to more clearly identify individual defects. Scale bar is approximate due to perspective view of the projections [87]**.**

In these cases, it is also likely that fluctuations in the melt pool size caused these defects, as they are relatively infrequent and appear to occur randomly and decrease in frequency and size at larger overlap depths. These results suggest that while the general trend for predicting lack of fusion porosity as a function of overlap depth is sound, the assumption of constant melt pool sizes and semi-circular melt pool shapes does not accurately represent what is occurring during the builds.

Keyholing was attributed as the second leading cause of defects observed in these samples. As previously discussed, it is difficult to conclusively identify keyhole porosity by morphology but looking at where the sample lies in process space, and identifying trends with samples fabricated with similar processing conditions, can give a good indication when keyholing conditions are active. This transition will be investigated further in Chapter 7. Samples 2 and 3 (Fig. 5.1-2, 3) are clearly cases of keyholing, as there are large pores that do not resemble lack of fusion. This is to be expected, as these samples are fabricated at high power, low velocity conditions, which is the area of process space having large melt pool sizes where keyholing is frequently observed [2]. Sample 11 (Fig. 5.1-11), despite its small melt pool size not generally associated with keyholing, is also believed to contain primarily keyhole pores, and is therefore an outlier. While the pores have a similar size distribution to the pores contained in the powder (Fig. 5.2.a, b), the sudden onset of these pores compared to samples 1 and 10 (Fig. 5.1-1, 10), which differ only in hatch spacing, suggests that their cause is keyholing induced by overheating due to the significantly reduced hatch spacing: given what was discussed in Chapter 4, it is unreasonable that there would be a sudden increase in trapped gas porosity with increased overlap between melt pools.

The remaining porosity formation mechanism often attributed to defects in laser power-bed AM materials is trapped gas porosity, as discussed in Chapter 4, where inert gas pores trapped within the powder was shown to transfer to the part during fabrication [4][3]. In general for Ti-6Al-4V, other trace gases such as oxygen are not likely to precipitate gas pores due to their high solubility in titanium [3]. Fig. 5.2a shows a μSXCT-scan of the powder used to fabricate the samples in this experiment, with interior porosity shown in red. A comparison of the volume normalized size distribution of spherical pores measured in the powder and the samples where gas

porosity was observed is given in Fig. 5.2.b. Samples 2, 3, and 11 were omitted from this comparison, as these defects were considered to be from keyholing, as previously discussed. Comparing the volume averaged size distributions shows that gas pores within the parts have roughly the same size distribution, but at lower volume fraction, reflecting what was observed in Chapter 4. As with the previous study in the EBM process, the presence of gas porosity is observed to vary with processing parameters. Samples containing low amounts of remelting by adjacent melt pools and/or remelting of previous layers (high t_l/d_O or H/W) and consequently large amounts of lack of fusion porosity, such as samples 9, 10 and 12, also contain larger populations of trapped gas pores [4]. Sample 8, which contained an unexpectedly large amount of lack of fusion porosity, also contained a higher concentration of gas pores, further supporting that it had a smaller melt pool size than was predicted. It should be noted that, unlike the electron beam melting systems that operate in vacuum, laser powder-bed AM processes run in a gas (argon for Ti-6Al-4V) atmosphere, so in addition to the transference of trapped argon gas in the powders, there is also the possibility of atmospheric gas being trapped during the melting process. Additionally, any processing defects such as lack of fusion or keyholing will also likely contain gas, so if subsequent melt pool passes remelt them, they may also reform to a spherical trapped gas pore. It is therefore difficult to definitively conclude that the observed porosity in the parts are transferred from the powder particles, but the similar size distributions and previous observations from other powder bed systems would suggest this is the case.

Table 5.2: Pore statistics in order of decreasing overlap depth.

Sample No.	Spherical Pores		Irregular Pores	
	Vol. % Spherical Pores	Max. Eq. Diam. (μm)	Vol. % Irregular Pores	Max. Eq. Diam.(μm)
Sample 2	.67 %	133	1.69 %	162
Sample 3	.0092 %	32	.052 %	57
Sample 11	.0093 %	36	.005 %	36
Sample 4	.00073 %	14	.00023 %	14
Sample 6	.00019 %	9	.00010 %	21
Sample 7	.00041 %	12	.0050 %	33
Sample 5	.000096 %	8	.00013 %	14
Sample 1	.00077 %	11	.0056 %	31
Sample 12	.0015 %	19	.021 %	57
Sample 8	.0012 %	15	.11 %	66
Sample 10	.0010 %	16	.015 %	54
Sample 9	.0015 %	12	.34 %	62
Powder	.029 %	29	n/a	n/a
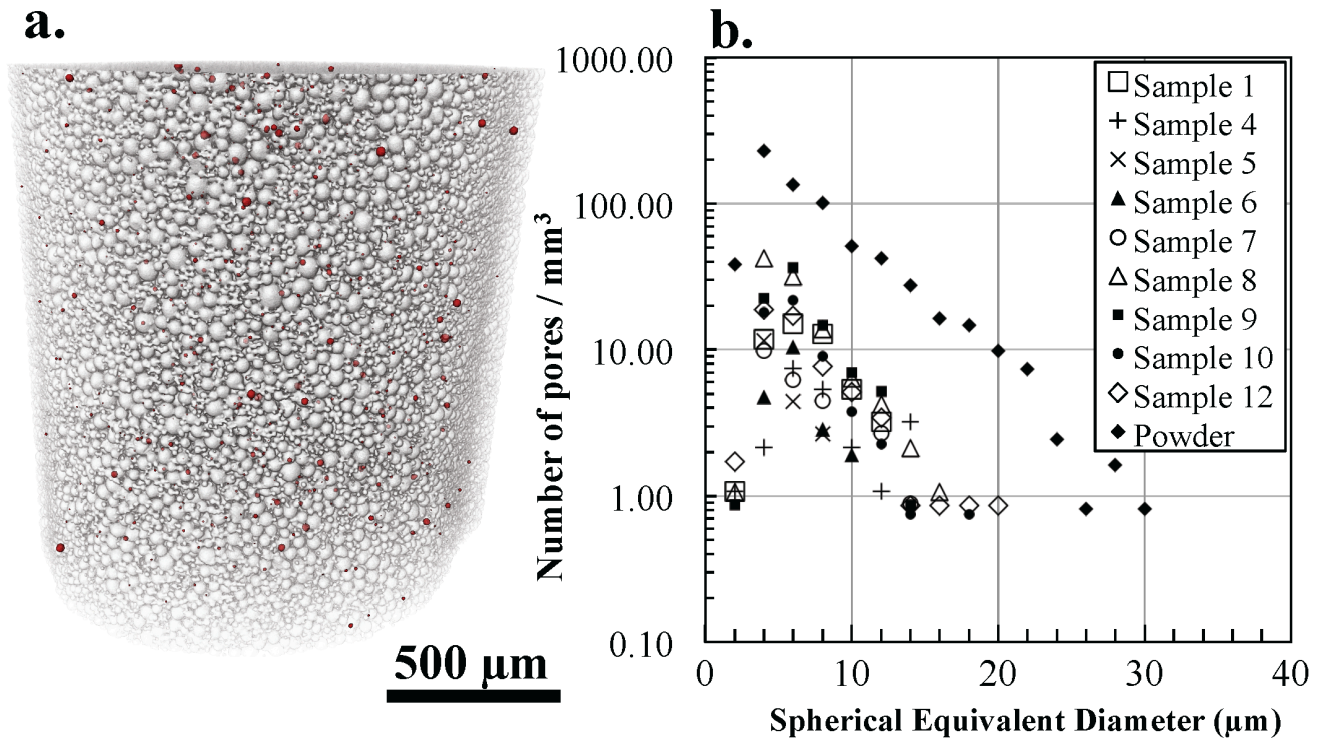
**Fig. 5.2: a. Projection of μSXCT reconstruction of Ti-6Al-4V powder with porosity trapped within powder particles shown in red. b. Volume averaged size distribution of spherical pores detected in the powder vs. samples identified as having gas pores. A comparison of the distributions suggests that smaller pores (< 15 μm) in the powder may transfer to the as-built parts, while larger pores do not.**

5.3 Conclusions

Synchrotron-based μSXCT was used to observe the variations in porosity as a function of processing parameters (power, velocity, and hatch spacing). Pore morphology, the location of the sample in process space, and trends observed from samples with similar processing conditions were used to infer the acting pore formation mechanisms for each sample. This experiment resulted in the following conclusions:

i.   The presence of lack of fusion porosity scaled with the overlap depth between adjacent melt pools based on a geometric model, except in conditions where the semi-circular melt pool assumptions is assumed to breaks down. Small, randomly dispersed lack of fusion pores were also observed where the model did not predict.

ii. More accurate measurements of the melt pool size and shape, taking into account variability due to melt pool fluctuations, will needed to further improve the geometric model for lack of fusion porosity.

iii. Processing-related flaws (lack of fusion, keyholing) were the dominant defects observed in the majority of examined samples. Gas porosity was not observed to be significant compared to the presence of processing flaws, by contrast with previous results from the EBM process, owing largely to the fact that the smaller powder size reduced the maximum size of the pores that can transfer to the powder.

iv. Gas porosity was observed to change with processing parameters, being more frequent in cases with low remelting conditions, in line with previous observations from the EBM process.

v.   The ratio of hatch spacing to melt pool width can be important. It appears (based on one case in this study) that too small of a ratio can induce keyholing porosity, even for power

and velocity values not sufficient to induce keyholing on their own. However, too large a ratio (approaching 1) can yield lack of fusion porosity due to fluctuations in melt pool dimensions, even in cases where the overlap depth would otherwise be sufficient.

vi.   Defect populations can be considerably reduced from those observed under default settings by using further optimized parameter values, such as those used to fabricate sample 5.

Chapter 6: Keyhole Transition in Laser Spot Welds

This chapter examines the formation of a vapor cavity and subsequent keyhole transition under stationary laser illumination. The prevailing opinion in metal AM is that the "keyholing" region is necessarily avoided due to the tendency to form defects, which pose a significant to the fatigue sensitive target markets of biomedical and aerospace. However, limited research has been performed on the conduction-to-keyhole transition in the welding community, and even less under processing conditions relevant to metal AM. Ultra-high speed synchrotron X-ray imaging is used to directly observe this transition in Ti-6Al-4V plate under stationary laser illumination at frame rates up to 400 kHz. Two separate transitions were identified, consisting of the formation of a vapor cavity, and the subsequent keyhole transition. The results presented in this chapter for stationary laser melting are used to predict the transitions for a scanning beam in Chapter 7.

6.1 In-situ X-Ray Observation of the Keyhole Transition in Laser Spot Welds

As discussed in Chapter 2, previous investigations into dynamic laser-metal interactions for a stationary laser have relied upon ex-situ analysis or visible light cameras [40]–[42]. High speed x-ray imaging has proven useful in examining this dynamic behavior, while also providing sub-surface information regarding the vapor depression and melt pool that is otherwise impossible to observe [90]. In the case of the DXR experimental setup described in Chapter 3, using a stationary laser beam enables the use of significantly higher frame rates (200-400 kHz) owing to the smaller field of view required to capture the behavior.

These experiments were performed on 400 μm thick Ti6Al4V coupons. Specifics of the experimental setup and sample dimensions are described in Chapter 3, section 3.2. The surface of each sample was polished with 320-grit sandpaper and cleaned with acetone prior to laser exposure

to remove any organic contamination or oxide film. Experiments were designed to cover a range of spot sizes and powers, which are described in Table 6.1.

Table 6.1: Laser parameters for spot weld experiments in Ti-6Al-4V

Spot Size (µm)	Power (W)	Power Density (MW/cm^2)
95	104	0.733
95	156	1.10
95	208	1.47
115	156	0.751
115	208	1.00
115	260	1.25
140	156	0.507
140	182	0.591
140	208	0.676
140	234	0.760
140	260	0.844
140	312	1.01
140	364	1.18

Figure 6.1 and video S6.1 show the formation and evolution of the melt pool and vapor depression over time under stationary laser illumination. Soon after the laser is turned on, the metal under the laser begins to melt, and a solid-liquid interface is visible in the radiographs as the boundary between the higher intensity transmitted through the (lower density) liquid and the lower intensity through the solid (Fig. 6.1a). Following melt pool formation, a vapor depression is formed at the center of the melt pool surface (Fig. 6.2b). The surface of the melt pool adjacent to the depression extends over the surface of the plate, indicating the depression displaces the liquid under the beam. The depression grows steadily in depth and width until it begins to fluctuate and,

shortly thereafter, transitions from a shallow, semicircular morphology to a deep, conical depression. When this transition occurs, the vapor depression rapidly penetrates through any remaining liquid between the depression and the solid/liquid interface of the melt pool (Fig. 6.1d-f). It should be noted that this is, to our knowledge, the first direct observation of this transition of the vapor depression, and for the purposes of the rest of this discussion will be referred to as the *keyhole transition*, which differs from previous definitions that generally identify the formation of the depression as the keyhole transition. Following this, both the vapor depression and melt pool penetrate at a faster rate into the material than in the previous regime, while exhibiting strong periodic fluctuations. To summarize, we have identified four distinct regimes of behavior; *melting, vapor depression formation and growth, vapor depression instability,* and finally *keyhole transition and growth*.
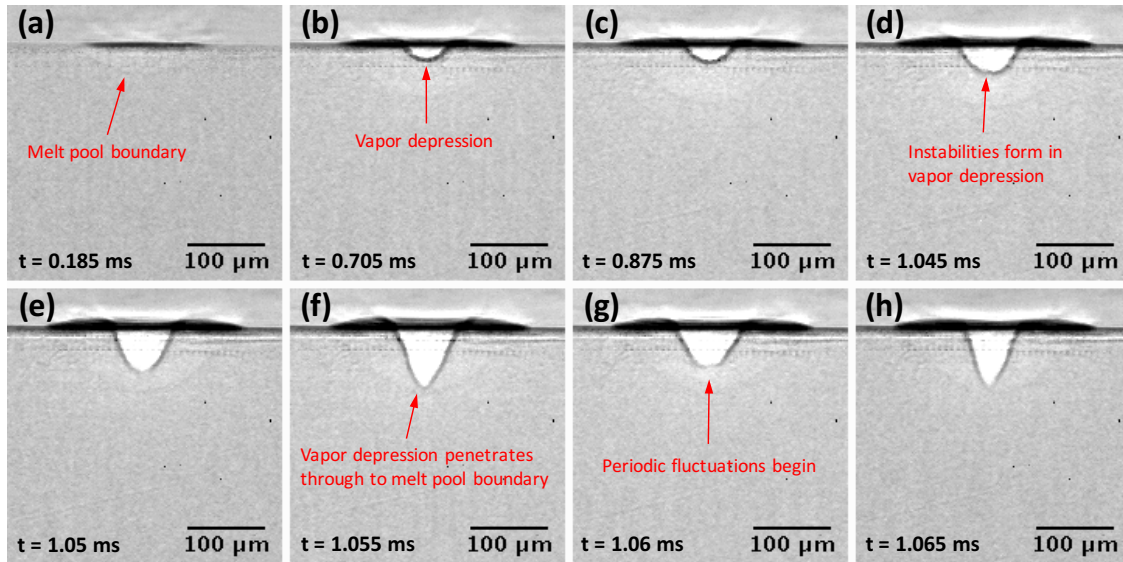

Figure 6.1: Radiographs illustrating the progression of the melt pool and vapor depression in Ti-6Al-4V formed under stationary laser illumination (100 μm spot size, P = 156 W). (a) Initial formation of the melt pool. (b) Formation of small, stable vapor depression. (c) Period of steady growth of the vapor depression. (d) Instabilities form in the vapor depression. (e-f) The vapor depression rapidly changes shape to a pointed conical morphology as it rapidly penetrates through the liquid layer to the melt pool boundary. (g-h) The vapor depression periodically fluctuates as it rapidly drills into the substrate.

To quantify the behavior of the vapor depression, the maximum depth was measured for each frame as a function of spot size and applied laser power. The results for the Ti-6Al-4V experiments are shown in Fig. 6.2. At relatively low powers, such those used in Figure 6.2a (156 W, $2w_o$ =140 µm) each stage outlined in Figure 6.1 (with the exception of the fluctuations prior to the keyhole transition) is easily identifiable, with melting beginning almost immediately upon the laser turning on, vapor depression formation at approximately 0.2 ms, and the keyholing transition occurring just after 1 ms.
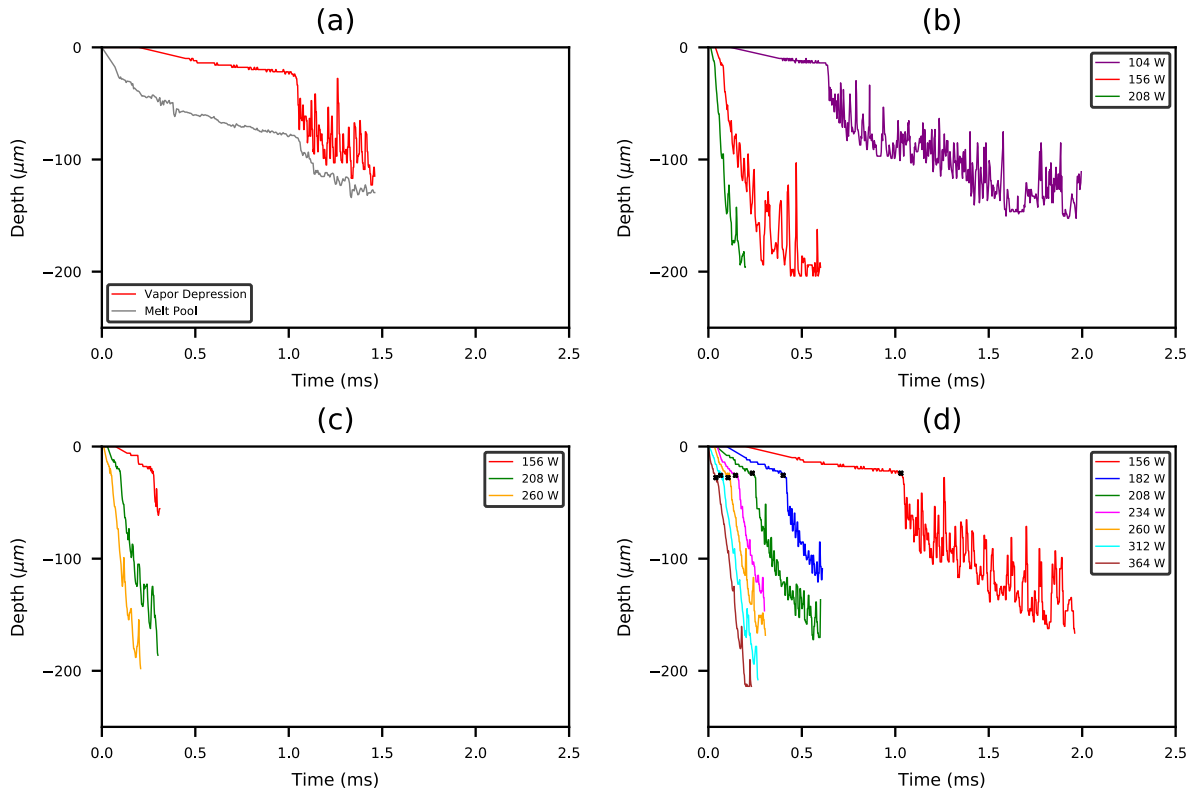

Figure 6.2: (a) Penetration depth of the vapor depression and melt pool over time under stationary laser illumination ($2w_o$ = 140 µm, 156W). (b, c, d) Penetration depth of vapor depression over time at different powers for a $2w_o$ = 95 µm, 115 µm, and 140 µm respectively.

As power and spot size change, two interesting behaviors regarding the aforementioned transitions in the vapor depression (formation, keyhole transition) were observed. First, the time-to-transition for both decreases non-linearly with increasing power for a given spot size. The

second is that the depth at which the transition occurs for a given spot size is nearly constant, occurring, on average, at 25 μm, 20 μm, and 13 μm for $2w_o$ = 140 μm, 115 μm, and 95 μm respectively. Figure 6.3 shows the last frame before noticeable instabilities form, just prior to the keyhole transition, for $2w_o$ = 140 μm. The time of each frame is depicted by a black 'X' on their respective curves in Figure 6.2d. Regardless of the applied power, the morphology of the vapor depression is very similar, in addition to the depth as previously noted. However, the size of the melt pool is significantly different, with the lower powers having a considerably larger melt pool at the keyhole transition. This explains the some of the difference in the keyhole transition behavior observed between the low and high power cases: the low powers display a sharp, cliff-like change in depth at the transition because of the rapid penetration through a considerable amount of liquid, whereas higher powers show a more gradual transition because there is less liquid under the vapor depression to push through before it makes contact with the melt pool boundary and begins to penetrate into the substrate in the post-keyhole transition regime.
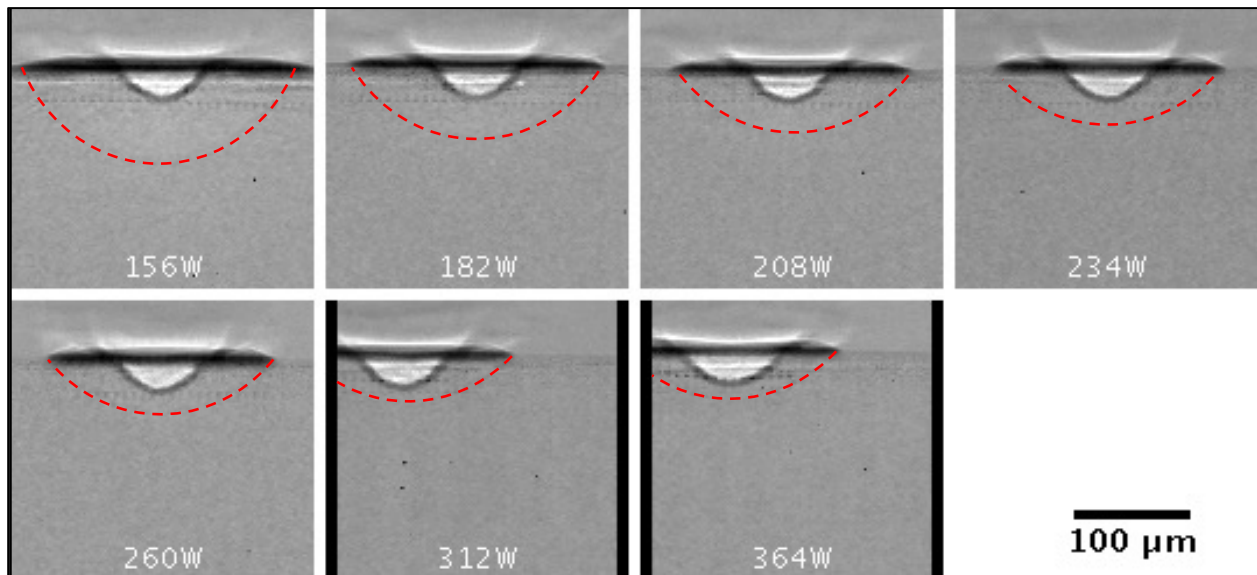

Figure 6.3: Melt pool and vapor depression prior to collapse and transition to keyhole regime for $2w_o$ = 140 μm. Times indicated by black 'X' on Fig. 6.2d. Melt pool boundaries outlined in red.

6.2 Analytical model for estimated transition times

As discussed in Chapter 2, the formation of a vapor depression is believed to be the point at which the vaporization induced recoil pressure above the melt pool is sufficiently large to overcome to surface tension of the liquid surface of the melt pool. To analyze the time dependence of the transitions observed in Fig. 6.2, a simple analytical thermal model commonly used in the spot welding literature was employed.

6.2.1 Force Balance

The important energy balance to consider is the recoil pressure, P_r, acting on the surface being irradiated by laser where vaporization is taking place, and the surface tension of the melt pool resisting the formation of additional liquid surface area in the depression. P_r is derived from the temperature-dependent saturation pressure calculated from the Clausius-Clapeyron relation

$$P_r = 0.56 P_{sat}(T) = 0.56 P_a \exp\left(\lambda \left(\frac{1}{T_b} - \frac{1}{T}\right)\right) \tag{6.1}$$

where $\lambda = \Delta H_V / k_B$, and T_b is the boiling temperature, and 0.56 is a constant to account for evaporation momentum loss [45]. The calculated recoil pressure up to the boiling point for Ti-6Al-4V using equation (6.1) and the materials properties shown in Table 6.2 is shown in Fig. 6.4., where a super-exponential growth is observed at temperatures exceeding ~2500 K. The most accurate way to calculate the force imparted by the vapor pressure on the melt pool surface would be to integrate P_r over the surface temperature profile in the melt pool being heated by the laser [40], [41], however, for this simplified model [28], the distribution is assumed to be uniform over the laser spot area, and equal to the peak temperature, which is discussed below.

As this pressure increases, a depression forms in the melt pool surface, as shown in Fig. 6.1. During the steady growth period of the depression, the width is observed to be roughly

constant, while gradually increasing in depth. Modeling this as a hemi-spheroid with radius a and depth c (c // z-axis), the surface area can be expressed for an oblate ($c/a < 1$) and prolate ($c/a > 1$) hemispheroid, respectively, as

$$S = \pi a^2 + \pi \frac{c^2}{2e} \ln\left(\frac{1+e}{1-e}\right) \tag{6.2}$$

$$S = \pi a^2 + \frac{\pi a c^2}{\sqrt{c^2 - a^2}} \sin^{-1}\left(\frac{\sqrt{c^2 - a^2}}{c}\right) \tag{6.3}$$

where e is the ellipticity equal to

$$e = \sqrt{1 - \frac{c^2}{a^2}}. \tag{6.4}$$

Assuming the radius a is fixed, the surface tension force changes with the growing depth c according to

$$F(S, \gamma) = \gamma \frac{dS}{dc} \tag{6.5}$$

where γ is the temperature dependent surface tension coefficient.
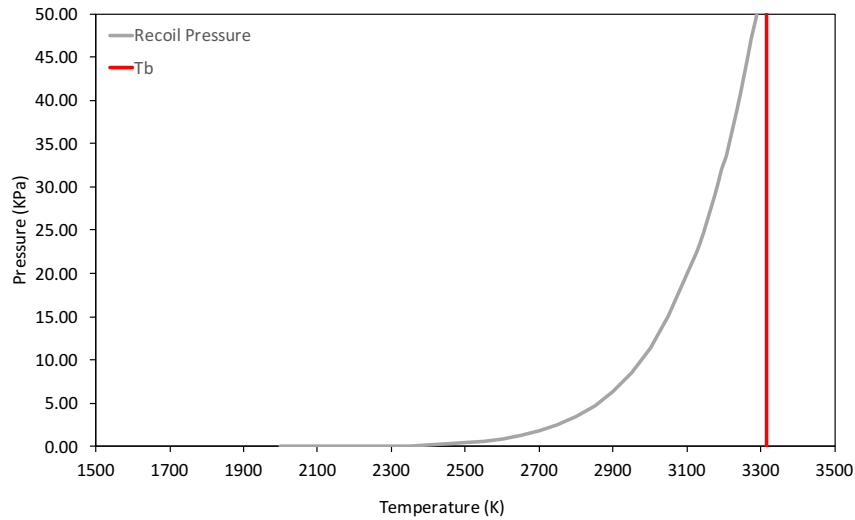
Figure 6.4: Recoil pressure as a function of temperature for temperatures calculated up to the boiling temperature for Ti-6Al-4V of 3315K. Note that 1 atmosphere is approximately 100 kPa.

An interesting consequence of this morphology is that the change in surface tension as a function of depth c (dS/dc) approaches a constant value of $\pi^2a/2$ at larger c/a ratios, which means that the surface tension force will approach a constant value or plateau. The result of this plateau behavior is that there exists a temperature above which the recoil force will exceed the surface tension force at all cavity depths. Figure 6.5 shows the calculated recoil force and surface tension force for the critical temperature T_c, where T_c is the temperature at which

$$\pi a^2 P_r = \gamma \frac{\pi^2 a}{2} \, .$$ (6.6)

 Figure 6.5 shows the calculated recoil force and surface tension as a function of temperature and cavity depth for the 140 µm laser spot size, where the depression radius during the steady growth period was observed to be ~40 µm. The temperature that satisfies equation (6.6) is only slightly below the boiling point of Ti-6Al-4V. This is consistent with the frequently cited assumption that the surface temperature needs to approach T_b to initiate keyholing [28], [44]. Figure 6.5 also shows that the approximate force balance resulting in the cavity depth just prior to the keyhole transition corresponds to a temperature very close to the critical temperature. This is because of the super-exponential relationship of recoil force with temperature near T_b, allied with the weak dependence of surface tension on temperature, so small changes in temperature (in the vicinity of the boiling point) can result in rapid changes in the equilibrium cavity depth.
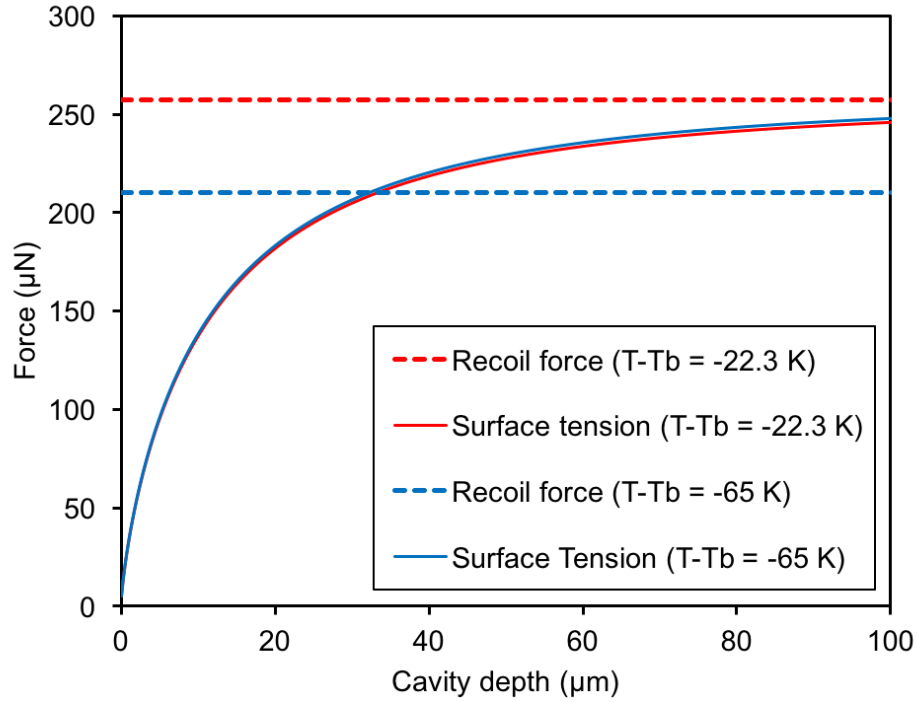
Figure 6.5: Surface tension force vs. recoil force at T_c and at the temperature corresponding to the depression depths observed in Fig. 6.3.

Table 6.2: Physical properties of Ti-6Al-4V

Physical Property	Ti-6Al-4V
T_b [91]	3042 ˚C
T_m [91]	1685 ˚C
ΔH_v [91]	421 kJ mol^{-1}
Surface tension coefficient [91]	-0.26 mN m^{-1}
Surface tension at T_m [91]	1650 mN m^{-1}
Absorptivity coefficient [38]	0.3
Thermal conductivity at T_b [92]	30 W m^{-1} K^{-1}
Density at T_b[92]	3780 kg m^{-3}
Specific heat at T_b [92]	730 J kg^{-1} K

6.2.2 Estimating Transition Times

The analysis above established a critical temperature T_c at which the surface tension and recoil

pressure forces acting on the melt pool become equal for a given spot diameter $2w_o$, which for

the following calculations was estimated to be T_b. In order to compare this to the measured

transition times, a one-dimensional heat flow model [45] was used to estimate the time t required

to reach T_c,

$$T_c = \frac{AI_L 2w_o}{k\sqrt{\pi}} tan^{-1} \frac{\sqrt{8Dt}}{2w_0} \tag{6.7}$$

where A is absorptivity, I_L is laser intensity (power density) calculated as $I = \frac{2P}{\pi(2w_o)^2}$, k is thermal

conductivity, D is thermal diffusivity, and $2w_o$ is laser spot size (diameter). Note that this version

of the equation is adopted from Trapp *et al.* which was modified from Bäuerle [45] to use the $1/e^2$

laser diameter [44]. Rearranging to solve for time t gives

$$t = \frac{(2w_0)^2}{8D} tan^2 \frac{\sqrt{\pi}\kappa T_c}{AI2w_0} \tag{6.8}$$

In order to compare the time-to-transition between the various spot sizes, the powers and

spot size were converted to power density. Note that this is an *applied* power density, as laser

absorptivity is ignored and assumed to be constant across each experiment since the material was

not varied. Figure 6.6 shows that the measured times for the vapor depression formation and

keyhole transition for each combination of power and spot size. Despite the simplicity of the

model, the calculated time to reach the critical temperature fits the behavior observed for the

measured time to initiate the keyhole transition, and roughly falls between the measured time for

vapor depression formation and keyhole transition. However, in all cases it under-predicts the time

required to initiate the keyhole transition. Using the same parameters, it is possible to fit the

calculated curves to the keyhole transition using a critical temperature of ~ 4700 K, but this seems

unreasonably high. Possible reasons for this discrepancy are discussed in the next section.
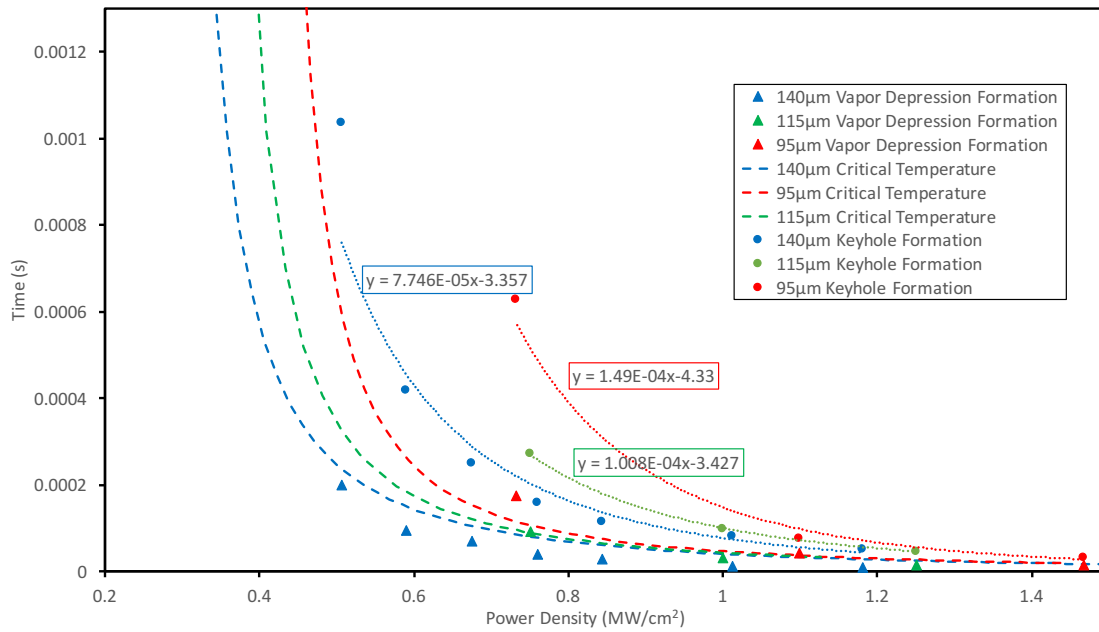
Figure 6.6: Measured time to reach vapor depression transition and keyhole transition as a function of power density compared to calculated time to reach critical temperature T_c from Fig. 6.4 using 1-dimensional heat flow model, Eq. (6.7).

6.3 Discussion

The established literature is in good agreement that keyhole formation begins when the surface temperature approaches the boiling point of the liquid metal, so it was not particularly surprising to see that even the simple model applied here agreed with the trends observed in the critical time required to initiate the depression. That said, it would be prudent to verify these results with a more accurate model if/when the capabilities become available. It should be noted that the experimental values in in Fig. 6.6 are largely dependent on spot size though the energy density, which was not measured to a high degree of accuracy in these experiments because of lack of access to a laser beam profiler.

However, this result is not as important as the distinction between the formation of the vapor depression and the keyhole transition. As discussed in Chapter 2, the formation of a

depression is often seen as the initiation of the keyhole regime, as there has not been a clear distinction between the formation of the vapor depression and the sudden keyhole transition observed here; the latter transition is of much greater interest for laser welding and for the avoidance of defects in AM. Given the speed at which these transitions occur, on the order of 10 µs, it is not surprising that it has not been observed without the application of ultra-high speed x-ray imaging. That said, the consequences of such a transition are evident, as has been reported in papers on pulsed laser drilling, some of which describe the delay in fast drilling rate observed here [93], [94]. However, the mechanism described for the delay between the formation of a vapor cavity and the region of rapid drilling is said to be the threshold for ejecting the liquid from the melt pool, which is a separate occurrence from the behavior seen here, where the depression morphology change appears to initiate the transition. This behavior does appear to occur in other materials systems. While a systematic study was only conducted for Ti-6Al-4V, this transition behavior was observed in a similar experiment for a 1000-series aluminum alloy, which will be discussed in the *Future Work* section. He et al. observed an increase in spatter out of the depression at a critical threshold depth for 304 stainless steel [41]. Hirano *et al.* also described what they called a keyhole transition but did not discuss their result in detail [42]. The potential connection between this interim drilling regime and the transition region between conduction and keyhole mode occasionally described for welding [47] is discussed in Chapter 7.

With regards to the under-predicted values for the keyhole transition time, it is important to consider what physical effects are not being taken into consideration in this simple thermal model. Cho *et al.* performed simulations investigating the depression behavior and fluid flow in the melt pool under the laser for titanium under laser irradiation near the keyhole transition [95]. This work highlighted the importance of taking evaporative cooling into consideration, which also

experiences super-exponential growth at temperatures similar to the recoil pressure. This causes the peak surface temperature to plateau for a period of time, over which complex fluctuations in fluid flow occur. This could explain the period of slow, steady growth observed in this study, where it is feasible that there is only slow change in peak temperature over this region, but eventually the critical temperature is reached and the rapid transition occurs. Note that the spot size was about 1 mm, which is much larger than that used here, i.e., ~100 μm and which is typical in LPBF.

Another point discussed in the paper, which is a well-established consequence of welding in the keyhole regime, is the increase in absorptivity caused by multiple reflections [53], [96]. As the depth of the depression increases, the number of internal reflections also increases, effectively increasing the power applied to the surface with the respective increase in temperature. Pointed geometries similar to those observed at the transition have been observed in laser drilling simulations taking into account the focusing effect of multiple reflections [97]. However, given the speed at which the transition occurs, as well as the shallowness of the depression, particularly for the small spot sizes, it seems unlikely that this would be the only cause rather than the previously described recoil pressure/surface tension balance. That said, it is highly likely that this factor plays a role in the significantly increased penetration rate once operating in the keyhole regime. Additionally, if any of this behavior is a result of multiple reflections, it is likely to behave differently on the other side of the focal plane where the rays are converging below the (initial) surface of the metal. Further simulations taking into account the temperature field in the depression, as well as ray tracing simulations may shed further light on this transition beyond the simple geometric model. Experiments to investigate the keyhole transition that place the focus below the metal surface are also indicated.

In addition to running higher fidelity simulations, there remain several interesting behaviors highlighted in the acquired videos that deserve further study, in particular the periodic nature of the fluctuations in the keyhole regime, as well as the decline of the "drill rate" as the keyhole approaches a maximum depth. It is likely that the latter has to do with the attenuation of the laser because of the significant plasma production within the keyhole [98], [99]. Additionally, there is considerable room for more experimental efforts investigating how this behavior changes across material systems, which is discussed in the *Future Work* section. However, as stated in the beginning of this chapter, spot welding experiments present simplified conditions for analyzing the laser/metal interaction, but of considerably more importance to AM is how the transitions observed here influence the behavior with a moving beam. This is the focus of the Chapter 7.

6.4 Conclusions

The findings from the study of the keyhole transition under static beam conditions are summarized as follows:

i.   In addition to the previously reported formation of a (shallow) vapor depression, a second, sharp transition was observed that directly led to a deep, keyhole depression.

ii. The trends in the formation of the vapor depression as a function of power density and laser spot size were predicted by balancing the recoil pressure and surface tension forces acting on the melt pool surface, coupled with a 1-dimensional heat flow model. The accuracy of this model could likely be improved by taking into consideration the effect of multiple reflections and evaporative cooling.

Chapter 7: Variations of the Vapor Depression Across Process Space

This chapter examines the formation and variation of the vapor cavity formed by a scanning laser in Ti-6Al-4V across process space. Understanding the boundaries of the "process window" for metal AM is of critical importance to repeatedly producing parts without defects. Ultra-high speed synchrotron X-ray imaging is used to directly observe and identify the conditions at which the transitions identified in Chapter 6 take place, and the subsequent morphological changes of the vapor depression as a function of processing parameters. Experiments were conducted on plate in order to more precisely measure interfaces and reduce experiment time. The results indicate that a significant vapor cavity exists for the majority of processing conditions relevant to metal AM, but that the traditional deep penetrating keyhole geometry is limited to the combination of high power, low velocity, which is commonly used in welding. Additionally, direct observations of multiple defect formation mechanisms related to the vapor depressions were made and discussed. Finally, a simple model to predict keyhole morphology was shown to accurately describe the changes in keyhole morphology as a function of processing parameters based off of the stationary beam experiments in Chapter 6.

7.1 In-situ X-Ray Analysis of Vapor Depression Formed by Scanning Laser

To investigate the evolution of the vapor depression under scanning beam conditions, "process maps" [8] were developed similar to those developed in Chapter 5, based on the two main process parameters for both laser welding and additive manufacturing, i.e., laser power and velocity. Parameters were chosen that cover the majority of the process space available to LBPF machines such as the EOS M290, on which this is experimental setup is based, with velocities ranging from

400 mm/s to 1200 mm/s, and powers ranging from ~100 W to ~500 W. As with the spot beam experiments described in Chapter 6, these were conducted on 400 μm thick Ti-6A-l4V coupons, with the exception of some of the high energy density conditions that used 800 μm thick coupons in order to avoid overheating effects. Specifics of the experimental setup and sample dimensions are described in Chapter 3.2. The surface of each sample was polished with 320-grit sandpaper and cleaned with acetone prior to laser exposure to remove any organic contamination or a significant oxide film. The specific laser parameters and coupon thickness for each experiment, with their respective quantitative analysis, are listed in Appendix C.

Figure 7.1 shows the process maps for two of the spot sizes used in the stationary beam experiments, 95 μm and 140 μm. Unlike the stationary beam experiments, which showed similar behavior over different time scales, the moving beam vapor depressions exhibit widely variable morphologies across process space. Additionally, unlike most descriptions of the keyhole boundary in process maps, it is clear that nearly all the videos exhibit a significant vapor depression, although only those in the traditional "keyhole region" described in Fig. 2.6 display the characteristic deep, narrow depression that keyholing was named for, and that is characteristic of deep penetration welds [38], [51], [56]. The exception to this is at low power, where behavior similar to the static beam transitions is observed. For example, the two lowest power cases (104 W and 130 W) at 400 mm/s for $2w_o$ = 95 μm (Fig 7.1a) display a dramatic shift in depths from a shallow round depression at 104 W to a deep, narrow depression at 130 W.

7.2 Keyhole Transition with Scanning Beam

 In order to compare to the depression formation and keyhole transitions measured in the stationary beam experiments to the process map, the curves from Fig. 6.5 were plotted in the process map by converting time to velocity by using the "dwell time" estimate

$$t = \frac{2w_o}{v} \tag{7.1}$$
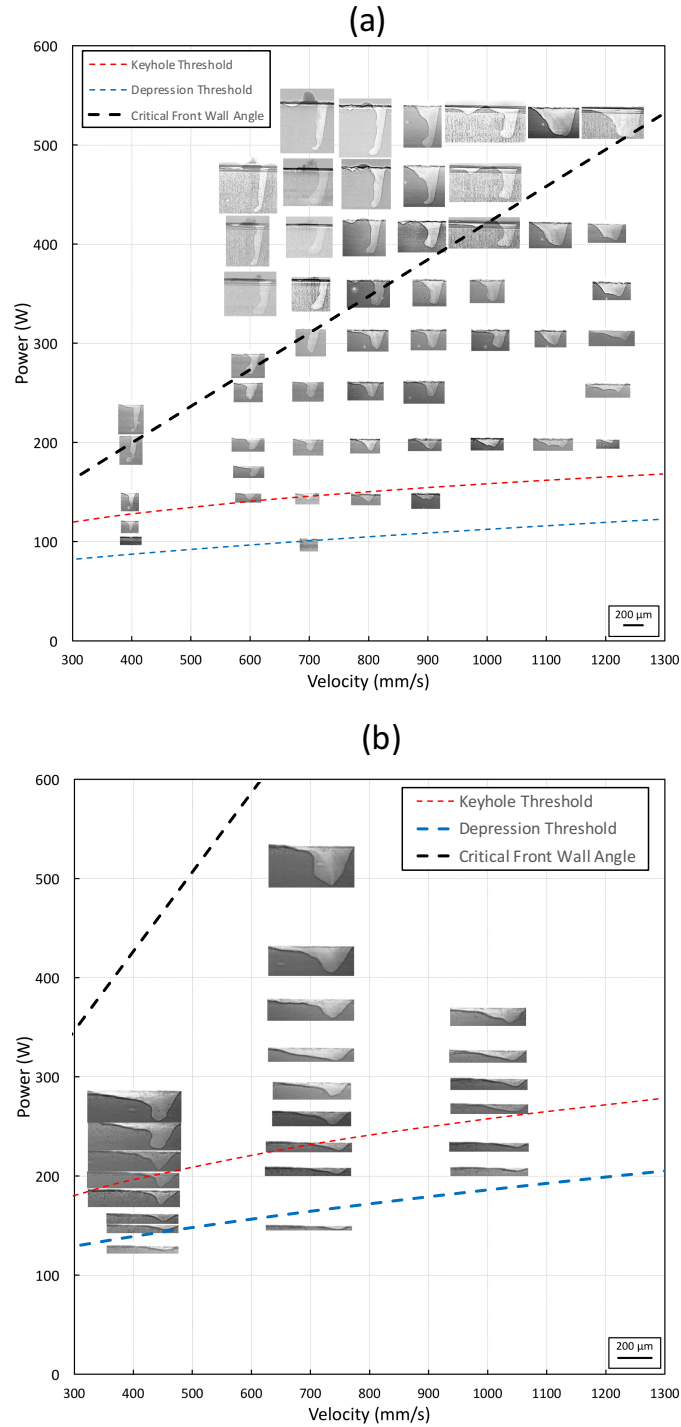
Figure 7.1: Process maps showing vapor depression morphology as a function of laser power and velocity for spot sizes (a) $2w_o = 95$ µm and (b) $2w_o = 140$ µm. The red dashed line indicates the critical power density taken from the fit-lines of the keyhole transition from Fig. 6.5, while the blue line indicates the depression formation threshold. The black line indicates a calculated front wall angle

of 77°, as described in section 7.4. Time was converted to velocity by dividing the spot size by the exposure time (i.e., dwell time).

where $2w_o$ is the laser spot size and v is the beam velocity. Dwell time is a commonly used estimate

of the time over which the laser acts on a given point of material and is useful for constructing 1D

models [28], [44]. The result of this is a threshold for power above which the dwell time exceeds

the critical time to for the vapor depression or initiate keyholing for a given power density based

on the stationary beam experiments.

In the case of the estimation for the vapor depression formation, we see a reasonably good

fit with the limited amount of data collected at those low powers. One interesting takeaway from

this is that by the definition of the keyhole transition being the formation of a vapor depression,

then nearly all of process space for Ti-6Al-4V is technically in the "keyhole" regime at the ~100

µm spot sizes the LPBF machines typically use.

For the keyhole transition, it is apparent that the constructed threshold does not correspond

to a sharply defined transition, but there is a shift in morphology from a shallow, round depression

towards a deeper, more pointed morphology near this boundary, reminiscent of the behavior seen

near the transition point in the stationary beam experiments. This connection is further supported

by observing the behavior of the vapor depressions near the keyhole threshold. As seen in video

S7.1 (140 µm spot size, P = 260 W, V = 400 mm/s), the vapor depression fluctuates between a

shallow, rounded melt pool and a deeper more pointed melt pool. In Fig. 7.1b, the two depression

morphologies at 400 m/s that appear to be keyholing below the estimated threshold both exhibit

these fluctuations. The fluctuations are a result of the vapor depression suddenly penetrating

through the existing liquid under the beam, as was observed at the beginning of the transition in

the stationary beam experiments. These similarities demonstrate that the transitions in the stationary beam and the scanning beam are likely governed by the same underlying physics.

As demonstrated in Chapter 4, this experimental setup is capable of running simulated powder-bed experiments. However, for the purposes of accurately measuring the phase interfaces in an automated way, powder was not used for the keyholing experiments, as it adds interfaces and noise to the images. This will likely result in a lower effective absorptivity, as powder has been observed in multiple studied to increase the laser absorptivity in the pre-keyhole regime [44], [100], as well as change the heat flow characteristics of the top surface, as the powder is a poor thermal conductor and acts to insulate the area around the melt pool. Both of these characteristics mean that the early on-set of keyholing observed here is, at least for this these spot sizes, an overestimation of heat input compared to the case with powder.

7.3 Quantifying Scanning Beam Videos

Similar to the static beam analysis, these videos were quantified by the maximum penetration depth of the vapor depression, but also by the front keyhole wall angle, as shown in Fig. 7.2. The laser scanner software was such that the laser had to be turned on before the scan starts, which results in a deep keyhole that gradually recedes to a steady-state depth as the beam velocity reaches its target value. Therefore, in order to only measure a "steady state" condition, the laser track began outside the observation window and only the frames where the laser was at the target velocity were included in the measurements.

Depth as a function of power and velocity is plotted in Fig 7.3 for the $2w_o = 95$ μm and 140 μm. Figure 7.3a shows that the depth for the $2w_o = 95$ μm experiments follows a highly linear relationship with power. Assuming that the threshold on Fig. 7.1a is valid, nearly all of the data

for this spot size case falls in the keyhole regime, so no transition in behavior would be expected. As the velocity increases, the slope of the depth vs. power curves decreases at a fairly consistent rate, although there is some overlap in the 700-900 mm/s curves, possibly because of some slight variation in spot size between experiments. Similar linear behavior above the threshold is seen for $2w_o = 140$ µm in Fig. 7.3b, although the slopes for a given velocity are considerably lower for the larger spot size, as would be expected for the lower power density. Additionally, because sufficient data was collected below the threshold for $v = 400$ mm/s, the behavior below the transition is also visible. At the transition point, the slope increases dramatically, similar to the behavior seen in the stationary beam experiments. However, for the 700 and 1000 mm/s case, no dramatic transition in observed, though the shallow slopes after the transition because of the higher velocities may mask it. This linear relationship would then suggest that once the keyhole is active (after the transition), the depth of the keyhole is highly predictable.
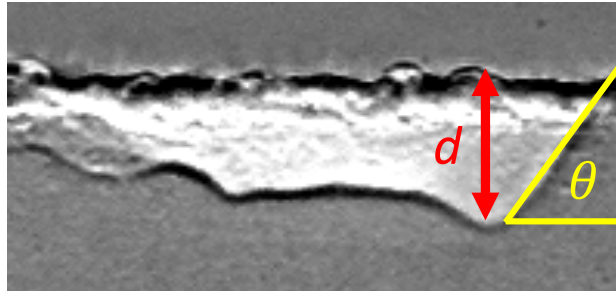
Figure 7.2: Depression depth, *d*, and front wall angle, θ. Beam conditions P=260 W, V = 1.2 m/s, 2*w*$_o$ = 95 µm.

Note that there are some exceptions at high powers and low to medium velocities (400-900 mm/s) for $2w_o = 95$ µm. These outliers, which display a larger depth than a linear relationship would predict, coincide with the morphologies that form a "tail" that trails behind the vapor depression but is not directly under laser illumination. Adjusting this value to the depth of the depression that is directly under the keyhole opening (and therefore presumably under

direct laser illumination), brings the values back closer to a linear relationship. The formation of this morphology is discussed in section 7.5.
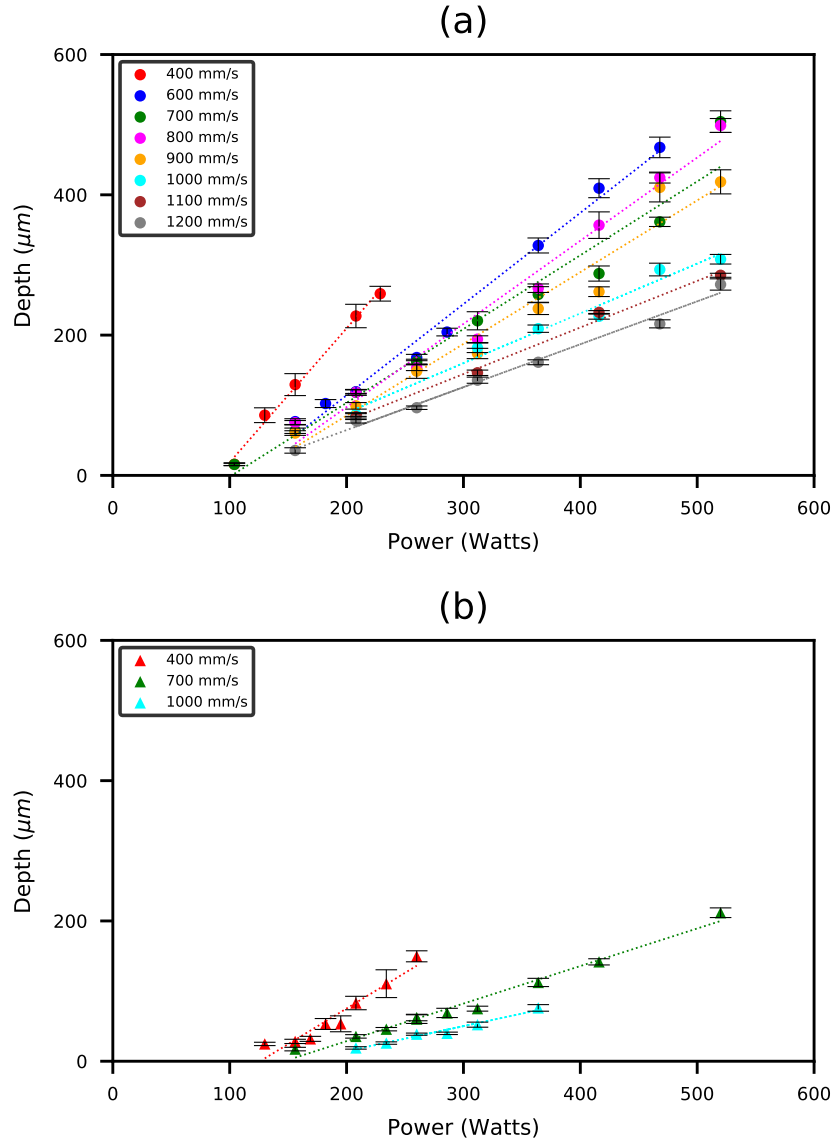
Figure 7.3: Keyhole depth as a function of beam power and velocity for (a) $2w_o$ = 95 µm and (b) $2w_o$ = 140 µm.

Figure 7.4 shows the measured front wall angle as a function of beam power and velocity for $2w_o$ = 95 µm and 140 µm, respectively, which shows that it varies over essentially the entire range of 0 to 90°. The processing parameters are known to have a strong effect on the keyhole

front wall angle, but this has never been studied at process parameters relevant to AM [101], [102]. Additionally, DXR measurements allows for a more accurate determination of the front wall angle. Here, it is evident that, after the keyhole transition, the front wall angle approximately scales with the log of the power density, approaching 90˚. There is a strong effect of beam velocity, with higher velocities shifting the curves towards higher powers, and reducing the slope.

7.4 Predicting Post-Transition Behavior

Full predictions of the morphology and dynamic behavior using multi-physics simulations have been conducted by Tan *et al.* [49] and Khairallah *et al.* [58], among many others. However, these simulations are extremely computationally expensive and difficult to scale, so a focus of this work was to determine what comparatively simple trends could be used to predict the vapor depression behavior.
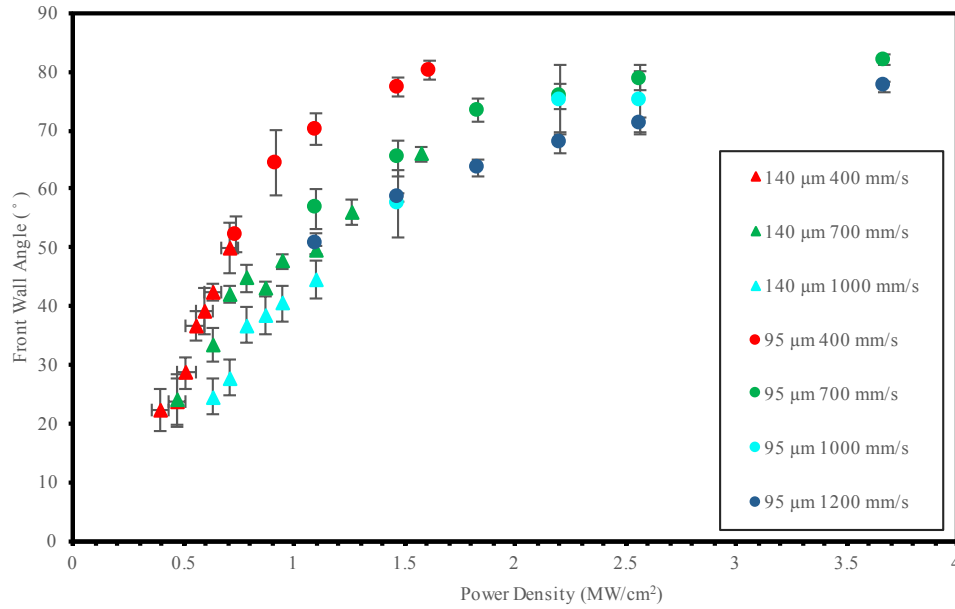
Figure 7.4: Keyhole front wall angle measured as a function of power density and velocity for spot sizes $2w_o = 95$ μm and 140 μm.

Fabbro *et al*. suggested a simple model for determining the front wall angle and penetration depth, excluding the influence of multiple reflections and angular dependence of absorption [52]. In this model, the keyhole front wall angle is simply determined by

$$\tan(\alpha) = \frac{V_w}{V_d} \tag{7.2}$$

where V_w is the beam velocity, $V_d(P)$ is the "drill rate" of a stationary laser for a given power density on a flat surface, and $\alpha = 90° - \theta$. Following this, and assuming a beam of equal intensity, the penetration depth is simply

$$d = \frac{2w_o}{\tan(\alpha)} . \tag{7.3}$$

To test this model, V_d was measured from the slope of Figs. 6.2b & d after the keyhole transition. Fig. 7.6 shows the results from two different methods of determining the drill rate from the data in Fig. 6.2. One method, denoted as "Full" took the slope from the entire region post-transition. However, it was assumed the significant fluctuations that develop later in the keyhole

regime would add noise to the drill rate that would not necessarily be relevant to a scanning beam experiment, so only the slope from the beginning of this regime was also measured and used for this prediction, however the accurate drill rate could feasibly fall anywhere between these two cases. In developing this model, Fabbro *et al.* assumed that the drill rate varies linearly with applied power, which appears to be a reasonable assumption based on the measurements from the laser drilling experiments.

Using the power density dependent drilling rate shown in Fig. 7.6 and Eq. (7.2), the estimated front wall angle was calculated as a function of power density and beam velocity, Fig 7.7. Despite not taking into account a number of other variables accounted for in more complicated simulations, such as the angular dependence of absorption or the effect of multiple reflections [103], it is clear the simple relationship captures the trends in the variation of the front wall angle with power, and is particularly accurate for the $2w_o = 95$ μm data. Interestingly, the accuracy of this simple model suggests that over the process space relevant to AM, the front wall angle is mostly dependent on the ratio of the beam velocity and drill rate, with little influence of secondary reflections. The impact of secondary reflections on keyhole shape is discussed further below.
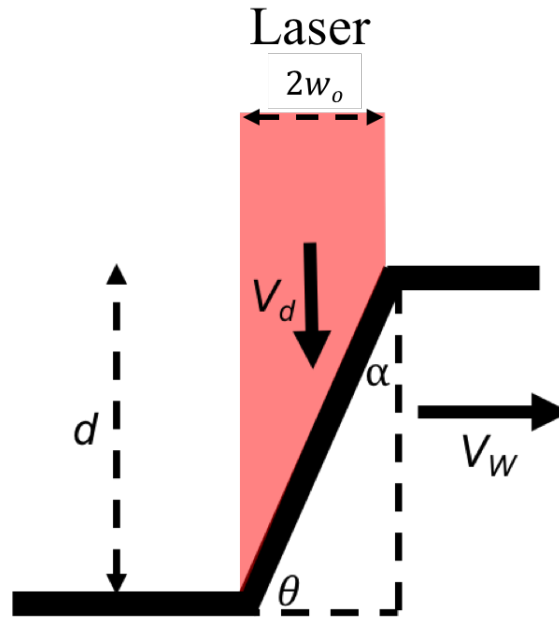
Figure 7.5: Schematic of keyhole depth and front wall angle. Adapted from Fabbro et al. [52]

Following this, an estimated keyhole depth was calculated from the estimated front wall

angle using (7.3). It was clear that this model captured the behavior of the keyhole depth as a

function of processing parameters seen in Fig. 7.3 but using the full beam sizes of 95 μm and 140

μm overestimated the depths by a factor of ~2. This model assumes a top-hat distribution of power,

whereas in reality this is a Gaussian source, which will concentrate the power at the center of the

beam. Therefore, instead of the full beam widths, the critical depression widths of ~50 μm and

~100 μm for the 95 μm and 140 μm respectively, as discussed in Chapter 6 (width of depression

in Fig. 6.3), were used as an estimated spot size. Using these values, the estimated depths for

selected spot size/velocity combinations in Fig. 7.3 were calculated, Fig. 7.8.
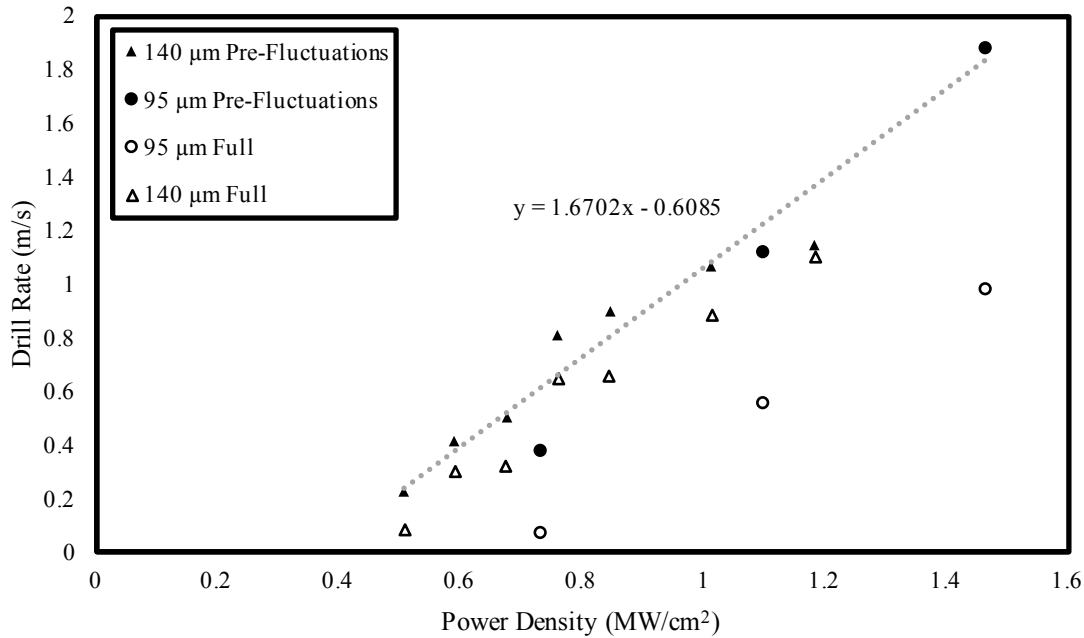
Figure 7.6: Drill rate, V_d, as a function of power density, measured from Fig. 6.2.

As with the keyhole front wall angle, this model shows promise for predicting the keyhole depth as simply a product of power and velocity. Given the simplicity of the model, the degree of accuracy for the 95 μm case, once accounting for the lower beam diameter, is somewhat surprising. The overestimation for the 140 μm case is not severe but is obviously less accurate. Given the overestimation of the front wall angle, this likely stems from an overestimation of the drill rate for this spot size. Further work is required to fully understand the evolution of this drill rate as a function of material properties and laser parameters. Regardless, this model shows promise for a simple approach to estimating keyhole depth and front wall angle that doesn't require considerable computational resources. The engineering implications of these two factors are discussed in the next section.
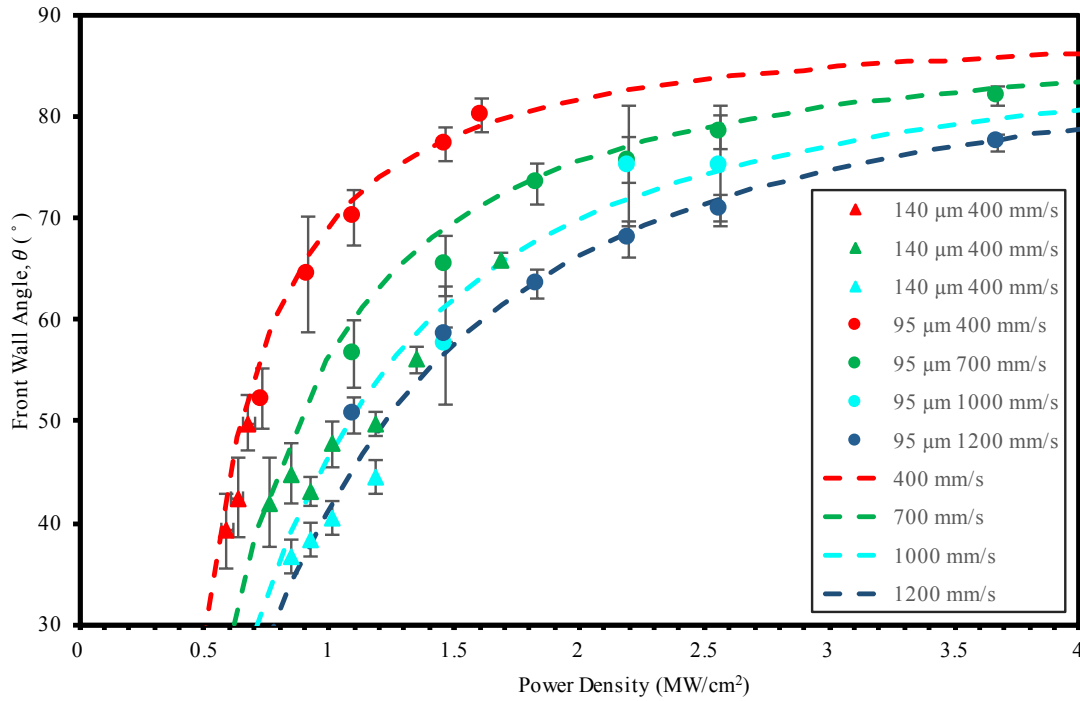
Figure 7.7: Estimated keyhole front wall angle compared to experimental results for select beam velocities.

7.5 Keyhole Morphology and Defects

Significant effort has been invested in investigating porosity formation in electron beam and laser welding, particularly "keyhole porosity" [24], [26], [28], [55], [57], including some in-situ x-ray radiography using non-synchrotron sources [50], [51], [56], [77], [104]. However, none have utilized a synchrotron source to capture in-situ dynamic behavior at the time and spatial resolution that these techniques enable. This section covers how the morphological variations in the keyhole across process space discussed earlier in the chapter can lead to defects.

Fabbro *et al.* discussed the possible implications of how variations in the front wall angle would change the direction of the secondary reflection, and how that would impact the depression morphology and effective absorptivity within the melt pool [52]. Simulations to capture the full effect of the secondary reflections are beyond the scope of this work, but the effects can be seen qualitatively, Fig. 7.9.
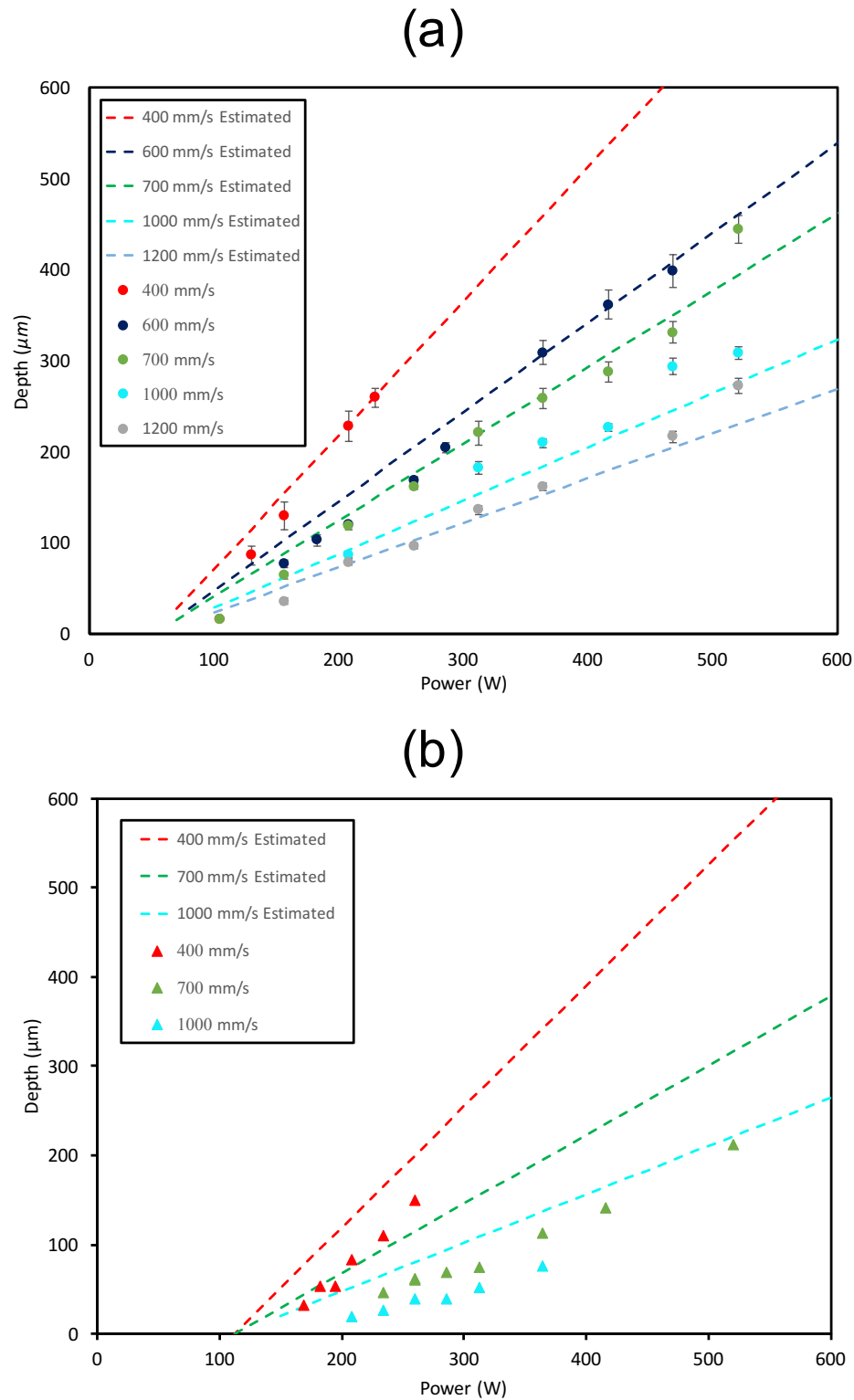
Figure 7.8: Comparison between measured keyhole depths and model estimates for (a) $2w_o = 95$ µm, and (b) $2w_o = 140$ µm. Adjusted beam widths of 50µm and 100µm used for the $2w_o = 95$ µm and 140 µm respectively.

It is well accepted that the steep front wall angles in a deep penetrating keyhole focus the reflections towards the bottom of the keyhole, increasing penetration beyond what would be predicted by the simple single reflection model established in the previous section. This is potentially the source of the "tail" observed in Fig. 7.9a, which extends the penetration depth beyond the front wall being directly illuminated by the laser. Conversely, it was argued that the shallower front wall angles that were observed at higher velocities would act to reflect the incident beam more horizontally thereby increasing the width of the depression and reducing the number of secondary reflections fully captured and absorbed by the melt pool, as some would be reflected out of the surface. This is supported by the results shown in Fig. 7.9b, where the high velocity depression has an elongated morphology. Additionally, Trapp et al. measured a lower peak absorptivity at high velocities [44]. This relationship is particularly important for understanding and preventing the formation of defects, which is the main focus of this work.
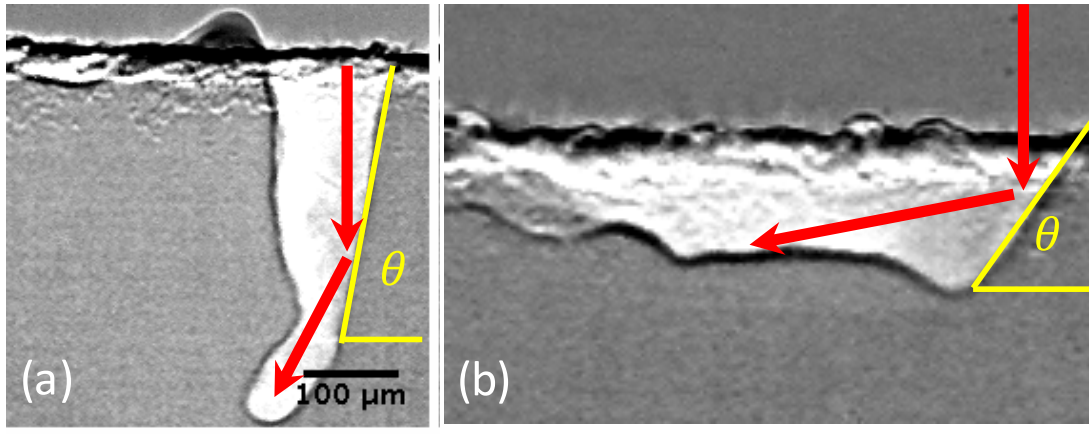
Figure 7.9: Schematic of angular dependence of laser reflection by front wall angle. $2w_o$ = 95 μm (a) 416W, 0.8 m/s. (b) 260W, 1.2 m/s.

7.5.1 Formation of Keyhole Porosity

The general mechanism behind "keyhole porosity" as the collapse of the vapor cavity in high aspect ratio vapor depression, such as those observed in this work to form at steep front wall

angles, has been fairly well established. Figure 7.10 and video S7.2 illustrate the mechanism where fluctuations on the front and back keyhole walls collide, resulting in a pinched-off bubble containing the gas within the vapor cavity. Previous investigations have established this is a mixture of the atmospheric/shielding gas as well as vaporized alloying elements within the metal [50]. A bubble once formed is ejected backwards towards the solidification front. A pore is carried clockwise within the melt pool, likely by a combination of the Marangoni driven fluid flow and buoyancy forces, until it intersects the solidification front and becomes fixed.

Despite most of the processing space falling into what has been established in this work as the "keyhole regime", it is clear that this porosity can only form with a specific vapor depression morphology, accompanied by strong enough fluctuations on the front and back keyhole walls in relation to the width of the vapor cavity. Referring back to the process map of Fig. 7.1, it is clear that this morphology is limited to the high power, low velocity region of the map, as suggested in the experimental maps discussed in the introduction, Fig. 2.6. Velocity largely determines the propensity for keyholing, as even the deep, high aspect ratio depressions become more stable at higher velocities. Eventually, at sufficiently high velocities, it becomes impossible to form a traditional "keyhole" depression within the power limits of this laser for this spot size for a baseplate starting at room temperature.

Comparing Figs. 7.1a & b shows how much the morphology is influenced by the spot size. To compare the two, Eq. 7.2 was used to calculate the power and velocity combinations that resulted in a front wall angle of 77˚, above which were most of the high-risk morphologies, as shown in Fig. 7.1. Note that a high-risk morphology does not necessarily mean that keyhole pores will form, as many of the experiments that exceeded this threshold did not form keyhole porosity within the 2 mm scan track, even if they exhibited fluctuations. However, given that the length of

the scan track we were able to observe was small compared to the length of most scan tracks, and the number of experiments per process parameter combination was often limited to one, we cannot conclusively say that keyhole pores do not form with a given geometry; one can only note whether they were observed or seemed likely (e.g., high-risk). Further investigation into this second transition (e.g. stable to unstable keyholing) deserves further investigation. Regardless, it is clear that while a large portion of process space at the lower laser spot size results in a "high risk" morphology, almost none of the *P-V* combinations at 140 μm fall into this category. While there may be some drawbacks to using a larger beam size such as reduced feature resolution, the ability to avoid keyhole formation over a larger area of process space could be a significant benefit in some applications, as noted by Francis [13].

7.5.2 Keyhole Formation at Turnaround

The previous discussion of keyhole pore formation focused on the "steady state" behavior of the vapor depression at constant beam velocity and thermal conditions. However, the AM processes necessarily contain many areas where these conditions are no longer true, such as at the end of tracks where the beam turns around. These next two sections focus on the potential defects that occur at these "non-steady state" regions. While not covered in depth in this work, it was observed that a deeper keyhole was formed when melting a region that had recently been melted, and therefore was at an elevated temperature. Groeber *et al*. found that locations where the beam turned around after finishing a track experienced higher temperatures than at the center of a raster [59].

Fig. 7.11 and video S7.3 show two adjacent laser tracks in the region near the beam turnaround. In the first track, the keyhole depression was not a morphology that was susceptible to keyhole pore formation. However, despite a hatch spacing of 100μm, when it passed over the already heated area, the vapor depression geometry changed considerably, and a keyhole pore was

formed. While a systematic study including temperature probes and thermal modeling did not fall

within the scope of this work, it is clear that operating at a preheat has a similar effect to operating

at a higher power and can likely be estimated as such.
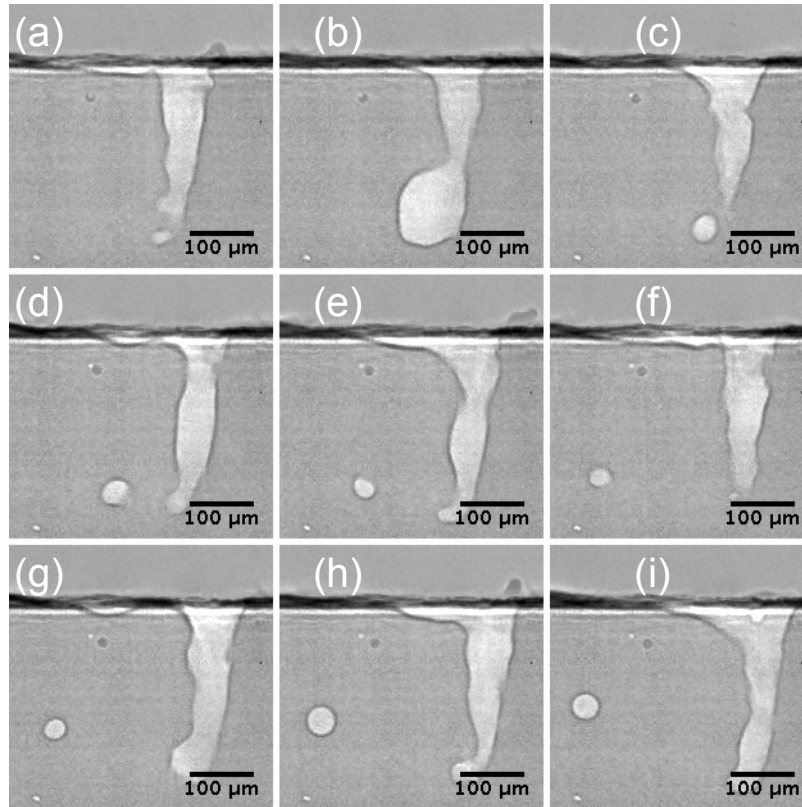
Figure 7.10: Frame-by-frame view at 50kHz of a pore being ejected from a deep penetrating keyhole vapor depression in Ti6Al4V. After pinching off (c), the pore is carried in a clockwise rotation by the fluid flow until it intersects the solid liquid interface and becomes fixed in place (i). Beam conditions: 230 W, 400 mm/s, 95 μm spot size. Full video: S7.2.

7.5.3 End of Track Porosity

Just because keyhole porosity may be relatively easily avoided by operating at processing

conditions well below the critical front wall angle threshold does not mean the significant

depressions observed in other regions of process space will not contribute to defect formation. In

particular, is the concern of "end of track" porosity. In simulations performed by Khairallah *et al*.,

it was speculated that the rapid collapse of a keyhole at the end of a laser scan track, because of

the rapid turn-off of the laser, could result in a forced keyhole pore [58]. However, this was only investigated for one keyhole morphology, so it is not clear how it will change with the dramatic differences in vapor depression morphology observed in Fig. 7.1. Groeber *et al*. also investigated this using x-ray computed tomography and identified it as a major source of defects that are location dependent based on your scan strategy (i.e., stripe boundaries) [59].
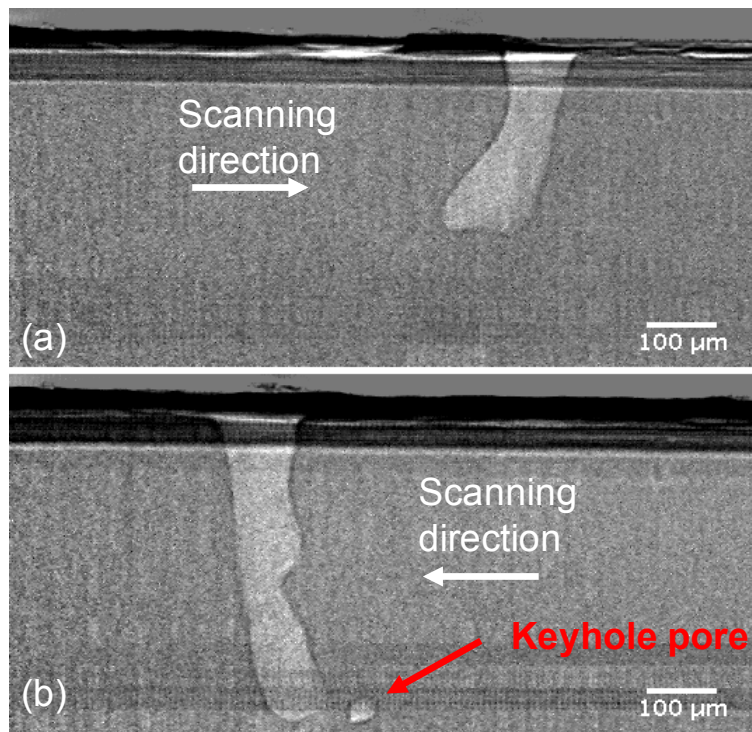
Figure 7.11: Effect of a preheat experienced at beam turnaround on the vapor depression depth and morphology. The vapor depression on the reverse direction over the pre-heated material is considerably deeper, and results in a keyhole pore despite the initial morphology not being susceptible. Beam conditions: P = 364 W, V = 0.7 m/s, $2w_o$ = 95 µm. Full video: S7.3.

Two cases representing a low velocity/steep front angle wall and high velocity/shallow front wall angle depression are shown in Fig. 7.11, and videos S7.4 & 7.5. It is clear that the different vapor depression morphologies result in significantly different defects due to differences in formation mechanism. For the low velocity vapor depression, the liquid along the keyhole back wall that was supported by the vapor is allowed to suddenly collapse forward when the laser is

turned off. The top of the depression collapses first, effectively trapping the gas existing within the depression at that time and forming a pore. Additionally, insufficient liquid existed to completely fill in the depression before solidifying, resulting in the depression on the surface. Similarly, for the high velocity case, the direction of the liquid appears to be opposite of the beam travel direction. This, coupled with the rapid solidification front traveling from the front keyhole wall, effectively freezes the morphology of the vapor depression into the solidified material. While the latter two are not fully enclosed defects, they do add ~100 μm in extra depth that needs to be filled in by a subsequent pass. Insufficiently filling this in would, in effect, create a LOF defect even if the basic conditions for melt pool overlap were met for other regions of the melt track.
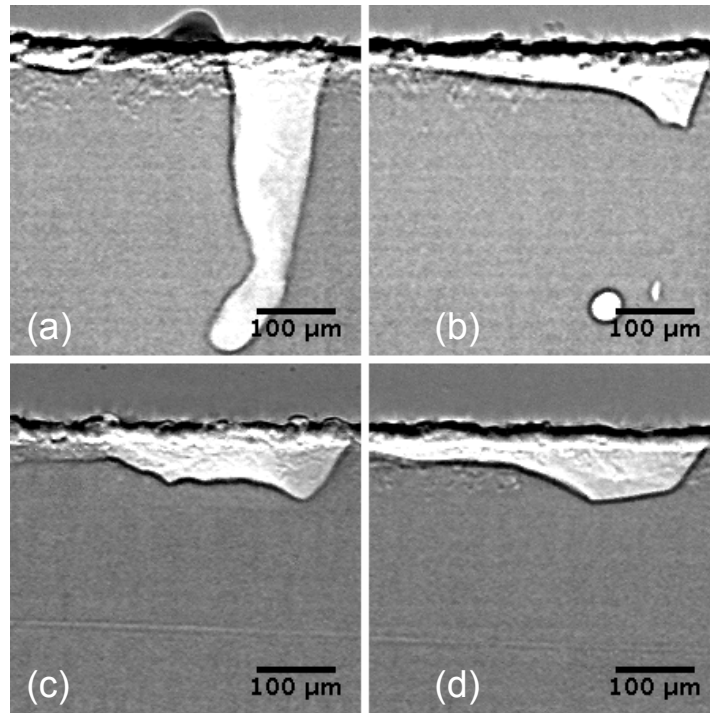
Figure 7.12: Influence of vapor depression morphology (left) on end of track pores (right). Deep keyhole depressions can result in closed-off pores resembling "keyhole pores" while shallow vapor depressions get "frozen" because of the rear-ward flow of liquid, resulting in an open defect. Full video: (a, b) 7.4, (c, d) S7.5.

7.6 Discussion

The vapor depression and keyhole transition for a scanning beam in Ti-6Al-4V is observed to follow similar behavior to the observations in the stationary beam experiments but is obviously complicated by the addition of the moving melt pool. While estimation for vapor depression formation based on the energy balance between recoil pressure and surface tension appears to apply to the moving beam, the keyhole transition does not appear to be as sharp as what was observed in the static beam case, except at low velocities. Having said that, it is clear that for a moving beam, the presence of a vapor depression does not serve as an effective boundary to separate conduction mode melting from the deep penetrating keyhole morphologies that can lead to porosity. This supports the previous findings from laser welding of a "transition region" between

conduction mode, characterized by the lack of a vapor depression, with the region of significant and possibly detrimental keyhole vapor depressions [47].

Further complicating this idea of single a keyhole boundary is the wide variety of depression morphologies across process space. Simply crossing the boundary in Fig. 7.1 does not predict the same behavior for all process conditions. Fortunately, it is clear that at some point near this boundary, the characteristics of the vapor depression, at least in terms of depth and front wall angle, become predictable. Lacking further understanding of the physics surrounding the keyhole transition observed in the spot beam, it is arguable that this point at which the depression behavior begins to be governed by the "drill velocity" could be considered the useful definition of the keyhole transition, as this can subsequently be used to identify regions which give detrimental morphologies, such as the critical front wall angle described here. While the model discussed in section 7.4 has considerable room for improvement, it should be noted that for the purposes of AM, avoiding those defect-inducing morphologies is sufficient, as there is little benefit in operating in that region of process space, unlike for laser welding where deep penetrating keyhole welds are necessary in certain situations.

While it is important to properly control the "steady state" behavior of the vapor depression, neglecting to take into account the influence of the vapor depression in non-steady state regions is both equally as important and more difficult to control. While this worked focused on identifying the mechanisms that can form in these conditions, considerable process optimization and modeling will be required to properly alter the laser parameters in these locations to prevent defect formation. Additionally, in order to fully take advantage of the feature resolution and design freedom of metal AM, additional potential areas of non-steady state behavior such as overhangs or thin walls [105] need to be investigated.

7.7 Conclusions

Overall, the findings from the study of vapor depression morphology of a moving beam can be summarized as:

i.   The formation of a vapor depression occurs at conditions comparable to a stationary beam.

ii. The keyhole transition predicted by the spot beam experiments generally identified a region where a change in morphology from shallow to pointed occurred. A sharp keyhole transition as observed for the spot beam experiment was only observed at low velocities. In most cases a transition region was observed.

iii. The connection between the transition to a sharp keyhole and the formation of defects is indirect and deserves further attention.

iv. Beyond this transition, the depth and front wall angle followed predictable trends as a function of the velocity and power-density dependent drill rate.

v.   The morphology of the vapor depression is directly linked to the propensity for defect formation. Front wall angle appears to be the dominant characteristic determining morphology, which is further related to the depth through the spot size.

Chapter 8: Porosity Regrowth Following Post-HIP Heat Treatment

This study aims to utilize the higher resolution of μSXCT to determine the effect of a standard HIP treatment on defects in EBM and LPBF Ti-6Al-4V and measure their potential re-growth after a subsequent β-solution heat treatment. To investigate this effect on trapped gas porosity observed in EBM samples, an identical set of samples as fabricated for the experiment in section 4.1 were studied. To investigate this effect on processing flaws in LPBF Ti-6Al-4V, namely keyholing and lack of fusion, samples 2 & 4 from Chapter 5 (Fig. 5.1) were studied after they had been imaged in their as-built state. Sample 2 was identified as having keyholing pores, while sample 4 had lack of fusion pores. Samples underwent a HIP treatment of 900 ˚C for 2 hours at 103 MPa in argon, in accordance with ASTM F 2924. To investigate potential regrowth, the HIPed samples underwent a β-solution heat treatment of 1050 ˚C for 10 min after initial imaging and were rescanned at the same locations. In all samples, pores were observed in the as-HIPed state, and partial regrowth of gas containing pores were observed after heat treatment.

8.1 Thermally Induced Porosity (TIP)

8.1.1 TIP of Powder Porosity

Results from the HIPed and post-HIP heat treated samples from the Arcam EBM Ti-6Al-4V samples discussed in section 4.1 are shown in Fig. 8.1b, c, e & f, with the results from section 4.1 representing their approximate as-built state from scans of equivalent areas of in a similar bulk sample in the as-built state. Pore statistics are summarized in Table 8.1. The HIP process largely reduced the size of the pores pores from the as-built condition, but small pores below ~5 μm were still detected in both the AP&C and TIMET samples. As with the as-built condition, more pores were detected in the AP&C HIPed sample than the TIMET. After heat treatment, the number and

maximum size of pores increased in both sample, indicating coarsening of pores during the heat

treatment.
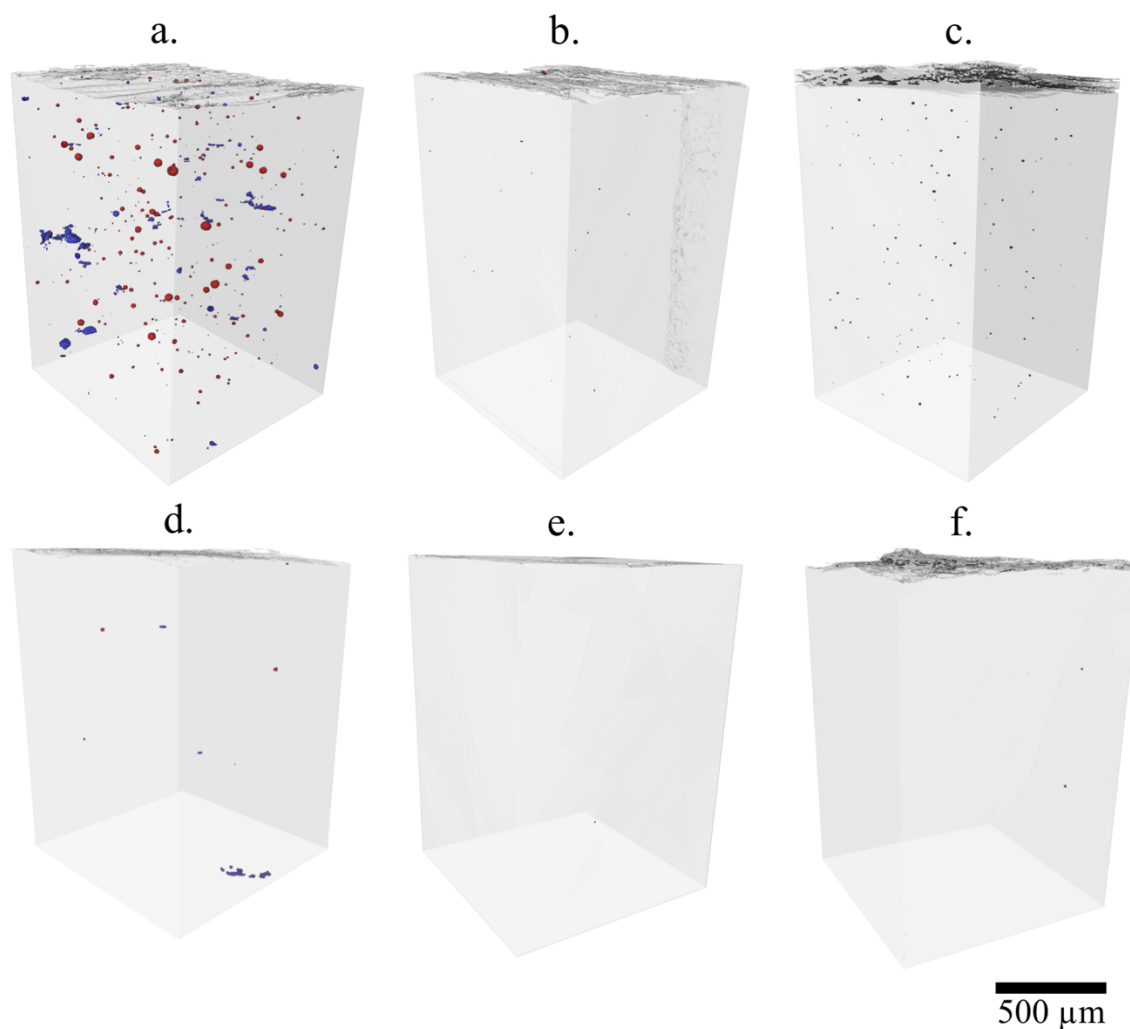
Figure 8.1: μSXCT results showing porosity in samples built from AP&C (a)-(c), and TIMET (d)-(f). From left to right, the sequence of samples is, as-built (a & d), HIPed (b & e), and HIPed + β solution heat treatment (c & f).

Table 8.1: Porosity statistics from HIPed and Post-HIP heat treated Arcam EBM samples.

	Volume Fraction $(x10^4)$	# Pores per mm^3	Ave. Eq. Diam.	Max Eq. Diameter
AP&C HIP	$7.65x10^{-3}$	35	3	6
AP&C HIP + HT	$1.36x10^{-1}$	131	5	10
TIMET HIP	$5.09x10^{-4}$	1	5	5
TIMET HIP + HT	$3.89x10^{-3}$	2	7	8

Fig. 8.2 shows the same pore in the HIP and post-HIP heat treated condition for each sample. Pores showed an approximately 200 % growth in size after heat treatment. In both cases, however, the lack of fusion porosity, which is assumed to be truly void because of the vacuum environment in the machine, appeared to be eliminated with the HIP process within the resolution of this experiment. This is, however, impossible to confirm as data was not collected for these samples in the as-built condition.
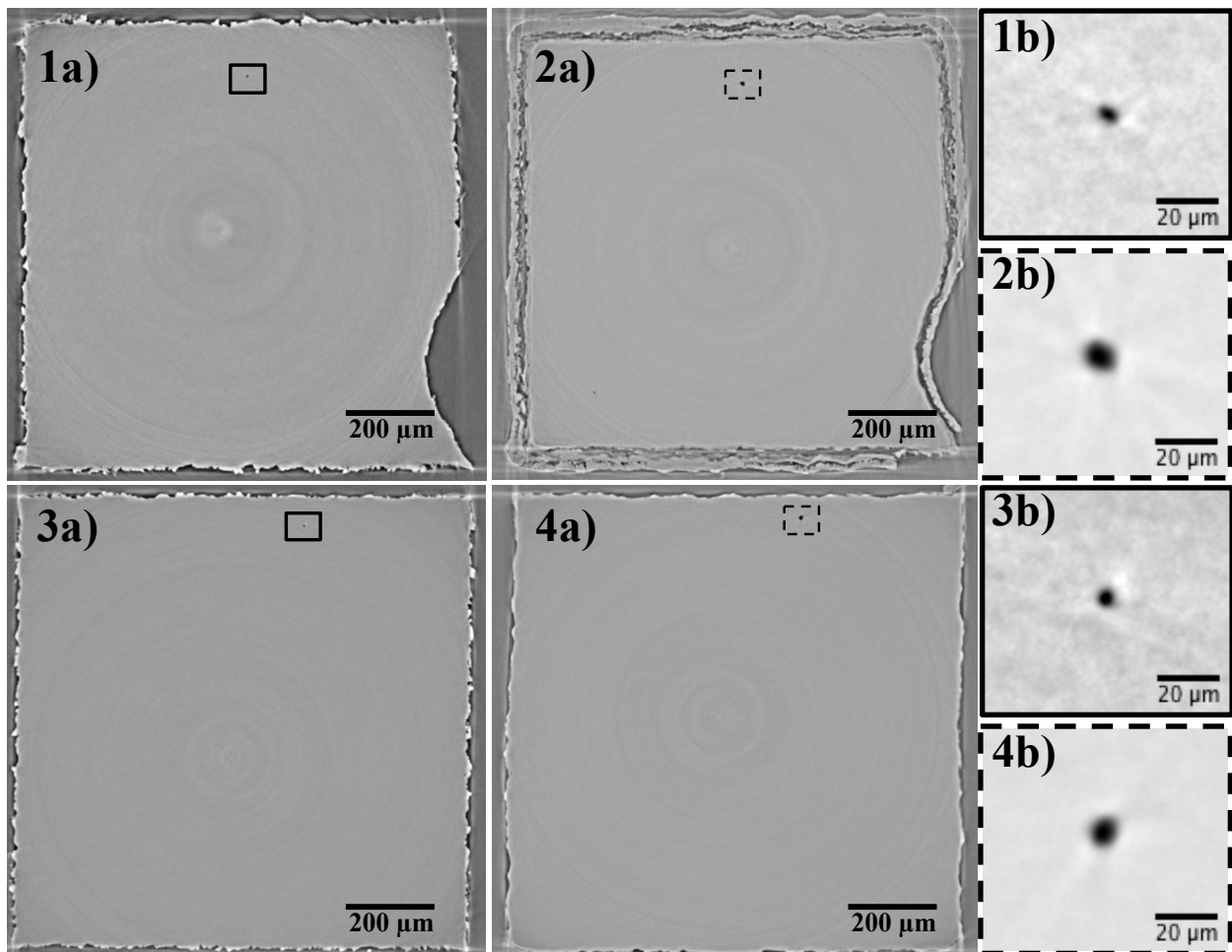
Figure 8.2: Reconstructed slices of the 1a) APC HIP, 2a) APC HIP + heat treatment, 3a) TIMET HIP and 4a) TIMET HIP + heat treatment, showing the same pore before and after solution heat treatment, with corresponding magnified images of the pores (1b-4b). Pore diameter grows approximately 200 % from the HIPed condition after β-solution heat treatment.

8.1.2 TIP of Lack of Fusion and Keyhole Porosity

Fig. 8.3 shows samples 2 & 4 from Chapter 5 in the as-built, HIPed and post-HIP heat treated samples. Pore statistics are summarized in Table 8.2, and the size distribution of pores are given in Fig. 8.4. As with the porosity in the EBM samples, the HIP process largely reduced the lack of fusion and keyhole pores from the as-built condition, but small pores below ~7 μm were still detected in both the keyhole and lack of fusion samples. Similarly, the pores were observed to coarsen after post-HIP heat treatment by approximately 200 %.
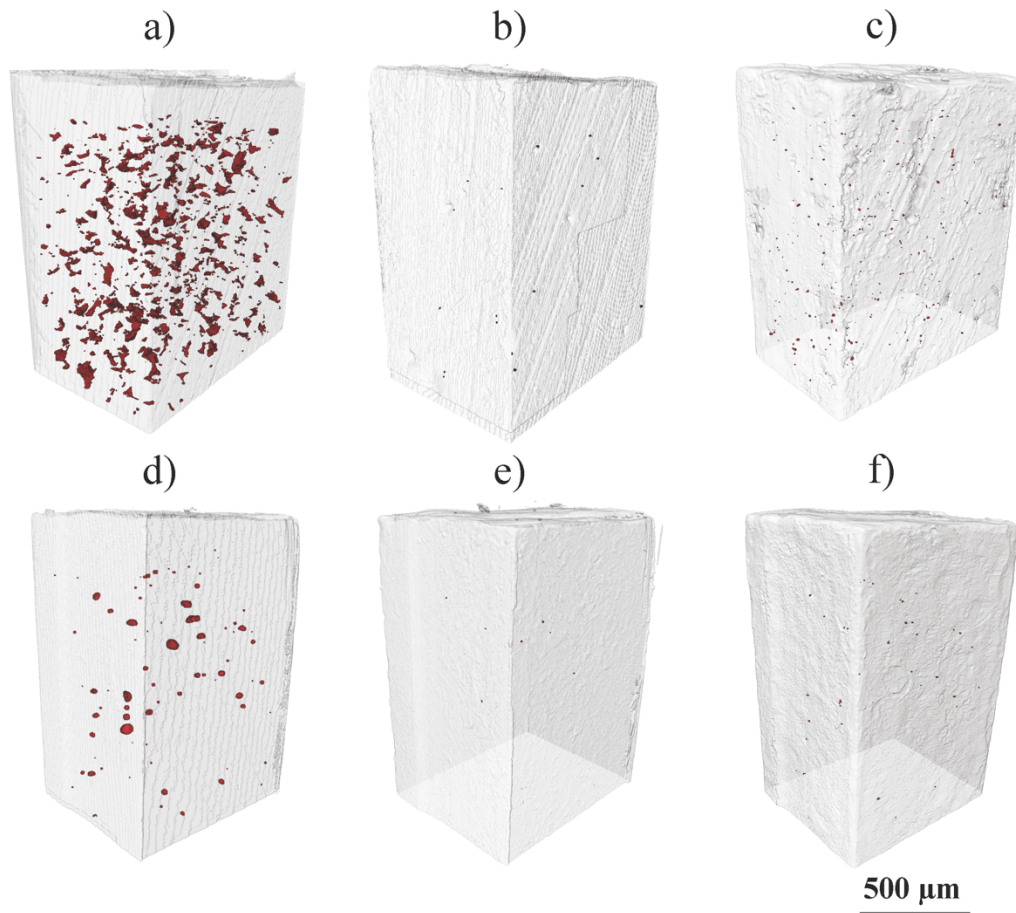
Figure 8.3: μSXCT results showing lack of fusion (a-c) and keyhole (d-f) porosity in as-built (a, d), HIPed (b, e) and heat treated (c, f). Remnants of both types of processing flaws are visible in the HIPed condition, with regrowth observed in heat treated samples.

Table 8.2: Porosity statistics from samples 2 & 4 in the as-built, HIPed and Post-HIP heat treated condition.

Sample	Number per mm³	Maximum Eq. Diameter
LOF	688	63
LOF HIP	34	7
LOF HIP + HT	239	15
KH	68	56
KH HIP	5	7
KH HIP + HT	37	13
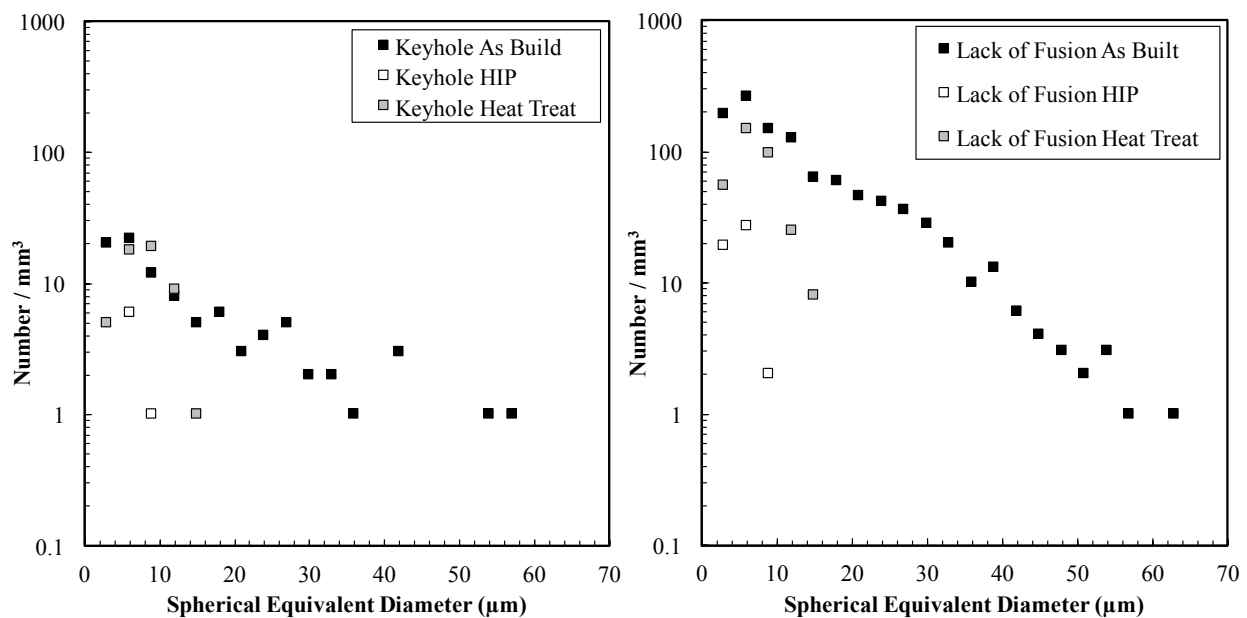
Figure 8.4: Size distribution of processing related pores at each stage of processing (as-built, HIP, and heat treatment) for keyhole porosity (left) and lack of fusion porosity (right). Both lack of fusion and keyhole pores reduced to <10 μm spherical equivalent diameter with a HIP treatment, and partially grow back after heat treatment.

Because μSXCT data was collected for these samples in the as-built condition, individual pores were able to be traced through each step of processes. Fig. 8.5 shows a representative lack of fusion pore and keyhole pore through each stage of processing. The lack of fusion pore is observed to form a small cluster of pores when HIPed, which subsequently regrows into a connected string of pores after heat treatment. The more regular shaped keyhole pore is observed to maintain its morphology or closely throughout each processing step. These results indicate that

the initial morphology of the pore in the as-built condition can influence the resulting pore after

regrowth at high temperature.
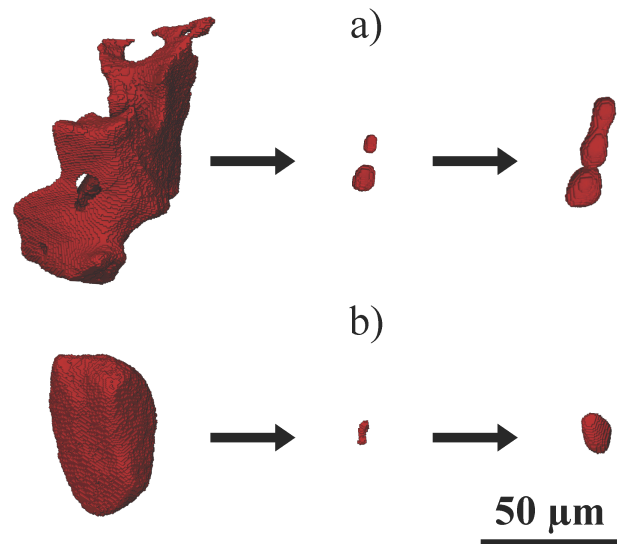
Figure 8.5: Morphology change through each stage of post-processing for a representative (a) lack of fusion defect and (b) keyhole pore. The irregular shape of the lack of fusion pore in the as-built condition is observed to influence the final morphology of the regrown pore. In contrast, the more spherical keyhole pore shows less variation throughout each processing step.

8.2: Discussion

Results from Arcam EBM samples from the AP&C and TIMET Ti-6Al-4V powders in the HIPed

and post-HIP heat treated condition are shown in Figs. 8.1b, c, e & f. Previous work using lab-

scale μXCT with feature resolution of ~ 5 μm did not detect any porosity in the HIPed condition,

although cross section analysis suggested the presence of incompletely closed pores [5][106].

Given the assumption that the gas porosity originates from insoluble gas transferred from the

powder, it is reasonable to expect the HIP process to shrink but not entirely eliminate pores. To

our knowledge, the higher resolution of the synchrotron μSXCT, with feature resolution of

approximately 1.5 μm, has for the first time detected pores in the HIPed condition using μXCT,

all of which are at or below the resolution limit of the previously used instruments (~ 5.5 μm). While this was to be expected with the plasma atomized powder samples, pores were also detected in the PREP samples, which provides further evidence for the presence of inert gas porosity originating from the PREP powder. In both cases, however, the lack of fusion porosity, which is assumed to be truly void because of the vacuum environment in the machine, was eliminated with the HIP process within the resolution of this experiment.

The continued existence of this porosity after HIPing raises a concern for post-HIP heat treatments or high temperature operating conditions because of the potential for pore regrowth. This process has been utilized to good effect in the manufacture of titanium foams, and Tammas-Williams *et al*. showed evidence from μXCT of pore regrowth with EBM Ti-6Al-4V after a β-solution treatment, however they were not able to observe pre-existing pores in the HIPed condition [12], [63], [64]. Figs. 8.1 & 8.2 show that pre-existing pores detected in the HIPed Arcam samples do in fact coarsen after heat treatment. In both cases, the number density of pores in the post-HIP heat treated samples displayed a similar, albeit smaller number of gas pores compared to the as-built sample. This is to be expected, as pores near the resolution limit in the as-built state would likely not regrow to within the resolution limit after the HIP/heat treat cycle, resulting in fewer pores detected in the final state. Interestingly, the pores in the HIPed AP&C and TIMET samples regrew to approximately the same size, despite the initial pores in the AP&C as-built sample being much larger. This result warrants further investigation of the kinetics of pore coarsening. Regardless, these results suggest that powder with low porosity such as PREP would be the ideal choice for parts that must be subjected to a high temperature post-HIP heat treatment, or are exposed to high operating temperatures, as there would be less risk of re-growth of pores after HIPing.

The processing flaws in the LPBF Ti-6Al-4V behaved similarly to the gas pores in the EBM Ti-6Al-4V (Fig. 5.13). The typical morphologies of lack of fusion and keyhole pores are visible in the as-built conditions, with the former having highly irregular and sharp features and latter being more spherical or globular. In the HIPed condition, pores are visible in both the lack of fusion and keyholing samples, suggesting that these pores do in fact trap argon from the atmosphere in the EOS machine. This further supported by the subsequent regrowth observed after the heat treatment, and also indicates that it is present at sufficiently high pressure to cause regrowth at the applied temperature, which was the main focus of this investigation. Matsunawa *et al.* detected shielding gas inside a keyhole pore, but it was unclear if the gas trapped inside keyhole pores within an LPBF machine would be sufficient internal pressure to be relevant after the HIP process [50]. Likewise, it was suspected but not ever observed that lack of fusion pores would exhibit this behavior, although it is a reasonable assumption that they are approximately at the internal pressure of the build chamber when they form

Registering every pore through each processing step is challenging for the lack of fusion pores because of their high number density and the tendency of the irregular shapes to collapse into a cluster of smaller pores that subsequently coarsen. As such, one representative lack of fusion pore that was successfully isolated was used to compare the differences in regrowth behavior between the irregular morphology and a more spherical keyhole pore. Figure 8.5 shows the progression of pore morphology through each post-processing step. The lack of fusion pore was observed to form a small cluster after HIPing, which subsequently coarsened and merged into a high aspect ratio defect after heat treatment. Despite being more irregular than previously observed gas pores, the keyhole pore behaved similarly in that it shrank and appeared to nearly collapse, before regrowing into a nearly spherical pore after heat treatment. The irregular regrown pore from

the original lack of fusion pore does potentially raise concerns, as pores on the order of 20 µm have been observed to be deleterious to fatigue properties [107], [108], but it still represents considerable improvement from the initial irregular morphology.

β-solution treatments can be useful for AM Ti-6Al-4V as the have been shown to be effective at removing the columnar prior-beta structure present in the as-built microstructure of, for instance, EBM Ti-6Al-4V [16]. However, the considerably lower creep resistance of Ti-6Al-4V makes this allow susceptible to the observed creep controlled pore growth [64], [109]. More troubling, however, are alloys that require significant post-processing after a HIP step, such as precipitation hardened alloys, e.g. Inconel 718. Having established that numerous types of defects in metal AM contain sufficient gas to expand at high temperatures, further investigations into other alloys systems of interest should be undertaken, particularly those destined for high temperature critical applications.

8.3 Conclusions

The findings from the study of thermally induced pore regrowth can be summaries as:

i.   All pores containing inert gas were observed to coarsen after exposure to temperatures above the Beta-transus where creep properties for Ti-6Al-4V are diminished.

ii.   Initial pore morphology influenced the morphology of the pore after the regrowth process.

Chapter 9: Conclusions and Future Work

9.1 Conclusions

In the present work, advanced synchrotron x-ray based characterization techniques are utilized to study defect formation mechanisms in powder bed metal additive manufacturing processes. High resolution X-ray computed tomography allowed for the visualization of trends in porosity for a large number of samples from different powders, machines, and regions of process parameters space, at resolutions superior to those of lab scale instruments. Also, as this is one of the pioneering efforts utilizing the Dynamic X-ray Radiography technique to acquire real-time measurements of the dynamic behavior occurring as a result of the laser-metal interaction, new and important insights into the process of laser powder bed fusion have been uncovered.

The objective of this work was twofold; first, to establish concrete experimental verification of assumed defect formation mechanisms that as of yet were unproven, and to utilize the developing capabilities of the DXR method to gain new insights into the dynamic behavior of these processes. Through establishing significant circumstantial evidence as well as the first direct observation of the powder pore transfer mechanism, coupled with the preliminary work identifying the potential risks associated with thermal induced porosity via post-HIP heat treatment, and most importantly mapping out the dynamic transitions and evolution of the depression morphology, both of these goals have been achieved.

9.2 Revised Hypotheses

In this section, the hypotheses put forth in Chapter 1 will be revised given the new information described in this work:

1. Inert gas trapped in the powder can be transferred to printed parts. This is observed to occur when powder is pulled into the melt pool away from the vapor depression. Contact with the vapor depression through remelting is an effective way to remove this porosity from previously deposited material.

2. The complexity of the keyhole transition has been significantly understated in the AM community. Laser spot welding identified two distinct transitions; the formation of the vapor cavity, and the subsequent collapse and transition into the fast drilling keyhole regime. Based on the results from the DXR for the 95 μm spot size, most of the process space for LPBF with similar beam sizes will be operating in the keyhole regime. The behavior of this keyhole is predictable to a first order by the ratio of the beam velocity and the power-density dependent drill rate. Based off of this relationship, a front wall angle of ~77° was determined a threshold in process space above which lies the high-risk depression morphologies that can produce keyhole porosity. However, any significant vapor depression morphology risks end of track defects, so non-steady state conditions need to be taken into account.

3. Inert gas containing pores in HIPed AM Ti-6Al-4V parts can regrow following post-HIP β-solution heat treatment. This includes trapped gas porosity from the powder, and both lack of fusion and keyhole defects formed in inert-gas environments. Additionally, irregular morphologies in the initial defect can carry over to the post-HIP condition, potentially increasing the risk of shortened fatigue life.

9.3 Future Work

The following proposed future work can further improve the understanding of defect formation mechanisms in metal powder bed AM processes:

1. Despite the important insights already gained during the early stages of development of the DXR experimental setup, the limitations imposed on the accuracy of the models in Chapters 6 and 7 because of the lack of an accurate beam profile highlights the need to fully characterize that setup before significant modeling work can begin.

2. While the in-situ DXR observations regarding keyhole formation in the LBPF process provide significant insights into the dynamic behavior that is otherwise difficult or impossible to capture, the true benefit of this technique will be through the validation and calibration of complex multi-physics models which can then be used to predict process outcomes without extensive experimentation.

3. Proof of concept for investigating solidification cracking using DXR has already been demonstrated. Coupling DXR with CT to get formation dynamics as well as full 3D information on crack growth and propagation could bring important insights to help expand the materials available to the AM community.

4. Scan strategy optimization to remove or reduce the severity of end of track pores.

5. Investigate the effect of variable pressure and different shielding gases on welding and AM processes using DXR.

6. This work focused on defect formation in Ti-6Al-4V, but there are many other material systems of interest to the additive manufacturing community, including but not limited to aluminum alloys, stainless steels, and nickel-based superalloys. While many of these

mechanisms will be active across other materials systems, it is important to fully explore those systems to the same extent.

7. Coupling of in-situ process monitoring techniques with the DXR technique would allow for connections between behavior that is readily observable in the machines with the sub-surface dynamic behavior only observable using x-ray radiography.

Appendix A: Image Analysis Code

Image J Preprocess Workflow:

run("Slice Keeper", "first=1 last=100 increment=1");
run("Z Project...", "projection=[Average Intensity]");

imageCalculator("Divide create 32-bit stack", "File_NAME","AVG__kept stack");
run("Reslice [/]...", "output=1.000 start=Left avoid");
run("Rotate 90 Degrees Right");
run("Flip Horizontally", "stack");
run("Z Project...", "projection=[Max Intensity]");
//run("Brightness/Contrast...");
run("Enhance Contrast", "saturated=0.35");

Matlab Code for Depth Profile Extraction

```matlab
%% Get Depth Profile
clear all
close all
%% Establish Properties
FrameRate = 50000;
PixelResolution = 1.98;
reference_line = 55;
% PixelResolution = 1;
% reference_line = 0;
threshold = 34000; % Threshold for meltpool detection

%% Read Data
% Load file info
[filename, path] = uigetfile('*.*');

% Read in image as matrix
img = imread([path '/' filename]);

%% Plot Image and Edge Detected Image
f = figure(1);
f.Color = 'w';
subplot(3,1,1)
imagesc(img)
axis off
title('Original Image')
colormap gray

% Apply edge detection
% img = imfilter(img,[0.5 1 0 -1 -0.5]','symmetric');
subplot(3,1,2)
imagesc(img)
axis off
title('Gradient Image')
colormap gray
hold on

%% Trace Profile

for n = 1:size(img,2) % loop through all times
    t_pixels(n) = n; %time in pixels
    depth_pixel_temp = find(img(:,n)>threshold,1,'last'); % check if meltpool exists
```

```matlab
    if isempty(depth_pixel_temp)
        depth_pixel(n) = reference_line; % if empty, say the depth is the reference line
    elseif depth_pixel_temp<reference_line
        depth_pixel(n) = reference_line; % if it thinks something above the reference line is a
meltpool, ignore it
    else
        depth_pixel(n) = depth_pixel_temp;
    end

end


%% Plot depth profile on top of image
plot(t_pixels,depth_pixel,'go','MarkerFaceColor','g','MarkerSize',1)
hold off


%% Add to original image
subplot(3,1,1)
hold on
plot(t_pixels,depth_pixel,'go','MarkerFaceColor','g','MarkerSize',1)
hold off


%% Convert to real units
time_s = (t_pixels-1)*(1/FrameRate);
depth_um = -PixelResolution*(depth_pixel-reference_line);


%% Plot Depth Profile with proper units
subplot(3,1,3)
plot(time_s,depth_um,'b','LineWidth',2)
axis tight
title('Depth vs Time')
xlabel('time (s)')
ylabel('depth (um)')
axis([min(time_s) max(time_s) min(depth_um) 0])


%% Make it pretty
set(findall(gcf,'-property','FontSize'),'FontSize',15)
set(findall(gcf,'-property','FontName'),'FontName','Helvetica')
f.Position = [814 74 300 631];


%% Save Data
% This uses the original file name
filename = [filename(1:end-4) '.xlsx'];


data = [time_s' depth_um'];
xlswrite(filename,data,'Sheet1','A1');
```

Appendix B: Estimating Beam Spot Size

In order to estimate the spot size of the laser as a function of distance from focus, two techniques were employed. The first method measured directly from the radiographs as the diameter of the keyhole opening. The second used the calculated theoretical spot size from the beam optics, and equation (3.3).
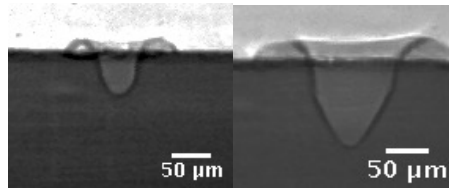
Figure B.9.1: Depression width for $2w_o$ = 95 µm (-2.5mm) and $2w_o$ = 140 µm (-4.5 mm).
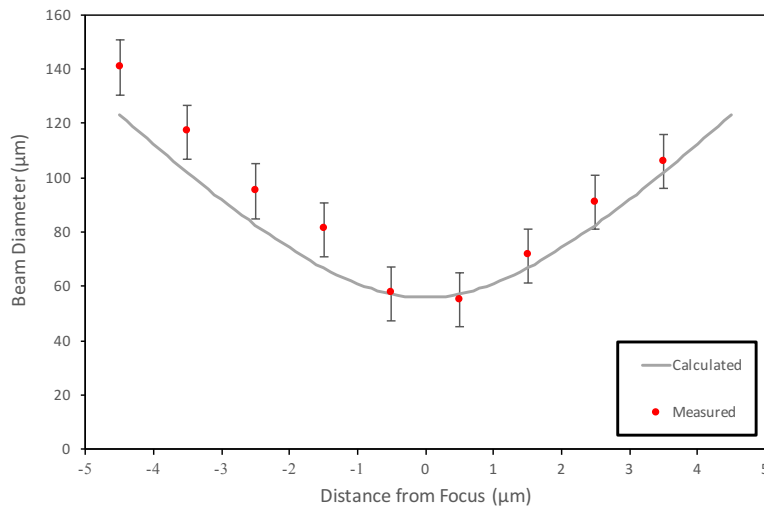
Figure B.9.2: Spot size calculated beam optics and divergence calculation and and vapor depression peak-to-peak width.

Appendix C: Data for Moving Beam Process Maps

Table C.1: List of Scanning Beam Experiments

Spot Size	Plate Thickness	Power (W)	Velocity (mm/s)	Depth (µm)	St. Dev (D)	FW Angle	St. Dev (θ)
140	400	130	0.4	24.68	2.38	22.31	3.73
140	400	156	0.4	28.27	3.04	23.59	3.96
140	400	169	0.4	31.90	3.56	28.67	2.75
140	400	182	0.4	53.10	7.78	36.63	2.37
140	400	195	0.4	53.36	11.34	39.20	4.00
140	400	208	0.4	82.99	9.57	42.49	1.53
140	400	234	0.4	110.56	19.81	49.85	4.23
140	400	260	0.4	149.59	7.84	56.79	0.75
140	400	156	0.7	17.31	2.53	24.25	4.33
140	400	208	0.7	35.42	2.48	33.44	2.95
140	400	234	0.7	45.69	2.41	41.99	1.44
140	400	260	0.7	60.04	6.17		
140	400	260	0.7	62.31	4.62	44.79	2.33
140	400	286	0.7	68.88	6.60	43.06	1.13
140	400	312	0.7	74.95	3.52	47.75	1.26
140	400	364	0.7	112.32	5.87	49.70	0.73
140	400	416	0.7	141.69	4.41	56.04	2.30
140	400	520	0.7	211.73	6.90	65.91	1.13
140	400	208	1	18.96	1.72	24.63	2.45
140	400	234	1	25.91	1.72	27.85	2.32
140	400	260	1	38.58	1.54	36.76	1.97
140	400	286	1	39.77	1.72	38.45	1.47
140	400	312	1	52.13	3.62	40.45	3.45
140	400	364	1	76.02	4.70	44.54	1.45
95	400	104	400	15.89	2.10	52.20	2.97
95	400	130	400	85.82	10.55	64.42	5.66
95	400	156	400	129.42	15.65	70.04	2.70
95	400	208	400	227.22	16.70	77.25	1.63
95	400	228.8	400	259.02	10.53	80.17	1.65
95	400	156	600	76.68	4.10	55.12	1.21
95	400	182	600	102.42	5.67	60.61	1.45
95	400	208	600	119.34	2.51	64.64	1.63

95	800	364	600	308.88	13.48	70.82	0.92
95	800	416	600	361.44	16.07	71.59	1.65
95	800	468	600	398.70	18.09	79.93	0.70
95	400	260	600	168.03	4.51	77.10	1.53
95	400	286	600	204.34	5.47	81.96	1.06
95	400	104	700	15.64	1.53		
95	400	156	700	63.63	3.82	56.58	3.37
95	400	208	700	118.40	4.13	65.29	3.06
95	400	260	700	161.82	3.81	73.37	1.99
95	400	364	700	257.94	11.14	75.65	2.21
95	800	416	700	287.76	10.80	78.45	1.66
95	800	468	700	330.87	11.33		
95	800	520	700	444.36	15.54		
95	800	312	700	220.41	12.92	82.01	0.91
95	400	156	1200	35.54	3.86	56.79	2.68
95	400	260	1200	96.48	2.47	67.14	1.67
95	400	364	1200	161.28	3.49	71.70	1.53
95	400	468	1200	216.06	5.75	73.13	1.42
95	800	520	1200	272.19	8.05	77.24	1.20
95	400	208	1200	78.21	3.56	80.22	0.86
95	400	312	1200	135.72	4.38	81.10	0.87
95	400	156	800	75.06	3.13	82.34	0.82
95	400	208	800	118.44	3.98	51.06	5.46
95	400	260	800	153.54	4.12	59.74	4.25
95	400	312	800	194.22	4.79	72.08	2.15
95	400	364	800	252.72	4.80	72.57	1.50
95	400	416	800	324.72	14.65	76.65	1.40
95	400	468	800	366.48	13.25	76.87	0.78
95	400	520	800	423.96	12.66	81.29	0.93
95	400	156	900	60.36	3.30	80.77	1.02
95	400	208	900	99.15	4.67	57.47	2.82
95	400	260	900	148.59	10.25	75.14	2.03
95	400	312	900	173.79	7.35	75.18	0.88
95	400	364	900	237.78	8.45	75.39	0.73
95	400	416	900	261.90	6.93	80.18	0.93
95	400	468	900	356.04	17.05	78.81	1.07
95	400	520	900	376.20	20.15	60.06	3.54
95	400	416	1000	226.80	4.07	69.50	1.37
95	400	520	1000	308.16	6.84	76.64	0.66

95	400	468	1000	293.49	9.05	78.06	1.19
95	400	208	1000	86.76	2.65	50.62	1.79
95	400	312	1000	181.89	6.78	58.46	0.72
95	400	364	1000	209.16	5.23	63.56	1.38
95	400	208	1100	83.82	4.20	67.94	1.73
95	400	312	1100	146.28	3.85	70.97	1.37
95	400	416	1100	232.44	2.49		
95	400	520	1100	285.30	2.86	77.43	0.80

Appendix D: Supplemental Video Captions

S4.1: DXR recording of powder pore transfer under stationary laser. P= 312W, spot size ~ 200μm, 50kHz.

S4.2: DXR recording of powder pore transfer under scanning laser. P = 260 W, V = 700 mm/s, spot size ~ 300μm, 50 kHz.

S6.1: DXR recording showing initial depression formation and secondary keyhole transition under stationary laser illumination. P = 156 W, spot size = 140 μm, 200 kHz.

S7.1: DXR recording showing fluctuation vapor depression under beam parameters near predicted keyhole transition. P = 260W, V = 400 mm/s, spot size = 140 μm, 50 kHz.

S7.2: DXR recording of keyhole pore formation under scanning laser. P = 230 W, V = 400 mm/s, spot size = 95 μm, 50 kHz.

S7.3: DXR recording at beam turnaround where heat buildup causes a shift in vapor depression morphologies similar to operating at higher power. P= 260 W, V = 700 mm/s, spot size = 95 μm, 50 kHz.

S7.4: DXR recording showing end of track defect left by deep, high angle depression. Rear keyhole wall collapses forward, trapping pore at bottom of depression. P = 416 W, 800 mm/s, spot size = 95μm, 50 kHz.

S7.5: DXR recording showing end of track defect left by shallow, low angle depression. Fluid flow is directed backward, resulting in depression freezing in place. P = 208 W, V = 1200 mm/s, spot size = 95 μm, 50 kHz.

Bibliography

[1]   W. E. Frazier, "Metal additive manufacturing: A review," *J. Mater. Eng. Perform.*, vol. 23, no. 6, pp. 1917–1928, 2014.

[2]   H. Gong, K. Rafi, H. Gu, T. Starr, and B. Stucker, "Analysis of defect generation in Ti-6Al-4V parts made using powder bed fusion additive manufacturing processes," *Addit. Manuf.*, vol. 1, pp. 87–98, 2014.

[3]   S. Tammas-Williams, H. Zhao, F. Léonard, F. Derguti, I. Todd, and P. B. Prangnell, "XCT analysis of the influence of melt strategies on defect population in Ti-6Al-4V components manufactured by Selective Electron Beam Melting," *Mater. Charact.*, vol. 102, pp. 47–61, 2015.

[4]   R. Cunningham, S. P. Narra, T. Ozturk, J. Beuth, and A. D. Rollett, "Evaluating the Effect of Processing Parameters on Porosity in Electron Beam Melted Ti-6Al-4V via Synchrotron X-ray Microtomography," *Jom*, vol. 68, no. 3, pp. 765–771, 2016.

[5]   S. Tammas-Williams, P. J. Withers, I. Todd, and P. B. Prangnell, "The Effectiveness of Hot Isostatic Pressing for Closing Porosity in Titanium Parts Manufactured by Selective Electron Beam Melting," *Metall. Mater. Trans. A Phys. Metall. Mater. Sci.*, vol. 47, no. 5, pp. 1939–1946, 2016.

[6]   M. Seifi, A. Salem, D. Satko, J. Shaffer, and J. J. Lewandowski, "Defect distribution and microstructure heterogeneity effects on fracture resistance and fatigue behavior of EBM Ti-6Al-4V," *Int. J. Fatigue*, vol. 94, pp. 263–287, Jan. 2017.

[7]   C. Kantzos, J. Pauza, R. Cunningham, S. Narra, J. Beuth, and A. D. Rollett, "A Survey of Process Parameter Modifications: Effects on Microstructure, Porosity, and Mechanical Performance," *J. Mater. Eng. Perform.*, vol. (Submitted.

[8]   J. Beuth, J. Fox, J. Gockel, C. Montgomery, R. Yang, H. Qiao, E. Soylemes, P. Reeseewatt, A. Anvari, S. Narra, and N. Klingbeil, "Process mapping for qualification across multiple direct metal additive manufacturing processes," in *Proceedings of Solid Freeform Fabrication Symposium*, 2013, pp. 655–665.

[9]   S. Tammas-Williams, P. J. Withers, I. Todd, and P. B. Prangnell, "Porosity regrowth during heat treatment of hot isostatically pressed additively manufactured titanium components," *Scr. Mater.*, vol. 122, pp. 72–76, 2016.

[10]   R. J. Hebert, "Viewpoint: metallurgical aspects of powder bed metal additive manufacturing," *J. Mater. Sci.*, vol. 51, no. 3, pp. 1165–1175, 2016.

[11]   D. Eylon, S. W. Schwenker, and F. H. Froes, "Thermally induced porosity in Ti-6Al-4V prealloyed powder compacts," *Metall. Trans. A*, vol. 16, no. 8, pp. 1526–1531, 1985.

[12]   B. D. C. Dunand, "Processing of Titanium Foams," no. 6, pp. 369–376, 2004.

[13]   Z. Francis, "The Effects of Laser and Electron Beam Spot Size in Additive Manufacturing Processes," Carnegie Mellon University, 2017.

[14]   D. Wright, "Beamwidths of a diffracted laser using four proposed methods," *Opt. Quantum Electron.*, vol. 24, no. 9, 1992.

[15]   D. Rosenthal, "Mathematical theory of heat distribution during welding and cutting," *Weld. J.*, vol. 20, no. 5, p. 220s--234s, 1941.

[16]   S. S. Al-Bermani, M. L. Blackmore, W. Zhang, and I. Todd, "The origin of microstructural diversity, texture, and mechanical properties in electron beam melted Ti-6Al-4V," *Metall. Mater. Trans. A Phys. Metall. Mater. Sci.*, vol. 41, no. 13, pp. 3422–3434, 2010.

[17]   O. D. Neikov, "Atomization and granulation," in *Handbook of Non-Ferrous Metal Powders*, 2009, pp. 102–142.

[18]   B. H. Rabin, G. R. Smolik, and G. E. Korth, "Characterization of entrapped gases in rapidly solidified powders," *Mater. Sci. Eng. A*, vol. 124, no. 1, pp. 1–7, 1990.

[19]   G. K. L. Ng, A. E. W. Jarfors, G. Bi, and H. Y. Zheng, "Porosity formation and gas bubble retention in laser metal deposition," *Appl. Phys. A Mater. Sci. Process.*, vol. 97, no. 3, pp. 641–649, 2009.

[20]   P. A. Kobryn, E. H. Moore, and S. L. Semiatin, "Effect of laser power and traverse speed on microstructure, porosity, and build height in laser-deposited Ti-6Al-4V," *Scr. Mater.*, vol. 43, no. 4, pp. 299–305, 2000.

[21]   T. Holt, E. Lindeberg, and S. Ratkje, "The Effect of Gravity and Temperature Gradients on Methane Distribution in Oil Reservoirs," *unsolicited Pap. SPE 11761*, vol. 23, 1983.

[22]   G. Tsotridis, H. Rother, and E. D. Hondros, "Marangoni flow and the shapes of laser-melted pools," *Naturwissenschaften*, vol. 76, no. 5, pp. 216–218, 1989.

[23]   R. B. Bird, W. E. Stewart, and E. N. Lightfoot, *Transport phenomena*. John Wiley & Sons, 2007.

[24]   T. Mohandas, D. Banerjee, and V. V. Kutumba Rao, "Fusion zone microstructure and porosity in electron beam welds of an α+β titanium alloy," *Metall. Mater. Trans. A*, vol. 30, no. 3, pp. 789–798, 1999.

[25]   N. Gouret, G. Dour, B. Miguet, E. Ollivier, and R. Fortunier, "Assessment of the Origin of Porosity in Electron-Beam-Welded TA6V Plates," *Metall. Mater. Trans. A*, vol. 35, no. March, pp. 879–889, 2004.

[26]   J. L. Huang, N. Warnken, J. C. Gebelin, M. Strangwood, and R. C. Reed, "On the

mechanism of porosity formation during welding of titanium alloys," *Acta Mater.*, vol. 60, no. 6–7, pp. 3215–3225, 2012.

[27] H. Gong, K. Rafi, H. Gu, G. D. Janaki Ram, T. Starr, and B. Stucker, "Influence of defects on mechanical properties of Ti-6Al-4V components produced by selective laser melting and electron beam melting," *Mater. Des.*, vol. 86, pp. 545–554, 2015.

[28] W. E. King, H. D. Barth, V. M. Castillo, G. F. Gallegos, J. W. Gibbs, D. E. Hahn, C. Kamath, and A. M. Rubenchik, "Observation of keyhole-mode laser melting in laser powder-bed fusion additive manufacturing," *J. Mater. Process. Technol.*, vol. 214, no. 12, pp. 2915–2925, 2014.

[29] S. Leuders, M. Thöne, A. Riemer, T. Niendorf, T. Tröster, H. A. Richard, and H. J. Maier, "On the mechanical behaviour of titanium alloy TiAl6V4 manufactured by selective laser melting: Fatigue resistance and crack growth performance," *Int. J. Fatigue*, vol. 48, pp. 300–307, 2013.

[30] E. Wycisk, A. Solbach, S. Siddique, D. Herzog, F. Walther, and C. Emmelmann, "Effects of defects in laser additive manufactured Ti-6Al-4V on fatigue properties," *Phys. Procedia*, vol. 56, no. C, pp. 371–378, 2014.

[31] P. Edwards and M. Ramulu, "Fatigue performance evaluation of selective laser melted Ti-6Al-4V," *Mater. Sci. Eng. A*, vol. 598, pp. 327–337, 2014.

[32] S. Leuders, M. Vollmer, F. Brenne, T. Tröster, and T. Niendorf, "Fatigue Strength Prediction for Titanium Alloy TiAl6V4 Manufactured by Selective Laser Melting," *Metall. Mater. Trans. A*, vol. 46, no. 9, pp. 3816–3823, 2015.

[33] G. Kasperovich and J. Hausmann, "Improvement of fatigue resistance and ductility of TiAl6V4 processed by selective laser melting," *J. Mater. Process. Technol.*, vol. 220, pp. 202–214, 2015.

[34] M. Tang and P. C. Pistorius, "Oxides, porosity and fatigue performance of AlSi10Mg parts produced by selective laser melting," *Int. J. Fatigue*, vol. 94, pp. 192–201, 2017.

[35] X. Zhou, D. Wang, X. Liu, D. D. Zhang, S. Qu, J. Ma, G. London, Z. Shen, and W. Liu, "3D-imaging of selective laser melting defects in a Co-Cr-Mo alloy by synchrotron radiation micro-CT," *Acta Mater.*, vol. 98, pp. 1–16, 2015.

[36] M. Tang, P. C. Pistorius, and J. L. Beuth, "Prediction of lack-of-fusion porosity for powder bed fusion," *Addit. Manuf.*, vol. 14, pp. 39–48, 2017.

[37] J. C. Ion, *Laser Processing of Engineering Materials: Principles, Procedure and Industrial Application*. Elsevier Science, 2005.

[38] R. Rai, J. W. Elmer, T. Palmer, and T. DebRoy, "Heat transfer and fluid flow during keyhole mode laser welding of tantalum, Ti–6Al–4V, 304L stainless steel and vanadium," *J. Phys. D. Appl. Phys.*, vol. 40, no. 18, pp. 5753–5766, 2007.

[39]   T. Debroy and S. A. David, "Physical processes in fusion welding," *Rev. Mod. Phys.*, vol. 67, no. 1, pp. 85–112, 1995.

[40]   S. Basu and T. DebRoy, "Liquid metal expulsion during laser irradiation," *J. Appl. Phys.*, vol. 72, no. 8, pp. 3317–3322, 1992.

[41]   X. He, J. T. Norris, P. W. Fuerschbach, and T. Debroy, "Liquid metal expulsion during laser spot welding of 304 stainless steel," *J. Phys. D. Appl. Phys.*, vol. 39, no. 3, pp. 525–534, 2006.

[42]   K. Hirano, R. Fabbro, and M. Muller, "Experimental determination of temperature threshold for melt surface deformation during laser interaction on iron at atmospheric pressure," *J. Phys. D. Appl. Phys.*, vol. 44, no. 43, 2011.

[43]   V. V Semak, W. D. Bragg, B. Damkroger, V. Semak, and A. Matsunawa, "The role of recoil pressure in energy balance during laser materials processing," 1997.

[44]   J. Trapp, A. M. Rubenchik, G. Guss, and M. J. Matthews, "In situ absorptivity measurements of metallic powders during laser powder-bed fusion additive manufacturing," *Appl. Mater. Today*, vol. 9, pp. 341–349, 2017.

[45]   D. Bäuerle, *Laser Processing and Chemistry*. 2011.

[46]   D. B. Hann, J. Iammi, and J. Folkes, "A simple methodology for predicting laser-weld properties from material and laser parameters," *J. Phys. D. Appl. Phys.*, vol. 44, no. 44, 2011.

[47]   E. Assuncao, S. Williams, and D. Yapp, "Interaction time and beam diameter effects on the conduction mode limit," *Opt. Lasers Eng.*, vol. 50, no. 6, pp. 823–828, 2012.

[48]   J. Svenungsson, I. Choquet, and A. F. H. Kaplan, "Laser Welding Process - A Review of Keyhole Welding Modelling," *Phys. Procedia*, vol. 78, no. August, pp. 182–191, 2015.

[49]   W. Tan and Y. C. Shin, "Analysis of multi-phase interaction and its effects on keyhole dynamics with a multi-physics numerical model," *J. Phys. D. Appl. Phys.*, vol. 47, no. 34, p. 345501, 2014.

[50]   A. Matsunawa, J.-D. Kim, N. Seto, M. Mizutani, and S. Katayama, "Dynamics of keyhole and molten pool in laser welding," *J. Laser Appl.*, vol. 10, no. 6, pp. 247–254, 1998.

[51]   N. Seto, S. Katayama, and A. Matsunawa, "High-speed simultaneous observation of plasma and keyhole behavior during high power CO2 laser welding: Effect of shielding gas on porosity formation," *J. Laser Appl.*, vol. 12, no. 6, pp. 245–250, 2000.

[52]   R. Fabbro and K. Chouf, "Keyhole modeling during laser welding," *J. Appl. Phys.*, vol. 87, no. 9, pp. 4075–4083, 2000.

[53]   J. Y. Lee, S. H. Ko, D. F. Farson, and C. D. Yoo, "Mechanism of keyhole formation and

stability in stationary laser welding," *J. Phys. D. Appl. Phys.*, vol. 35, no. 13, p. 1570, 2002.

[54]   J. D. Madison and L. K. Aagesen, "Quantitative characterization of porosity in laser welds of stainless steel," *Scr. Mater.*, vol. 67, no. 9, pp. 783–786, 2012.

[55]   J. W. Elmer, J. Vaja, and H. D. Carlton, "The effect of reduced pressure on laser keyhole weld porosity and weld geometry in commercially pure titanium and nickel," *Weld. J.*, vol. 95, no. 11, pp. 419–430, 2016.

[56]   S. Katayama and M. Mizutani, "Laser Weldability of Aluminum Alloys," *Trans. JWRI*, vol. 31, no. 2, pp. 147–155, 2002.

[57]   J. W. Elmer, J. Vaja, H. D. Carlton, and R. pong, "The Effect of Ar and N 2 Shielding Gas on Laser Weld Porosity in Steel , Stainless Steels , and Nickel," *Weld. J.*, vol. 94, no. 10, pp. 313–325, 2015.

[58]   S. A. Khairallah, A. T. Anderson, A. Rubenchik, and W. E. King, "Laser powder-bed fusion additive manufacturing: Physics of complex melt flow and formation mechanisms of pores, spatter, and denudation zones," *Acta Mater.*, vol. 108, pp. 36–45, 2016.

[59]   M. A. Groeber, E. Schwalbach, S. Donegan, K. Chaput, T. Butler, and J. Miller, "Application of characterization, modelling, and analytics towards understanding process-structure linkages in metallic 3D printing," *IOP Conf. Ser. Mater. Sci. Eng.*, vol. 219, no. 1, p. 12002, 2017.

[60]   H. Atkinson and S. Davies, "Fundamental aspects of hot isostatic pressing: an overview," *Metall. Mater. Trans. A*, vol. 31A, no. December, pp. 2981–3000, 2000.

[61]   R. L. Dreshfield and R. V. Miner, "Effects of thermally induced porosity on an as-HIP powder metallurgy superalloy," *Annu. Meet. Am. Inst. Mining, Metall. Pet. Eng.*, 1980.

[62]   G. Wegmann, R. Gerling, and F. P. Schimansky, "Temperature induced porosity in hot isostatically pressed gamma titanium aluminide alloy powders," *Acta Mater.*, vol. 51, no. 3, pp. 741–752, 2003.

[63]   N. G. D. Murray and D. C. Dunand, "Effect of thermal history on the superplastic expansion of argon-filled pores in titanium: Part I kinetics and microstructure," *Acta Mater.*, vol. 52, no. 8, pp. 2279–2291, 2004.

[64]   S. Oppenheimer and D. C. Dunand, "Solid-state foaming of Ti − 6Al − 4V by creep or superplastic expansion of argon-filled pores," *Acta Mater.*, vol. 58, no. 13, pp. 4387–4397, 2010.

[65]   F. Léonard, S. Tammas-williams, P. B. Prangnell, I. Todd, P. J. Withers, H. Moseley, and X. I. Facility, "Assessment by X-ray CT of the effects of geometry and build direction on defects in titanium ALM parts," *Conf. Ind. Comput. Tomogr.*, pp. 85–93, 2012.

[66]   G. Ziółkowski, E. Chlebus, P. Szymczyk, and J. Kurzac, "Application of X-ray CT method for discontinuity and porosity detection in 316L stainless steel parts produced with SLM technology," *Arch. Civ. Mech. Eng.*, vol. 14, no. 4, pp. 608–614, 2014.

[67]   M. N. Ahsan, R. Bradley, and A. J. Pinkerton, "Microcomputed tomography analysis of intralayer porosity generation in laser direct metal deposition and its causes," *J. Laser Appl.*, vol. 23, no. 2, p. 22009, 2011.

[68]   L. De Chiffre, S. Carmignato, J. P. Kruth, R. Schmitt, and A. Weckenmann, "Industrial applications of computed tomography," *CIRP Ann. - Manuf. Technol.*, vol. 63, no. 2, pp. 655–677, 2014.

[69]   F. H. Kim, S. P. Moylan, E. J. Garboczi, and J. A. Slotwinski, "Investigation of pore structure in cobalt chrome additively manufactured parts using X-ray computed tomography and three-dimensional image analysis," *Addit. Manuf.*, vol. 17, pp. 23–38, 2017.

[70]   J. A. Slotwinski, E. J. Garboczi, and K. M. Hebenstreit, "Porosity Measurements and Analysis for Metal Additive Manufacturing Process Control," *J. Res. Natl. Inst. Stand. Technol.*, vol. 119, p. 494, 2014.

[71]   S. R. Stock, "Recent advances in X-ray microtomography applied to materials," *Int. Mater. Rev.*, vol. 53, no. 3, pp. 129–181, 2008.

[72]   J. Kastner, B. Harrer, G. Requena, and O. Brunke, "A comparative study of high resolution cone beam X-ray tomography and synchrotron tomography applied to Fe- and Al-alloys," *NDT E Int.*, vol. 43, no. 7, pp. 599–605, 2010.

[73]   D. Gürsoy, F. De Carlo, X. Xiao, and C. Jacobsen, "TomoPy: A framework for the analysis of synchrotron tomographic data," *J. Synchrotron Radiat.*, vol. 21, no. 5, pp. 1188–1193, 2014.

[74]   B. A. Dowd, G. H. Campbell, R. B. Marr, V. V Nagarkar, S. V Tipnis, L. Axe, and D. P. Siddons, "Developments in synchrotron x-ray computed microtomography at the National Synchrotron Light Source," *Proc. SPIE*, vol. 3772, no. July, pp. 224–236, 1999.

[75]   B. Münch, P. Trtik, F. Marone, and M. Stampanoni, "Stripe and ring artifact removal with combined wavelet-Fourier filtering," *EMPA Act.*, vol. 17, no. 2009–2010 EMPA ACTIVITIES, pp. 34–35, 2009.

[76]   T. S. Niranjan D. Parab, Cang Zhao, Ross Cunningham, Kamel Fezzaa, Wes Everhart, Anthony D. Rollett, Lianyi Chen, "Ultrafast X-ray Imaging of Laser Metal Additive Manufacturing Processes," *J. Synchrotron Radiat.*

[77]   W. Meng, Z. Li, F. Lu, Y. Wu, J. Chen, and S. Katayama, "Porosity formation mechanism and its prevention in laser lap welding for T-joints," *J. Mater. Process. Technol.*, vol. 214, no. 8, pp. 1658–1664, 2014.

[78] S. Mobilio, F. Boscherini, and C. Meneghini, *Synchrotron Radiation: Basics, Methods and Applications*. 2015.

[79] S. W. Wilkins, T. E. Gureyev, D. Gao, A. Pogany, and A. W. Stevenson, "Phase-contrast imaging using polychromatic hard X-rays," *Nature*, vol. 384, no. 6607, pp. 335–338, 1996.

[80] R. P. Murrie, A. W. Stevenson, K. S. Morgan, A. Fouras, D. M. Paganin, and K. K. W. Siu, "Feasibility study of propagation-based phase-contrast X-ray lung imaging on the Imaging and Medical beamline at the Australian Synchrotron," *J. Synchrotron Radiat.*, vol. 21, no. 2, pp. 430–445, Mar. 2014.

[81] R. Cunningham, A. Nicolas, J. Madsen, E. Fodran, E. Anagnostou, M. D. Sangid, and A. D. Rollett, "Analyzing the effects of powder and post-processing on porosity and properties of electron beam melted Ti-6Al-4V," *Mater. Res. Lett.*, vol. 5, no. 7, pp. 516–525, 2017.

[82] R. Cunningham, A. Nicolas, J. Madsen, E. Fodran, E. Anagnostou, M. D. Sangid, and A. D. Rollett, "Analyzing the effects of powder and post-processing on porosity and properties of electron beam melted Ti-6Al-4V," *Mater. Res. Lett.*, vol. 5, no. 7, pp. 516–525, 2017.

[83] S. P. Narra, R. Cunningham, J. Beuth, and A. D. Rollett, "Location specific solidification microstructure control in electron beam melting of Ti-6Al-4V," *Addit. Manuf.*, vol. 19, pp. 160–166, 2018.

[84] Z. C. Cordero, R. B. Dinwiddie, D. Immel, and R. R. Dehoff, "Nucleation and growth of chimney pores during electron-beam additive manufacturing," *J. Mater. Sci.*, vol. 52, no. 6, pp. 3429–3435, 2017.

[85] A. Bauereiß, T. Scharowsky, and C. Körner, "Defect generation and propagation mechanism during additive manufacturing by selective beam melting," *J. Mater. Process. Technol.*, vol. 214, no. 11, pp. 2497–2504, 2014.

[86] H. P. Tang, M. Qian, N. Liu, X. Z. Zhang, G. Y. Yang, and J. Wang, "Effect of Powder Reuse Times on Additive Manufacturing of Ti-6Al-4V by Selective Electron Beam Melting," *Jom*, vol. 67, no. 3, pp. 555–563, 2015.

[87] R. Cunningham, S. P. S. P. Narra, C. Montgomery, J. Beuth, and A. D. D. Rollett, "Synchrotron-Based X-ray Microtomography Characterization of the Effect of Processing Variables on Porosity Formation in Laser Power-Bed Additive Manufacturing of Ti-6Al-4V," *Jom*, vol. 69, no. 3, pp. 479–484, 2017.

[88] M. Tang, P. C. Pistorius, and J. Beuth, "Geometric Model To Predict Porosity of Part Produced," *Mater. Sci. Technol.*, pp. 129–136, 2015.

[89] J. A. Kanko, A. P. Sibley, and J. M. Fraser, "In situ morphology-based defect detection of selective laser melting through inline coherent imaging," *J. Mater. Process. Technol.*, vol.

231, pp. 488–500, 2016.

[90] C. Zhao, K. Fezzaa, R. W. Cunningham, H. Wen, F. De Carlo, L. Chen, A. D. Rollett, and T. Sun, "Real-time monitoring of laser powder bed fusion process using high-speed X-ray imaging and diffraction," *Sci. Rep.*, vol. 7, no. 1, pp. 1–11, 2017.

[91] E. A. Brandes and G. B. Brook, *Smithells Metals Reference Book, 7th ed.* Elsevier, 1992.

[92] K. C. Mills, *Recommended values of thermophysical properties for selected commercial alloys*. Woodhead Publishing, 2002.

[93] M. Von Allmen, "Laser drilling velocity in metals," *J. Appl. Phys.*, vol. 47, no. 12, pp. 5460–5463, 1976.

[94] K. T. Voisey, S. S. Kudesia, W. S. O. Rodden, D. P. Hand, J. D. C. Jones, and T. W. Clyne, "Melt ejection during laser drilling of metals," *Mater. Sci. Eng. A*, vol. 356, no. 1–2, pp. 414–424, 2003.

[95] J. Cho, D. F. Farson, J. O. Milewski, and K. J. Hollis, "Weld pool flows during initial stages of keyhole formation in laser welding," 2009.

[96] M. Medale, C. Xhaard, and R. Fabbro, "A thermo-hydraulic numerical model to study spot laser welding," vol. 335, pp. 280–286, 2007.

[97] H. Ki, P. S. Mohanty, and J. Mazumder, "Multiple reflection and its influence on keyhole evolution," *J. Laser Appl.*, vol. 14, no. 1, pp. 39–45, 2002.

[98] M. von Allmen and A. Blatter, *Laser-Beam Interactions with Materials*, vol. 2. 1995.

[99] D. Bäuerle, *Chemical processing with lasers*. 1986.

[100] C. D. Boley, S. A. Khairallah, and A. M. Rubenchik, "Calculation of laser absorption by metal powders in additive manufacturing," *Appl. Opt.*, vol. 54, no. 9, p. 2477, 2015.

[101] Y. Pan and I. M. Richardson, "Keyhole behaviour during laser welding of zinc-coated steel," *J. Phys. D. Appl. Phys.*, vol. 44, no. 4, 2011.

[102] I. Eriksson, J. Powell, and A. F. H. Kaplan, "Melt behavior on the keyhole front during high speed laser welding," *Opt. Lasers Eng.*, vol. 51, no. 6, pp. 735–740, 2013.

[103] A. Matsunawa and V. Semak, "The simulation of front keyhole wall dynamics during laser welding," *J.Phys.D: Appl.Phys*, vol. 30, no. 5, pp. 798–809, 1997.

[104] J. Peng, L. Li, S. Lin, F. Zhang, Q. Pan, and S. Katayama, "High-Speed X-Ray Transmission and Numerical Study of Melt Flows inside the Molten Pool during Laser Welding of Aluminum Alloy," *Math. Probl. Eng.*, vol. 2016, 2016.

[105] L. Song, V. Bagavath-Singh, B. Dutta, and J. Mazumder, "Control of melt pool temperature and deposition height during direct metal deposition process," *Int. J. Adv.*

Manuf. Technol., vol. 58, no. 1–4, pp. 247–256, 2012.

[106] S. M. Gaytan, L. E. Murr, F. Medina, E. Martinez, M. I. Lopez, and R. B. Wicker, "Advanced metal powder based manufacturing of complex components by electron beam melting," *Mater. Technol. Adv. Perform. Mater.*, vol. 24, no. 3, pp. 180–190, 2009.

[107] D. Eylon and B. Strope, "Fatigue crack initiation in Ti-6wt % Al-4 wt % V castings," *J. Mater. Sci.*, vol. 14, no. 2, pp. 345–353, 1979.

[108] R. V. Miner and R. L. Dreshfield, "Effects of fine porosity on the fatigue behavior of a powder metallurgy superalloy," *Metall. Trans. A*, vol. 12, no. 2, pp. 261–267, 1981.

[109] A. Majorell, S. Srivatsa, and R. C. Picu, "Mechanical behavior of Ti-6Al-4V at high and moderate temperatures-Part I: Experimental results," *Mater. Sci. Eng. A*, vol. 326, no. 2, pp. 297–305, 2002.